CENTRO INTERNACIONAL DE ESTUDOS
DE DOUTORAMENTO E AVANZADOS
DA USC (CIEDUS)

TESE DE DOUTORAMENTO

STUDY OF LASER-PLASMA INTERACTION WITH PARTICLE-IN-CELL SIMULATIONS: ATTOSECOND PULSE GENERATION AND PROTON ACCELERATION

Manuel Blanco Fraga

ESCOLA DE DOUTORAMENTO INTERNACIONAL EN CIENCIAS E TENOLOXÍAS DA USC

PROGRAMA DE DOUTORAMENTO EN LÁSER, FOTÓNICA E VISIÓN

SANTIAGO DE COMPOSTELA

2018

USC
UNIVERSIDADE
DE SANTIAGO
DE COMPOSTELA

DECLARACIÓN DO AUTOR DA TESE

Study of laser-plasma interaction with particle-in-cell simulations: attosecond pulse generation and proton acceleration

D. Manuel Blanco Fraga

Presento miña tese, seguindo o procedemento adecuado ao Regulamento, e declaro que:

1) A tese abarca os resultados da elaboración do meu traballo.
2) No seu caso, na tese se fai referencia as colaboracións que tivo este traballo.
3) A tese é a versión definitiva presentada para a súa defensa e coincide ca versión enviada en formato electrónico.
4) Confirmo que a tese non incorre en ningún tipo de plaxio de outros autores nin de traballos presentados por min para a obtención de outros títulos.

En Santiago de Compostela, 12 de marzo de 2018

Asdo.
Manuel Blanco Fraga

USC
UNIVERSIDADE
DE SANTIAGO
DE COMPOSTELA

AUTORIZACIÓN DO DIRECTOR / TITOR DA TESE

Study of laser-plasma interaction with particle-in-cell simulations: attosecond pulse generation and proton acceleration

Dna. María Teresa Flores Arias

INFORMA:

Que a presente tese, correspóndese co traballo realizado por D. ***Manuel Blanco Fraga****, baixo a miña dirección, e autorizo a súa presentación, considerando que reúne os requisitos esixidos no Regulamento de Estudos de Doutoramento da USC, e que como directora desta non incorre nas causas de abstención establecidas na Lei 40/2015.*

En Santiago de Compostela, 12 de marzo de 2018

Asdo.
María Teresa Flores Arias

USC
UNIVERSIDADE
DE SANTIAGO
DE COMPOSTELA

Me gustaría comenzar esta tesis con la escritura de unas líneas de agradecimiento, que probablemente sean las que más veces he releído de este documento, dado que no es fácil resumir una etapa vital en unos párrafos de texto, y las palabras en la mayor parte de los casos se quedan cortas a la hora de expresar mi gratitud.

Este trabajo no habría sido posible de no ser por toda la gente que me ha acompañado a lo largo de este periplo de casi cuatro años. Sé que es imposible mencionar a todos aquellos que han contribuido directa o indirectamente en la culminación de este trabajo, pero en los siguientes párrafos me gustaría agradecer a una parte de todas esas personas.

En primer lugar, me gustaría agradecerle a Alicia todo su apoyo incondicional, sin el cual me habría desmoronado en los momentos más difíciles, su alegría ante mis logros, sin la cual no habría sabido valorarlos como es debido, y el haber estado a mi vera todos estos años. Le agradezco a mi madre María y a mi padrastro Fernando el ser tan comprensivos con mi dedicación a tiempo completo a este proyecto, que muchas veces me ha impedido disfrutar de todo el tiempo que quisiera con ellos. Me gustaría agradecer a toda mi familia y a todos mis amigos de la infancia, instituto y universidad, por todas las experiencias que me han brindado antes y durante estos años. Sin ello hoy no sería quien soy y puede que nunca hubiera llegado aquí.

Quiero hacer también un agradecimiento especial a mi grupo de amigos de la universidad y a ese gran chat grupal que compartimos, que me ha amenizado cada día de estos últimos años, que me ha permitido debatir y aprender sobre muchos temas y que me ha sabido arrancar una sonrisa hasta en los momentos menos agradables.

Agradezco a la Universidad de Santiago de Compostela y al profesorado del Grado en Física, por la gran educación académica que me han brindado. Le doy las gracias a mi directora de tesis, Maite Flores, por todo el trabajo y esfuerzos que soy consciente que ha dedicado a sacar adelante este proyecto y por haber sido, sin un ápice de duda, la mejor jefa que uno pueda desear. También le doy las gracias a los profesores, técnicos e investigadores del Área de Óptica de la Facultad de Física y a todos mis compañeros de despacho. En especial me gustaría dar las gracias a Ángel por enseñarme que existe cine fuera de Hollywood, a María por confabular conmigo para dominar el mundo, a Ferran por todas sus anécdotas graciosas sobre siensia y globalmente a todos ellos por haber sido capaces de soportarme, de escuchar todos esos datos y curiosidades irrelevantes de las que hablo constantemente y de aguantar mis

discursos políticos. Quiero agradecer también a todos mis amigos codoctorandos de la facultad de física o que eventualmente han estado por aquí. Muchas gracias Javi, Manu, Juan, Jose, Dani, Víctor, Damián, Heli, Lucía, Ramiro y Amina, por esos cientos de cafés que hemos tomado juntos a media mañana en los que arreglamos el mundo en cuestión de 20 minutos y por esas comidas en la facultad de matemáticas que le dan alegría a la rutina diaria.

Quiero también extender mi agradecimiento a los alumnos y alumnas del grado en física a los que he tenido la oportunidad de dar clase. Gracias por escucharme, por proveerme con alguna que otra anécdota graciosa y sobre todo por tener un espíritu crítico y hacerme dudar de toda afirmación que diga en clase, realmente habéis sido vosotros los que me habéis enseñado a mí a enseñar y a dudar de hasta los conceptos mejor establecidos.

I would also like to thank all the incredible people that I met in Lisbon during my stay there, that made me feel like at home. I thank Luis Silva and his group for giving me the opportunity to use their simulation code OSIRIS and hosting me for several months. I would like to thank Marija Vranic for teaching me so many things and always pushing me to achieve the best possible results in all our joint projects, I am sure that without her help I would not be able to be where I am now.

Thanks also to Arkady Gonoskov for giving me the opportunity to collaborate with him in exciting projects and all the PICADOR development team for allowing me to use their code.

Quiero también expresar mi gratitud al grupo de investigación en Aplicaciones del Láser y la Fotónica de la Universidad de Salamanca por haberme acogido como uno más en mi estancia allí. En particular quiero agradecer a Luis Plaja y Carlos Hernández el haberme brindado la oportunidad de colaborar con ellos.

Por último, mi más sincero agradecimiento a todos aquellos no mencionados aquí que han contribuido de alguna forma a este proyecto.

“El éxito no es definitivo. El fracaso no es definitivo. El valor para seguir adelante es lo que cuenta”

Este trabajo ha sido financiado parcialmente por diversas fuentes. Se agradece a la Xunta de Galicia y al Fondo Europeo de Desarrollo Regional (FEDER) por el programa de becas predoctorales en la convocatoria ED481A del año 2014 y por los proyectos EM2012/019, Agrup2015/11 (PC034) y ED431B 2017/64. Se agradece al Ministerio de Economía y Competitividad (MINECO) del gobierno de España por los proyectos MAT2015-71119-R y FIS2015-71933-REDT. Se agradece también Ministerio de Educación, Cultura y Deportes (MECD) del gobierno de España por su programa de becas predoctorales de Formación del Profesorado Universitario (FPU) en la convocatoria FPU14 del año 2014. También se agradece al consorcio OSIRIS, formado por la University of California, Los Angeles (UCLA) y el Instituto Superior Técnico (IST) por el uso de OSIRIS y por proporcionar acceso a la estructura de OSIRIS. Por último, se extiende el agradecimiento al Centro de Supercomputación de Galicia (CESGA) y al Barcelona Supercomputing Center (BSC) por permitir el uso de sus recursos.

USC
UNIVERSIDADE
DE SANTIAGO
DE COMPOSTELA

INDEX

USC
UNIVERSIDADE
DE SANTIAGO
DE COMPOSTELA

RESUMEN EXTENSO

Los avances en tecnología láser de las últimas décadas han permitido la exploración de nuevos regímenes de la física, el descubrimiento de nuevos fenómenos y la implementación de diversas aplicaciones novedosas. Todo esto ha convertido a los láseres en una herramienta esencial en la sociedad actual, con un impacto socioeconómico que se extiende en diversas áreas, tales como, por ejemplo, el procesado industrial de materiales, el tratamiento de semiconductores para la industria electrónica, las comunicaciones de alta velocidad gracias a la fibra óptica, o el formar una parte esencial directa o indirectamente en una gran variedad de campos científicos. Los láseres con longitudes temporales en el orden de los femtosegundos y con una elevada potencia pico se introdujeron en la década de 1980, y las potencias alcanzables no han parado de crecer desde entonces, abriendo en un primer lugar el campo de la interacción láser-plasma ultrarrelativista y estando hoy en día a las puertas de estudiar experimentalmente fenómenos asociados a la electrodinámica cuántica.

Cuando enfocamos estas fuentes láser pulsadas en un área micrométrica, se pueden alcanzar intensidades pico suficientes para ionizar un material sólido en una escala temporal por debajo de los femtosegundos, dadas las grandes amplitudes que alcanzan localmente los campos eléctricos. Esta ionización causada por la parte inicial del pulso láser genera un plasma en la superficie del material, con el que interaccionan estos campos. La interacción láser-plasma entre los láseres de alta potencia y los plasmas formados por electrones e iones, con densidades sólidas, tiene como producto dos fenómenos principales. Por una parte esta interacción causa el movimiento relativista de los electrones en la superficie del plasma, lo cual nos proporciona las herramientas para la generación de radiación pulsada ultracorta de alta frecuencia, con energías próximas al régimen de los rayos X y con un espectro energético en forma de armónicos de orden alto de la frecuencia central del pulso láser. Este espectro se emite periódicamente y aparece concentrado en el tiempo en

la forma de un tren de pulsos con longitudes temporales en la escala de las decenas o centenas de attosegundos. Por otra parte, otro producto de esta interacción es la aceleración de protones e iones localizados en la superficie posterior del blanco con el que interacciona el láser, que se ocasiona por el efecto de los electrones que son empujados por el pulso láser, atraviesan el blanco y salen por su cara posterior, generando en distancias micrométricas gradientes de campo eléctrico muy intensos, que son capaces de acelerar partículas con carga positiva en la superficie del material. El estudio de estos aceleradores es interesante por su reducido coste, por las propiedades singulares de los haces de partículas generados y por su compactibilidad, todo ello en comparación con los aceleradores de partículas convencionales. Las cualidades particulares de estos aceleradores de partículas hace interesante su estudio para diversas aplicaciones, principalmente en el campo de la medicina, como la radioterapia o la activación de blancos secundarios para tomografía de electrones y positrones, entre muchos otros.

Las simulaciones numéricas son una herramienta fundamental en la física de la interacción láser-plasma para el avance de este área científica, dado que nos brindan una visión más profunda de los fenómenos físicos envueltos en la interacción y pueden ser empleadas para el diseño de experimentos o para la predicción de resultados en regímenes de no fácil acceso desde el punto de vista experimental. El empleo de códigos particle-in-cell (PIC) está muy extendido en este campo científico, debido a la simplicidad de sus fundamentos teóricos y a su demostrada capacidad para proporcionar resultados fiables, que pueden ser contrastados con resultados experimentales. Estos códigos asumen que el total de las partículas cargadas que componen el plasma pueden ser agrupadas en un número menor de macropartículas, y teniendo esto en cuenta, resuelven en una malla numérica regular, en la que se localizan los campos electromagnéticos y las partículas, las ecuaciones de Maxwell y la ecuación de Lorentz para el cálculo de los campos electromagnéticos y de las propiedades dinámicas de las partículas, respectivamente. Las fuentes de los campos electromagnéticos son las densidades de carga y corriente, que se calculan a través de la posición y momento de las partículas, que a su vez son obtenidas por el efecto de los propios cam-

pos. La resolución numérica de las ecuaciones se realiza de una forma cíclica con un incremento temporal escogido apropiadamente, de tal forma que, tras varios ciclos sea posible obtener la evolución temporal de la interacción entre un pulso láser y un plasma en la escala temporal de interés.

En esta tesis mostramos los resultados de simulaciones numéricas para el estudio de varios fenómenos asociados a la interacción láser-plasma: la generación de armónicos de orden alto y la producción de pulsos de attosegundo, donde proponemos varios posibles caminos para la manipulación de las propiedades del tren de pulsos de attosegundo; la aceleración de protones a través de la interacción entre láseres de alta intensidad y blancos sólidos, donde evaluamos las propiedades del uso de blancos nanoestructurados y encontramos que estos blancos son capaces de incrementar substancialmente la energía láser absorbida por el plasma y la energía cinética de los protones acelerados; y otros fenómenos en los que la interacción láser-plasma juega un papel fundamental, tales como la amplificación local del campo eléctrico que tiene lugar en nanoestructuras, encontrando que esta amplificación puede ser empleada para la manipulación de las propiedades del espectro de armónicos emitido por un gas encapsulado en la nanoestructura, a través de efectos de *phase matching*.

En cuanto a la generación de armónicos de orden alto, en primer lugar se introducen sus propiedades espectrales y espaciotemporales fundamentales, junto con una explicación teórica del fundamento de su generación. Posteriormente se introducen las dependencias de este mecanismo en relación a algunas propiedades del pulso láser o del plasma, tales como la intensidad pico del láser, su estado de polarización y su orientación espacial, la densidad del plasma, el ángulo de incidencia del láser o la existencia de un pre-plasma en la superficie frontal del blanco.

Una vez introducido el concepto de la generación de armónicos de orden alto y resumidas sus propiedades básicas, se procede a mostrar los resultados. En primer lugar se motiva la necesidad del estudio de las técnicas de manipulación del tren de pulsos, dado que ser capaz de aislar un sólo pulso de attosegundo, manipular el estado de polarización

de los armónicos, o controlar la intensidad de estos es útil para varias aplicaciones en las que estas fuentes de radiación son empleadas, tales como el sensado de muy alta resolución, la física de materiales o el estudio de la dinámica electrónica a escalas atómicas.

Para la manipulación del número de pulsos emitidos en el tren y, en el caso más óptimo, el aislamiento de un sólo pulso de attosegundos, se presentan dos trabajos diferentes. En el primer trabajo se implementa una variante de la técnica conocida como *Polarization Gating*, la cual hace uso de la dependencia de la generación de armónicos con la elipticidad del pulso láser (siendo más óptima para polarización lineal P y menos óptima para polarización circular), de forma que con un pulso láser con una elipticidad dependiente del tiempo es posible acotar el número de pulsos del tren. En particular se utiliza un pulso con polarización lineal en la región central más intensa y circular fuera de esta región. La variante propuesta se caracteriza por el empleo de un fenómeno no lineal conocido como *Cross Polarized Wave Generation*, mediante el cual a la salida de un cristal no lineal que atraviesa el láser, se genera un pulso con polarización lineal, cuyo eje es dependiente del tiempo. La adición de una dispersión de segundo orden en un eje de los campos a la salida del cristal y el uso una lámina de cuarto de onda permiten que, para un pulso láser de varios ciclos e intensidad moderada, se pueda aislar un pulso de attosegundo en el caso más óptimo.

En la segunda propuesta se introduce una nueva técnica para el aislamiento de pulsos de attosegundo, que se ha bautizado como *Frequency Gating*. Esta técnica consiste en el uso de un pulso láser obtenido como suma coherente de dos pulsos láser con la misma envolvente pero con una ligera diferencia entre el valor de sus frecuencia centrales, lo que genera una onda resultante como producto de una onda de frecuencia rápida y otra de frecuencia lenta. Si la frecuencia lenta es tal que su período de oscilación esté en el orden de la longitud del pulso, entonces se genera un patron de pulsado en el campo láser que, a efectos de la generación de armónicos, acorta en términos efectivos el tren de pulsos de attosegundo. Se estudia cómo se comporta esta técnica para diferentes anchuras del pulso láser, encontrando que el ratio óptimo entre frecuencias para el aislamiento de un sólo pulso de attosegundo, así como

la eficiencia de aislamiento de este, depende de la longitud temporal del pulso láser, pudiendo modelizar esta dependencia de forma sencilla. También se ha comprobado que el buen funcionamiento de esta técnica requiere del uso de pulsos de alto contraste y de un buen control sobre la fase relativa entre los dos pulsos láser. Los resultados muestran que este método consigue de forma muy eficience acortar el tren de pulsos de attosegundo, siendo posible incluso para pulsos láser multiciclo el aislamiento eficiente de un solo pulso de attosegundo.

Por último se presentan resultados relativos a la manipulación del estado de polarización del espectro de armónicos, tomando como base resultados recientes que demuestran que un pulso láser con polarización elíptica en incidencia oblicua genera armónicos también polarizados elípticamente. Mediante el uso del modelo teórico *Relativistic Electronic Spring* (RES) para la generación de armónicos, caracterizado por su validez a muy altas intensidades láser, se realiza un estudio paramétrico extenso en el que se analiza la elipticidad del tren de pulsos de attosegundo para diferentes estados de polarización y ángulos de incidencia del láser. Los resultados muestran por primera vez las configuraciones que generan en particular pulsos de attosegundo con polarización cuasi circular y prueban que, dada la concentración local de la emisión de los armónicos en el régimen de intensidades estudiado, se pueden alcanzar, en ciertas configuraciones, pulsos de attosegundo con polarización próxima a la circular y amplitudes en el orden de magnitud de la amplitud del pulso láser original, lo cual supone una gran motivación para aplicaciones en las que estos se puedan emplear.

En esta tesis también se aborda el estudio de la aceleración de protones a través del mecanismo conocido por *Target Normal Sheath Acceleration* (TNSA). En este escenario los electrones son empujados por la fuerza ponderomotriz del campo láser a lo largo del blanco, escapando a través de su superficie posterior y creando una separación de carga en esta superficie con una distancia micrométrica. Esta situación genera un campo longitudinal muy intenso capaz de acelerar eficientemente partículas con carga positiva localizadas en dicha superficie posterior, generalmente protones provenientes de hidrógeno atmosférico depositado en una fina capa sobre el blanco. Se introduce este mecanismo de

aceleración y se explican sus propiedades, mostrando como ejemplo el resultado de una simulación numérica.

Se motiva la necesidad de mejora de las propiedades del haz de partículas acelerado, en general en términos de energía máxima y carga acelerada, sin incrementar para ello la intensidad del láser, dado que esto implica un aumento notable en el coste del experimento. Se discuten las distintas propuestas en la literatura científica para mejorar el proceso de aceleración a través de la manipulación de las propiedades del blanco, encontrando que el empleo de blancos nanoestructurados de forma regular en su superficie frontal mejora substancialmente la absorción de energía del pulso láser por parte de los electrones, lo cual se traduce en un aumento de la energía de los protones acelerados. En estos estudios de blancos nanoestructurados se encuentra que la estructura que permite una absorción de energía mayor es la triangular, por lo tanto se decide realizar un estudio en profundidad de las propiedades de dicha estructura.

Empleando los parámetros del láser *STELA* de la plataforma *L2A2* de la *Universidade de Santiago de Compostela*, estudiamos el proceso de aceleración de protones con blancos nanoestructurados triangulares. Los resultados muestran que, tanto la absorción de energía como la energía de los protones dependen fuertemente de las dimensiones de la nanoestructura y del ángulo de incidencia del láser, pudiendo optimizarse para dar una absorción de energía casi total y obtener una mejora en un factor 5 de la energía de los protones en comparación con la obtenida cuando se utiliza un blanco de superficie plana. Los resultados relativos a la absorción de energía y a las dimensiones óptimas de la nanoestructura son respaldados por un modelo teórico y analítico basado en el movimiento relativista de los electrones en la nanoestructura periódica bajo la influencia del campo láser.

Por último se estudia el comportamiento de estos blancos en términos de la absorción de energía, para situaciones más realistas, considerando posibles desviaciones de la situación ideal, tales como la existencia de diferentes especies de iones, fluctuaciones en la intensidad pico del pulso láser, errores en la periodicidad de la nanoestructura y la existencia de una región de pre-plasma. La motivación para la realización de este

estudio es la de certificar cómo de robustos son los resultados obtenidos y cómo de precisa ha de ser la técnica de fabricación de las nanoestructuras (lo que repercute en su precio). Los resultados de esta última parte revelan que los resultados son muy robustos frente a desviaciones de la situación ideal en términos de diseño del experimento, siendo posible por ejemplo emplear una nanoestructura con errores de fabricación del 50% del valor de sus dimensiones, y que esto implique un cambio en la absorción de energía de aproximadamente un $\sim 2\%$. También se encuentra que estos blancos requieren del empleo de pulsos láser de muy alto contraste, para evitar la formación de un pre-plasma, el cual demuestra ser muy perjudicial para obtener altos porcentajes de absorción, en consonancia con lo que se ha publicado en la literatura.

La última sección de resultados se dedica a la generación de armónicos de orden altos en medios gaseosos, cuando dichos medios se encuentran encapsulados en un volumen nanométrico delimitado por una nanoestructura formada por dos bloques separados entre si. En esta situación la interacción láser-plasma representa más una herramienta que el fenómeno a estudiar en si mismo.

Para contextualizar los resultados del último capítulo, primero se introduce el fenómeno de la generación de armónicos de orden alto y pulsos de attosegundo en medios gaseosos. Se explica dicho fenómeno a un nivel atómico con un modelo semiclásico, basado en el movimiento de los electrones bajo el efecto del campo láser alrededor de un ion cargado positivamente, y se explica por qué estos armónicos son emitidos y cuáles son sus propiedades principales. Se calculan las trayectorias de los electrones para los cuales la recolisión con el ion ocurre y se introduce el concepto de trayectorias largas y cortas, en función de cuando se produce la recolisión con respecto a la trayectoria óptima, para la que se emite la energía máxima. Una vez realizada la explicación microscópica de este mecanismo, se generaliza para el caso macroscópico, en el cual se tiene en cuenta que la muestra gaseosa está compuesta de un gran número de átomos que emiten radiación con diferentes amplitudes y fase, y que la suma coherente de cada contribución individual proporciona la señal final a medir en un experimento. A la sazón de esta descripción macroscópica, se introducen los efectos de *phase matching*, los cuales se definen como

los efectos a nivel macroscópico que producen las diferencias de fase entre la emisión de los armónicos por los átomos en la muestra. Se discuten las diferentes fuentes que puedan ser responsables de dichos efectos, tales como la geometría del experimento o el balance entre las trayectorias largas y cortas presentes en el experimento. En el último caso dicha contribución de fase es conocida como fase intrínseca.

Una vez explicada la generación de armónicos en medios gaseosos, se introduce el concepto de las oscilaciones plasmónicas, dado que es necesario para la comprensión de los resultados mostrados en la parte final del capítulo. Se explica su origen y significado, así como sus aplicaciones y propiedades más generales. El concepto de la oscilación plasmónica causada por un campo láser sobre la superficie de un plasma de densidad sólida nos permite proponer una configuración en la cual dos superficies de espesor ultrafino se separan una distancia mucho menor que la longitud de onda, tal que un pulso láser incide sobre dicha separación, linealmente polarizado en la dirección en la que dichas superficies se separan. La separación de carga generada por el movimiento de los electrones sobre el fondo de iones pesados en reposo, causa que se creen en las superficies paralelas opuestas una acumulación de carga de signo contrario e igual magnitud, lo que a efectos prácticos se puede describir como un capacitor a escala nanométrica. Este fenómeno mejora el campo local en el volumen de separación entre ambos materiales, dado que el campo generado está en fase con el campo láser original, sumándose por tanto a este. Las propiedades de este mecanismo para la mejora local del campo eléctrico se estudian atendiendo a la polarización e intensidad del láser, así como a las dimensiones del diseño, encontrando cuales son las limitaciones de este mecanismo y su comportamiento en relación a estos factores. Para finalizar, se muestran los resultados de la generación de armónicos por un gas localizado en un volumen nanométrico limitado por una estructura similar a la descrita anteriormente. El campo en la estructura se ve incrementado hasta en dos órdenes de magnitud en intensidad, lo cual puede ser empleado para la mejora de la generación de armónicos con campos láser de baja intensidad. El empleo de códigos particle-in-cell nos permiten obtener la distribución exacta del campo en la estructura, la cual se puede emplear para calcular la emisión del

espectro de armónicos. Los resultados revelan que, al contrario de lo que es típicamente asumido en estas configuraciones, los efectos de *phase matching* son relevantes y que además la fuente de los desajustes de fase no es otra que la fase intrínseca, causada por la inhomogeneidad de los campos en la nanoestructura, por lo tanto este efecto estará presente siempre que se empleen nanoestructuras con el fin de generar ármonicos con gases.

La tesis finaliza con una relación de conclusiones, en las que se recogen de forma detallada los resultados obtenidos en cada uno de los capítulos.

USC
UNIVERSIDADE
DE SANTIAGO
DE COMPOSTELA

SHORT SUMMARY

The advancements in laser technology over the last decades have allowed researchers to explore new regimes of physics, discover new phenomena and implement several new applications. This has made lasers into an essential tool in nowadays society, with an extensive socioeconomic impact in many areas. High power femtosecond lasers were first developed in the 1980s, and the achievable peak powers have grown substantially ever since. These pulsed laser sources have enough power to ionize a solid material in a femtosecond temporal scale, being able to interact with the plasma formed at the material surface. Laser-plasma interaction between high power lasers and solid density plasmas provides with the tools to create high frequency ultrashort pulsed radiation, close to the X-ray regime and with temporal lengths in the attosecond scale, and allows to create compact and cheap particle accelerators, that can represent an advantage in some scientific areas in comparison with conventional accelerators.

Numerical simulations are a fundamental tool in laser-plasma physics for the advancement of this scientific area, since they provide with insights of the physical processes involved in the interaction and they can be used to design experiments or predict results in regimes not easily available from the experimental perspective. In this thesis we show the results of numerical simulations to study several phenomena associated with laser-plasma interaction: high harmonic generation and its associated attosecond pulse production, where we propose several routes to manipulate the properties of the attosecond pulse train; proton acceleration through the interaction of high intensity laser pulses and solid targets, where we address the properties of using nanostructured targets, finding that these targets are able to increase substantially the laser energy absorbed by the plasma and the kinetic energy of the accelerated protons. We also analyze other phenomena in which laser-plasma interaction plays a key role, where we study the local enhancement of the laser electric field in nanostructures and we find that this enhancement can be

used to manipulate the properties of the harmonic spectrum emitted by a gas enclosed inside the nanostructure, via phase matching effects.

KEYWORDS

lasers, ultraintense lasers, plasma physics, laser-plasma interaction, particle-in-cell simulations, high harmonic generation, attophysics, ultrafast physics, plasma-based particle acceleration, proton acceleration, target normal sheath acceleration, plasmon oscillations, phase matching effects in high harmonic generation

1 INTRODUCTION

The interaction between light and matter has always fascinated human beings. From the very beginning of our existence, light and its interaction with matter have been a central piece of culture and science in societies. Starting from the early scientific theories of the XVII and XVIII centuries, the increasing advancement of the understanding of this scientific field allowed the development of new technologies, which in turn helped to develop new and more complete theories that brought us to the world that we live in. Nowadays the scientific and technological development in the fields of radiation-matter interaction is so big and so specialized, that in some research areas we are on the verge of analyzing previously unreachable scales of energy, intensity or resolution, that will most likely bring to light new physical phenomena previously ignored and give rise to a new and more complete scientific understanding of nature.

The invention of the laser in 1960 and its fast evolution have made possible to be able to have nowadays terawatt (10^{12} W) radiation sources in the visible and infrared part of the spectrum and with temporal lengths in the range of the femtosecond scale, available for a reasonable price. Even petawatt (10^{15} W) laser sources have been developed in some laboratories around the world. The high levels of irradiance ($I \gtrsim 10^{18}$ W/cm^2 or $a_0 \gtrsim 1$ in dimensionless units where $a_0 = 0.85(I\lambda^2/10^{18}\ Wcm^{-2}\mu m^2)^{\frac{1}{2}}$) that can be achieved with these powers when the laser pulse is tightly focused in a micrometric area, can strongly ionize solid materials and create high density plasmas to interact with. Furthermore, these irradiances are beyond the relativistic limit, that means that an electron affected by these fields will show a relativistic behaviour, giving rise to a nonlinear interaction that has as a result phenomena that prior to the development of these systems was unknown.

In this thesis, we study the interaction between high intensity laser pulses and ionized solid materials, or overdense plasmas, with particle-in-

cell (PIC) simulations. Laser-plasma interaction in the relativistic limit has highly increased its interest in the last decades [1–3]. It has been a way to obtain new intense radiation sources beyond the ultraviolet part of the spectrum [4, 5] as well as a method for producing energetic beams of electrons, from the Laser Wakefield Acceleration (LWFA) mechasim, and ions, from the Target Normal Sheath Acceleration (TNSA) mechanism [6, 7], as principal and most developed acceleration mechanisms. These are nowadays starting to be used in several applications, such as X-ray production, target nuclear activation, hadrontherapy, probing or sensing.

The aim of this PhD thesis is to study the interaction of high intensity and ultrashort laser sources with solid ionized materials, with the purpose of extending previous works, proposing new experiments, exploring new practical applications and obtaining a better understanding of the physical processes present. We analyze the nonlinear mechanisms involved in this interaction and we focus our attention into the study of two of its most important outcomes: the generation of high harmonics of the laser central frequency and the associated attosecond pulse generation in the reflected field [4, 5] and the acceleration of ions at the back surface of a solid target caused by its interaction with an ultrashort and intense laser pulse [6, 7]. Apart from these topics, we address other topics where laser-plasma physics produces interesting physical phenomena.

The results derived from this thesis provide a better understanding of the interaction between laser pulses and overdense plasmas at the nanoscale level. In one hand, they will allow to implement new experiments to isolate single attosecond pulses and to manipulate their polarization state, in the other hand, they will help to obtain the optimal parameters of nanostructured solid targets for achieving more efficient proton sources from plasma accelerators. The results will find their applicability in several technological fields, such as high precision sensing with attosecond resolution, atomic science with ultrashort and non-linearly polarized pulses, improvement of the target activation methods for positron emission tomography, and so on.

1.1 ATTOSECOND PULSES AND HIGH HARMONIC GENERATION

The generation of ultrashort radiation, through the interaction of a laser pulse with a gas or solid target, has been a very active research field in the last decades, yielding to very interesting results in basic and applied science [4,5,8]. The generation of this kind of pulses is linked to a nonlinear mechanism, known as high harmonic generation (HHG), by which integers of the laser central wavelength are generated and emitted as a consequence of the interaction of a laser pulse with a target.

In gas media, HHG is a nonlinear effect caused by the motion of electrons at the atomic scale due to the effect of an external laser field [8–18]. The periodic recollision of electrons with their parent ions during their oscillations generates a train of ultrashort bursts of radiation with a wide harmonic spectrum. HHG produced by this method is limited by the intensity of the laser and therefore not very high efficiencies or energies can be achieved in comparison with the case when solid targets are used [18].

The generation of high harmonic orders when focusing an intense laser pulse in a solid target was first discovered in the 1970s [19], and then reproduced and studied by other groups in the following years [20–23]. In these studies several interesting features of HHG were found: harmonics appeared at integer multiples of the laser central frequency; the motion of electrons at the plasma surface was responsible for their generation and the spectrum showed a cutoff at the maximum local electron plasma frequency, defined by the equation $\omega_{pl} = \omega(n/n_c)^{\frac{1}{2}}$, where n is the plasma density and $n_c = \varepsilon_0 m_e \omega^2 / q_e^2$ the critical density, being ε_0 the vacuum permitivity and m_e, q_e the mass and charge of the electron, respectively. With the advent of high power lasers, HHG in solid targets gained interest as it was demonstrated at intensities where gas HHG was not possible anymore ($I \gg 10^{16}$W/cm^2), both in experiments and numerical simulations [24–27], showing new features of this generation, such as the disappearance of the harmonic cutoff at relativistic intensities and the temporal shape of the harmonic spectrum in the form of attosecond pulses.

The generation of high harmonic orders in solid targets occurs during

the interaction between a laser pulse and the ionized surface of the target, such that ultrashort bursts of radiation containing the harmonic spectrum appear periodically with the laser field oscillations in the reflected field. This mechanism for HHG is fundamentally relativistic and associated to the motion of electrons at the plasma surface, caused by the external laser field. There are several models to explain this mechanism in solid targets, all of them based on the electron dynamics at the plasma surface in different parametric configurations. A short description of the basis of these models is the following: the pre-pulse or the front part of the laser pulse ionizes the target surface, generating a high density plasma with a frontal region of density growth (pre-plasma); the laser pulse interacts with the plasma, moving electrons at relativistic velocities, and gets reflected carrying harmonic radiation generated by the particle motion at the target surface. The nonlinearity that governs this mechanism causes that models usually cannot yield to final analytical expressions that describe explicitly the harmonic spectrum and they have to be solved numerically under certain approximations. Therefore, the dependency of HHG in several parameters such as the laser polarization state is not obvious and has to be inspected by performing numerical simulations. The best established models to account for HHG are the Coherent Wake Emission (CWE) model [28], the Relativistic Oscillating Mirror (ROM) models [27] and the Relativistic Electronic Spring (RES) model [29], having each of them its range of applicability in terms of the laser and plasma properties.

The CWE model is designed for moderate laser intensities ($I \leq 10^{18}$ W/cm^2 or $a_0 \leq 1$), where relativistic effects in the electron motion are not dominant and the source of HHG is the variation over time of the electron density profile. The oscillatory motion of electrons at the surface of an overdense plasma under the influence of a P-polarized laser field is described by Brunel's model [30]. It predicts that electrons starting their motion at different times under the same field, could eventually cross each other when re-entering the plasma after one laser oscillation. Since inside the plasma the velocity of the electrons is unperturbed [31], this leads to the formation of a high density peak of electrons propagating through the plasma, which excites collective electron oscillations inside

the plasma that emit radiation in the form of ultrashort pulses containing high frequency harmonics. This mechanism and its steps have been verified in numerical and experimental studies [28, 32–34] and reviewed thoroughly in reference [5]. The properties of the harmonic spectrum in the CWE regime have been analyzed through parametric scans with numerical simulations [5, 35, 36], finding a clear cutoff at the plasma frequency of the harmonic spectrum; a strong dependence of the harmonic emission on the shape and length of the pre-plasma; a cancellation of CWE harmonics at normal incidence and an optimal generation at a laser angle of incidence around 45° and, in relation to the polarization state of the laser pulse, a need for the existence of a P-polarized component in the laser pulse for CWE to be triggered.

The ROM models [27, 37–43] are a group of theoretical models designed to account for HHG at relativistic intensities ($I \gtrsim 10^{18}$ W/cm^2 or $a_0 \gtrsim 1$). They share the same ad hoc initial assumption about the plasma surface behaving as a mirror. In this regime the high laser intensity provokes a collective motion of the electrons at the plasma surface, causing a simultaneous oscillation of the laser field and the surface where it is reflected, that generates a doppler shift in the reflected field, responsible for the harmonic spectrum. The harmonic spectrum in the ROM regime also comes in the form of attosecond pulses, but presents features that were not present in the CWE regime, namely an universal scaling of the harmonic signal on the harmonic order of $\propto n_H^{-8/3}$ (where n_H is the harmonic order) with a cutoff given by $\omega_c = \gamma^3$, being γ the maximum Lorentz factor at the apparent reflection point (ARP) [39, 41]; an optimal angle of incidence in the interval $[45^\circ,\ 60^\circ]$; an explanation for the harmonic spectrum at normal incidence; an enhancement of the generation due to the presence of a pre-plasma and the existence of a set of "selection rules" that explains what is the polarization state of the harmonics depending on the polarization state of the laser pulse [27]. In this regime of intensities, the ROM described harmonics are dominant over CWE ones [33, 34], which demonstrates that the regime of relativistic intensities is much more interesting for HHG. The main assumption of this model is that at some point during the laser-plasma interaction, both incident and reflected fields compensate each other at an apparent

reflection point. Therefore this model is limited for a certain parameter region in which that statement may apply.

The RES model [29, 44], which is the most recent of these three, assumes that the shifted reflection in the ROM models is generally not true, since it neglects the accumulation of energy by the electrons during their motion, which is a relevant factor not negligible when the laser intensity is increased or the plasma density reduced. Therefore the electron plasma oscillations over the ion background have a bigger amplitude. This model takes into account the accumulated energy on the electrons over the laser oscillation and its reemision in the form of an ultrashort radiation burst, containing a harmonic spectrum. The steps followed by this mechanism during one laser ocillation are the following: the laser field pushes the electrons into the plasma bulk and stacks them into a thin high-density nanometric sheet, heating them. After that, the electrons are accelerated backwards towards their original position and finally they emit radiation when they reduce their energy at the beginnning of a new oscillation. In contrast with ROM models, this is a fully physically based model, without any prior assumption about the physical processes taking place, furthermore the elimination of the constrain of perfect specular reflection present in ROM models, allows that the reflected field may have locally a much higher amplitude than the incident field, i.e. the integrated harmonic spectrum would be locally more intense than the incident field and finally its results are also valid when pre-plasma regions are taken into account and it is not needed to assume an initial steep density profile. The parameter that controls the range of applicability of this model is the similarity parameter, defined as the quotient between the density of the plasma in units of the critical density and the dimensionless amplitude of the laser field, $S = n/a_0$. When this value is in the range $[0.05, 5]$, we can consider that we are in the RES regime, below the lower limit the relativistic self transparency (RSIT) begins to occur and above it, ROM models need to be taken into account. The predictions of this model have been tested with numerical simulations, obtaining a remarkably good agreement, however there is still a lack of studies of this regime to be able to explain the different parametric dependencies of HHG in it, mainly due to the typical high

densities of solid targets, that together with the similarity parameter in which this regime apply, require the use of very high laser intensities ($I \gtrsim 10^{21}$W/cm^2 or $a_0 \gtrsim 20$), which are still only achievable in a few laboratories around the world.

The properties of the harmonic spectrum, discussed in the previous paragraphs in the context of the present models, have been demonstrated and addressed in several numerical and experimental works. These studies confirm the existence of a plasma frequency cutoff and its disappearance by lowering the plasma density or increasing the laser intensity [33–36, 45]; the existence of the selection rules [26, 27]; the dependence of HHG on the laser polarization state [27, 46, 47]; the dependence on the pre-plasma scale-length [43, 45] and, very recently, new properties are being unraveled for HHG using targets with nanostructured surfaces [48–50].

Up to this point, it has been discussed the spectral properties of HHG in solid targets, however equally important is its spatiotemporal shape. Fourier's transform establishes that a wide spectrum corresponds to a narrow temporal shape, so the shape of these high order harmonics must be in the form of very short radiation pulses. This is the case for HHG both in gas and solid targets, in which the high harmonic orders, once filtered in a certain spectral region, appear as a train of pulses, with a temporal width in the order of hundreds of attoseconds or even below [18, 29, 38, 40, 42, 45, 47, 51]. The discovery of these sources supposed a breakthrough in science, because it unlocked the creation of controllable radiation sources below femtosecond lengths, opening a wide field of applications [8]. The manipulation of the properties of these pulses is a very interesting topic, since in this way they could be tailored for specific applications. Several techniques for their manipulation have been developed, principally devoted to the shortening of the pulse train up to the isolation of a single pulse [39, 47, 52–58], to shorten the temporal length of the pulses [38, 55], to increase their intensity [29] or to control their polarization state [59, 60].

The applications of HHG and its associated attosecond pulses are very broad. Most of the applications mentioned here are already being used with gas-generated attosecond pulses, where the degree of tunabil-

ity and control over the process is still higher, although solid-generated attosecond pulses can also be used for them, with the advantage of the availability of higher energies and intensities. These attosecond pulses can be used for several applications, such as high precision metrology, due to their very short length and XUV spectrum, allowing to study matter at previously unreachable scales, being able to measure electron cloud dynamics, ionization processes or molecular dynamics with attosecond resolution [61–67]. High harmonic orders have been also used to estimate properties of plasmas in laser-plasma interaction [68, 69], making possible to measure the spatial evolution over time of the plasma density and its temperature. An extensive list of the applications of these pulses can be found in references [8, 61] and references therein.

In summary, HHG in laser-plasma interaction is a nonlinear mechanism to obtain, in the reflected laser field, a high frequency spectral content. The nature of this generation is still under discussion, as there are three main theoretical models explaining this phenomenon for different parametric regions in terms of laser intensity and plasma density. The harmonic spectrum comes in the form of sub-femtosecond pulses, emitted periodically, typically with lengths of hundreds of attoseconds. Numerical simulations and experiments show that it is possible to manipulate the number of generated pulses, their polarization and their temporal width, meaning that these ultrashort radiation sources are tunable. HHG and attosecond pulse generation also occurs in gas targets, and the degree of control in this case is much higher because of the bigger volume of research, however the use of high intensity lasers and solid targets represents a powerful evolution due to the higher energies and intensities obtained in this way. The potential of these sources is vast and they are already being applied in several reseach fields, mainly as a sensing or imaging tool, for atomic physics experiments or for studying matter at a very small scale, however the further development of these sources will open the way for new applications and improvement of the existing ones.

1.2 LASER-BASED ION ACCELERATION

Particle acceleration in laser-driven plasma accelerators has been a very active field in the last few decades. The use of laser pulses as a mean to accelerate particles was first proposed in 1979 [70], since then, due to the fast development in laser technology, it has been demonstrated that it is possible to accelerate ions up to energies of tens of MeV with table top laser sources. A large number of applications have been proposed and implemented, and this acceleration paradigm has gained a reputation as a key tool for future technologies using energetic ions [6, 7].

There are several scenarios where ions can be accelerated by laser pulses interacting with solid targets, the main mechanisms to do so are: the Target Normal Sheath Acceleration (TNSA), the Radiation Pressure Acceleration (RPA) and its Light Sail (LS) regime and the Collisionless Shock Acceleration (CSA).

In the TNSA scenario [71], a high power laser ($I \gtrsim 10^{18}$ W/cm^2) interacts with a few-micron thick solid target to produce energetic ions. The laser pulse ionizes the target surface and heats up the electrons; these electrons propagate across the target and escape perpendicularly to the rear surface, generating a space charge separation in the rear surface that yields a strong longitudinal field [72]. This field can accelerate positively charged particles located in the vicinity of the surface. These particles usually come from a contamination layer in the back surface of the target, and are usually protons caused by the effect of atmospheric hydrogen. However even without that layer, bulk heavy ions can be still accelerated [73–75]. The strength of the longitudinal field and thus the efficiency of the acceleration process depends on several factors, mainly related to the electron cloud properties (density, energy or spatial distribution). Several fenomenological models [71, 76–83] have proposed explanations and scaling laws to be able to make theoretical predictions, but all of them agreeing about the different steps involved in the acceleration process.

The RPA mechanism is a process by which ions initially in the front surface of the target, where the laser pulse is focused, are accelerated [84–90]. In this case the ponderomotive force acting upon the target surface steepens remarkably the density profile by pushing it deeply

inwards (process known as hole boring), generating a double layer of particles (ions and electrons) moving with a velocity known as recession velocity or hole boring velocity, so that the charge separation due to the pushing of the electrons accelerates the ions in the front surface of the target. This description of the RPA process is present in several theoretical and numerical studies [91–94]. The particle energy scaling with the laser peak intensity for RPA is stronger than for TNSA [95–97], which suggests that RPA should be more relevant at much stronger intensities than the ones typically used in TNSA studies (see figure 21 in reference [6]). The RPA mechanism is applicable for micrometric thick targets, however when the target becomes ultrathin, the LS regime takes over. In this situation the target is thin enough that the hole boring is able to reach the end of the target and the laser pulse removes all the bulk electrons, allowing ions to propagate freely further [98–101], the potential of this regime is important, but the need for very high laser intensities and extremely thin targets is within current technological limitations.

The CSA acceleration mechanism [102] relies on the formation of electrostatic shocks in an overdense plasma, that propagate through it accelerating the ions to high Mach numbers. This acceleration mechanism has been studied experimentally and numerically [102–106], and it has been discovered that it can contribute to increase the ion energy when both CSA and TNSA take place [104, 105].

TNSA is the most robust and controllable method that exists nowadays, for the typical laser powers commercially available and using solid targets, as demonstrated by the large number of publications studying its properties [71–83, 97, 107–111]. These ion sources are obtained via pulsed laser systems, therefore their temporal and spatial properties mimic the ones from the laser pulse, that means they are pulsed ion sources with a short temporal length, a very small spatial size, a sharp angular distribution and a clear directionality [108, 110]. Furthermore, they show a broad spectrum with a clear cutoff [110] and a low emittance [112–114]. Several studies in the last years have developed ways to enhance some of these advantageous properties, like increasing the ion energy, enhancing the laser energy absorption, or collimating the ion

beam, among others [115–124]. These characteristics represent a way to implement new applications, taking advantage of the ion source special properties or reduced price in comparison to traditional high energy ion sources, such as cyclotrons.

The applications of these ion sources are very broad. For example ion probing and sensing, where thanks to these sources it has been possible to make precise electromagnetic field measurements in laser-plasma experiments [72,125–133]; to implement proton radiography as a precise imaging method for ionized materials [134–136]; to measure particle properties [137, 138] and to be a diagnostic tool in inertial confinement fusion (ICF) experiments [139–141]. In the biomedical field there are also many applications, such as: hadrontherapy, that uses these ion sources to reduce the damage in the surrounding non-tumoral tissue or to address their effect in cancer cells [142–150] and imaging applications in Positron Emission tomography (PET) [151–153], allowing to use more specific tracers, versus those produced by conventional cyclotrons, to detect different kinds of diseases. Laser-plasma ion acceleration is also used in the context of the intertial confinement fusion (ICF) [154], to implement what is known as proton fast ignition (FI) [155–161], where accelerated protons are used to trigger nuclear fusion. More fundamental and research applications have been also studied with these sources, such as research on warm dense matter (WDM) [162–166], nuclear physics [167–173] and particle physics [174–176].

In summary, laser-based ion acceleration using high power lasers and solid targets is a scientific field that has grown enormously during the last decades, and it has opened a way to obtain cheap, controllable and energetic beams of ions, suitable for a big variety of applications, both in basic science and industry. The impact of this new particle acceleration paradigm is yet to be seen, but it is already clear that it will contribute significantly to the advancement of future technologies.

1.3 THESIS OUTLINE

This thesis is structured as follows: Chapter 1 gives a general introduction of the scientific context and state-of-the-art of the topics related to laser-plasma interaction developed in this work. Chapter 2 describes

the numerical tools employed to develop the work present in this thesis. The results obtained for HHG and attosecond pulses are described in chapter 3. The results for ion acceleration are explained in chapter 4 and other results where laser-plasma interaction plays an important role are developed in chapter 5. Finally, we present the conclusions.

2 NUMERICAL TOOLS

Laser-plasma interaction and its outcomes have been proved and developed in several experiments, where it has been possible to demonstrate theoretical or simulation predictions. The increasing availability of high intensity table-top laser sources has made possible to increase the volume of experimental research and it is paving the way for the industrial implementation of the applications of laser-plasma interaction. The set of parameters to study in laser-plasma physics problems is huge, since it is possible to tune several parameters related to the laser pulse, the target where the plasma is formed, the geometry of the experiment and the detection and data analysis methods, all of this taking into account that there are some technological limitations that do not allow to explore some interaction regimes. In light of these facts, it is virtually impossible to perform extensive experimental studies in a wide parametric region without finding technological limitations or producing a very increased cost to perform the experiments.

To overcome experimental limitations and to be able to analyze scenarios difficult to access in a laboratory, and also to explain the scientific foundations of what is found in experiments, there is a high volume of theoretical papers modeling laser-plasma interaction to explain the several outcomes that were described in the introduction. However the very high nonlinearity of high intensity laser-plasma interaction, due to the relativistic velocities at which electrons move under the influence of intense laser pulses, makes very hard to obtain analytical equations or a full description of the phenomenon to address, being most of the times necessary to use approximations and assumptions to obtain partial solutions. This faces us with a similar problem to the one described in the previous chapter, these models can only account for a certain region of the parameter space or a specific setup, therefore they cannot give a full picture of the physical mechanisms involved, neither an exact prediction for what is to be found experimentally outside of the parameter space for which they are designed.

Because of the previously explained, the use of numerical simulations to investigate laser-plasma interaction appears as a natural solution, since knowing the fundamental equations that govern this interaction it is possible to solve them numerically and to explore all the possible regimes of interaction for a specific purpose, therefore giving a wider overview of the problem to analyze, acting as a support for theoretical models and assisting experimentalists into developing new experiments. Laser-plasma numerical simulations are usually performed through the particle-in-cell (PIC) formalism [177, 178]. This is based on the solution of Maxwell's equations and Lorentz's equation on a regular grid, in which charged particles and electromagnetic fields are defined. PIC codes have proven to be very useful to support for experiments; to propose new setups for enhancing a specific output or to understand the physics underlying a certain physical phenomenon.

2.1 BASIC ASSUMPTIONS

To carry out the simulations presented in this work, it was necessary to make the following assumptions:

- The material with which the laser pulse interacts has been ionized before the pulse arrival by the pre-pulse or the laser front pedestal. This is a safe assumption taking into account that the barrier suppression ionization (BSI) mechanism, responsible for ionization in laser-plasma experiments, occurs at much lower peak intensities ($\sim [10^{14} - 10^{16}]$ Wcm^{-2}) than the relativistic ones considered in this work ($I > 10^{18}$ Wcm^{-2}) [179–183].

- The effect of collisions between particles (t_{col}) has been neglected since all the thesis results occur in time scales below 1 ps. This can be assumed taking into account that t_{col} is given by [184]:

$$t_{col} \approx \frac{4\pi\varepsilon_0^2 m_e^{\frac{1}{2}} \left(K_B T_e\right)^{\frac{3}{2}}}{n_e q_e^4 \log(\Lambda)} \tag{2.1}$$

  where n_e is the electron number density, T_e the electron temperature, $\Lambda = 4\pi \left(\varepsilon_0 K_B T_e\right)^{\frac{3}{2}} q_e^{-3} n_e^{-\frac{1}{2}}$ is the plasma parameter

and K_B is Boltzmann's constant. Assuming relativistic electrons $T_e \approx m_e c^2/K_B$, with a solid density of $n_e = 200 n_c$ for a wavelength of 800 nm, that is $n_e = 3.4 \cdot 10^{23}$ cm^{-3}, the logarithm of the plasma parameter is $\log(\Lambda) = 15$, and the mean free time between collisions is $t_{col} = 6.5$ ps.

- The particles that form the plasma can be grouped into macroparticles in order to reduce the computational needs of the simulations, this is an intrinsic assumption for the PIC formalism.

  The distribution function of a particle species in a plasma is given by Vlasov equation, that for a collisionless system is [184]:

$$\partial_t f + \vec{\nabla}_{\vec{r}} \left(\frac{\vec{p}}{m\gamma} f \right) + \vec{\nabla}_{\vec{p}} \left(\vec{F} f \right) = 0 \tag{2.2}$$

  where $\vec{r}$ and $\vec{p}$ are the particle position and momentum, m its mass, $\gamma = \sqrt{1 + \vec{p}^2}$ the relativistic factor and $\vec{F} = \frac{d\vec{p}}{dt} = q \left(\vec{E} + \frac{\vec{p}}{m\gamma} \times \vec{B} \right)$ is the Lorentz force. f gives the density distribution and the mean velocity by integrating it over the momentum space: the expressions $n(\vec{r},\ t) = \int f(\vec{r},\ \vec{p},\ t) d^3p$ and $\vec{u} = \frac{1}{n} \int \vec{v} f(\vec{r},\ \vec{p},\ t) d^3p$, respectively, give the particle number density and the average velocity, that are related to the charge and current densities in the plasma.

  The PIC method, to numerically calculate the charge and current densities, discretizes the distribution function as a sum of N individual distribution functions:

$$f(\vec{r},\ \vec{p},\ t) \equiv \sum_{k=0}^{N} g(\vec{r} - \vec{r}_k) h(\vec{p} - \vec{p}_k) \tag{2.3}$$

  where the functions g and h express the spatial and momentum distribution of each individual particle. It is numerically impossible to simulate the exact number of particles present in the plasma. For example in a volume of 1 μm^3 of a material with a density

of $3.4 \cdot 10^{23}$ cm^{-3} there would be $3.4 \cdot 10^{11}$ particles. To avoid this inconvenience and be able to compute numerically the plasma evolution, the total number of individual particles is grouped in N macroparticles, which behave like individual particles and therefore their evolution can be computed with Lorentz's equation. Each macroparticle contributes to the plasma density as the number of individual particles it represents. If this number N is high enough, the numerical fluctuations arising from this assumption are negligible.

2.2 UNIT SYSTEM

Physical quantities in PIC codes are normalized to make them unitless. The normalization relies on two main parameters, the laser central frequency (ω) and the plasma critical density (n_c), related by the equation $n_c = \varepsilon_0 m_e \omega^2 / q_e^2$. Table 2.1 details the conversion factors for the different physical quantities, where the unitless version is indicated with a tilde ($\sim$).

Table 2.1: Transformations to have an unitless system.

Time	$\tilde{t} = \omega t$
Position	$\tilde{z} = \frac{\omega}{c} z$
Momentum	$\tilde{p} = \frac{1}{m_e c} p$
Electric field	$\tilde{E} = \frac{\lvert q_e \rvert}{m_e \omega c} E$
Magnetic field	$\tilde{B} = \frac{\lvert q_e \rvert}{m_e \omega} B$
Particle density	$\tilde{n} = \frac{n}{n_c}$
Charge density	$\tilde{\rho} = \frac{\rho}{n_c \lvert q_e \rvert}$
Current density	$\tilde{J} = \frac{1}{n_c \lvert q_e \rvert c} J$
Temperature	$\tilde{T} = \frac{K_B}{m_e c^2} T$

In this work, unless stated otherwise, this particular unitless system will be used in all the displayed equations.

2.3 PIC ALGORITHM

The starting point of the PIC algorithm is to discretize the distribution function obtained from Vlasov equation. In this way it is possible to build the macroparticle concept and compute efficiently the evolution of charged particles under the influence of electromagnetic fields.

In PIC simulations, first the simulation is initialized, this means that all constants and parameters relative to the simulation are set, the spatial grid is established, the external EM fields (if there are any) are initialized and the particles' initial spatial and momentum coordinates are defined. After we enter a loop, to be ran as many times as desired and controlled by a time increment of Δt in each iteration. This loop consists on the following steps, illustrated in figure 2.1:

1. Based on the number, position and velocities of all the particles, the charge density and the current density are computed along the spatial grid.

2. Knowing the charge and current densities and the initial external fields if there are any, Maxwell's equations are solved to update the electromagnetic fields.

3. The fields are defined on the spatial grid and they act upon the particles, located in space with a chosen spatial distribution, therefore these fields must be interpolated to obtain the exact value acting on each particle.

4. Once calculated the field strength acting upon each particle, the particles' new positions and velocities can be computed by solving Lorentz's equation.

5. The new updated positions and velocities of the particles allow to recalculate the charge and current densities and return to the beginning of the simulation loop. At this point the user can print out data to a file to analyze afterwards.

After describing the basics of the PIC algorithm, we will describe further the details of each of the steps in the simulation loop.

2.3.1 Charge and current densities

It should be noted that particles and fields are defined in a spatial grid, but not in a momentum grid, this is because it is assumed that, while the spatial distribution of a macroparticle cannot be puntual to

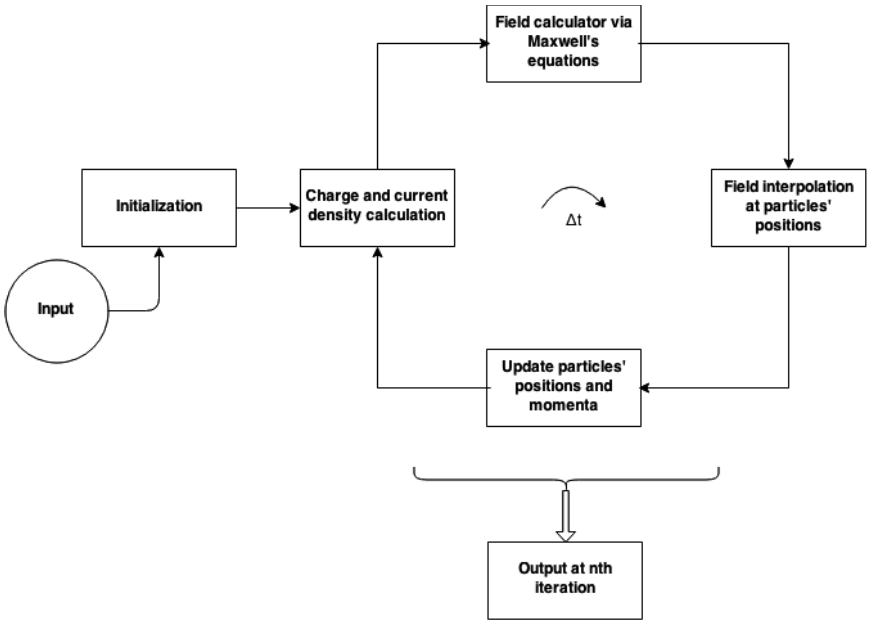

Figure 2.1: Diagram describig the steps followed in a PIC simulation.

account for the non-zero size of the particles and for numerical reasons that we will address after, it is safe to assume that the macroparticle has a clear defined momentum, therefore the discretized distribution function in equation (2.3) can be rewritten as:

$$f(\vec{r},\ \vec{p},\ t) \equiv \sum_{k=0}^{N} g(\vec{r} - \vec{r}_k)\delta^3(\vec{p} - \vec{p}_k) \tag{2.4}$$

where $\delta^3(\vec{x})$ is Dirac's three dimensional delta function. This allows to rewrite the charge and current density equations for a given particle species as a finite sum of N elements:

$$\rho = q \int f(\vec{r},\ \vec{p},\ t) d^3p = q \sum_{k=0}^{N} g(\vec{r} - \vec{r}_k) \tag{2.5}$$

$$\vec{J} = q \int \vec{v} f(\vec{r},\ \vec{p},\ t) d^3p = q \sum_{k=0}^{N} \vec{v}_k g(\vec{r} - \vec{r}_k) \tag{2.6}$$

The charge and current densities must obey the continuity equation $\partial\rho/\partial t + \vec{\nabla} \cdot \vec{J} = 0$, and in order to have a correct implementation for the current deposition this equation must be verified. A full description of how this is done can be found in reference [185].

The initial density profile is built by distributing the particles in the spatial grid. The initial distribution of the particles can be done in several ways, for example initializing particles regularly in the grid or locating them randomly with a rejection algorithm. Regardless of the path followed to build the initial density profile, the number of macroparticles and the spatiotemporal resolution have to be sufficiently high to avoid numerical errors. The number of macroparticles in the simulation can be controlled by fixing the total number of macroparticles at the beginnning or by defining a parameter named "particles per cell", that represents the initial number of macroparticles per cell.

If we neglect some spatial dimensions, to perform not three dimensional simulations, an additional parameter has to be added in order to have the correct dimensions in the simulation and to address for the density in the neglected dimensions. This extra density is defined as:

$$\sigma_{1D} = \frac{1}{N} \int n(x) dx \ \ [m^{-2}] \tag{2.7}$$

$$\sigma_{2D} = \frac{1}{N} \int \int n(x,y) dx dy \ \ [m^{-1}] \tag{2.8}$$

for the 1D and 2D cases, respectively.

2.3.2 Update of electromagnetic fields

Once the particles have been positioned in the grid and the charge and current densities computed, Maxwell's equations can be solved in

order to update the fields. These equations are given by:

$$\vec{\nabla} \times \vec{E} = -\partial_t \vec{B} \tag{2.9}$$
$$\vec{\nabla} \times \vec{B} = \partial_t \vec{E} + \vec{J} \tag{2.10}$$
$$\vec{\nabla} \cdot \vec{E} = \rho \tag{2.11}$$
$$\vec{\nabla} \cdot \vec{B} = 0 \tag{2.12}$$

To illustrate how to update the electromagnetic fields, let us consider for simplicity the one-dimensional case (spatial coordinate x), since the number of displayed equations will be smaller and the path followed to solve the problem will be similar for 2D and 3D. In this case Maxwell's equations transform into:

$$\partial_t B_x = 0 \tag{2.13}$$
$$\partial_t B_y = \partial_x E_z \tag{2.14}$$
$$\partial_t B_z = -\partial_x E_y \tag{2.15}$$
$$\partial_t E_x = -J_x \tag{2.16}$$
$$\partial_t E_y = -\partial_x B_z - J_y \tag{2.17}$$
$$\partial_t E_z = \partial_x B_y - J_z \tag{2.18}$$
$$\partial_x B_x = 0 \tag{2.19}$$
$$\partial_x E_x = \rho \tag{2.20}$$

In order to create a compact set of equations, we can define the field $F_{\pm}^{(i,j)} \equiv E_i \pm B_j$ and the operator $D_{\pm} \equiv \partial_t \pm \partial_x$, where the indexes $(i,j) \in \{0,1\} \equiv \{y,z\}$ account for the transverse field components. Equations (2.13-2.20) can be rewritten as:

$$D_{\pm} F^{(i,j)}_{\pm(-1)^i} = -J_i \tag{2.21}$$

This set of equations can be solved numerically. If we define the cell width as Δx and we assume that $\Delta x = \Delta t$ for simplicity (valid assumption for 1D simulations [1, 3]), we obtain that the numerical solution for the longitudinal components is:

$$E_x(x \pm \Delta x, t) = E_x(x,t) + \rho(x \pm \Delta x/2)\Delta x \quad (2.22)$$

$$E_x(x, t + \Delta t) = E_x(x,t) - J_x(x + \Delta_x/2, t + \Delta t/2)\Delta t \quad (2.23)$$

$$B_x(x \pm \Delta x, t) = B_x(x,t) \quad (2.24)$$

$$B_x(x, t + \Delta t) = B_x(x,t) \quad (2.25)$$

In the same way, the solutions for the transverse components are:

$$F_{\pm}^{(y,z)}(x \pm \Delta x, t + \Delta t) = F_{\pm}^{(y,z)}(x,t) - \\ -J_y(x \pm \Delta x/2, t + \Delta t/2)\Delta t \quad (2.26)$$

$$F_{\pm}^{(z,y)}(x \mp \Delta x, t + \Delta t) = F_{\pm}^{(z,y)}(x,t) - \\ -J_z(x \mp \Delta x/2, t + \Delta t/2)\Delta t \quad (2.27)$$

Once these equations have been solved, it is possible to obtain the transverse field components from the following equations:

$$E_y = \frac{F_+^{(y,z)} + F_-^{(y,z)}}{2} \quad (2.28)$$

$$E_z = \frac{F_+^{(z,y)} + F_-^{(z,y)}}{2} \quad (2.29)$$

$$B_y = \frac{F_+^{(z,y)} - F_-^{(z,y)}}{2} \quad (2.30)$$

$$B_z = \frac{F_+^{(y,z)} - F_-^{(y,z)}}{2} \quad (2.31)$$

By using equations (2.22-2.27), the spatial distribution of the electromagnetic fields and its temporal update can be calculated.

This is a simple one-dimensional example, in which it is valid to assume that $\Delta x = \Delta t$ and therefore obtain the evolution of the transverse field components using the defined $F_{\pm}^{(i,j)}$ functions. In a more general case, the cell dimensions and the temporal step have to obey the Courant condition [3], and equations (2.13-2.20) must be solved separately in a

certain way [186]. Nevertheless, in a general case, the process to update the fields will be similar to the one presented here, although without so straightforward calculations.

2.3.3 Interpolation of fields

Once the electromagnetic fields have been updated, it is necessary to calculate the value of the fields acting upon each macroparticle. But first it is necessary to dive a bit further on the spatial distribution function of the macroparticles.

2.3.3.1 Distribution function of the macroparticles

As introduced before, we have assumed that each macroparticle has associated an spatial distribution function, given by $g(\vec{r} - \vec{r}_i)$, where $\vec{r}_i \equiv \sum_{j=1}^{3} x_j \hat{x}_j$ is the position of the ith particle. This means that the macroparticles are not punctual, but have an specific width in each spatial dimension. The reason behind this choice is rather simple, since choosing a punctual particle, i.e. a delta function, would mean that if the particle would move from one cell to the other, the change in density over one timestep would be very abrupt, while if it would remain into the same cell but at a different position, there would be no change in the density, which would also be incorrect.

The shape of this function is hence a factor to take into account, as it has to be chosen in a way that no abrupt density changes occur if the particle moves from one cell to the next. Assuming that each particle is initially located at the center of each cell, the simplest choice would be to define the distribution function with a rectangular profile that covers the whole cell:

$$g(\vec{r} - \vec{r}_i) = \Pi_{j=1}^{3} \frac{1}{\Delta x_j} \tag{2.32}$$
$$if\ \forall j \in \{1,2,3\},\ |x_j - x_{j,i}| < \Delta x_j/2$$
$$g(\vec{r} - \vec{r}_i) = 0 \tag{2.33}$$
$$if\ \forall j \in \{1,2,3\},\ |x_j - x_{j,i}| \geq \Delta x_j/2$$

however this distribution still leads to sudden jumps on the density when part of the density distribution crosses a cell. Therefore a different solution can be chosen. Another simple shape could be the triangular one for each spatial dimension. In the 1D case (shown for simplicity) it would be:

$$g(x - x_i) = \frac{2}{\Delta x}\left(1 \mp \frac{2}{\Delta x}(x - x_i)\right) \tag{2.34}$$
$$if\ (x - x_i) \in [0,\ \pm \Delta x/2)$$
$$g(x - x_i) = 0 \tag{2.35}$$
$$if\ (x - x_i) \notin [0,\ \pm \Delta x/2)$$

where we have assumed that the triangle width matches the cell width. In both cases, g is normalized to 1, that is: $\int_{\mathbb{R}^3} g(\vec{r} - \vec{r}_i)\, d^3x = 1$. With this shape the problem regarding cell crossing is solved, as depicted in figure 2.2, where it is shown the density evolution in two neighbourhoring cells for a 1D example when the density profile function is rectangular or triangular.

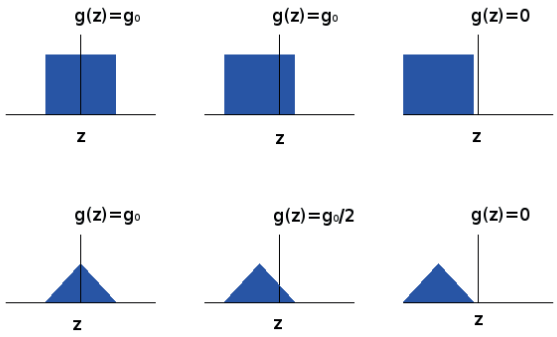

Figure 2.2: Example of the density measured at three different times for a specific point in space when a particle is departing from this point. The abrupt change for the rectangular shape does not happen for the triangular one, with a smoother transition.

In principle, any shape for the distribution function can be chosen, as long as it is integrable and it does not yield to numerical errors.

In figure 2.3 it is shown a very simple example of the effect of using a punctual function in the charge density on a regular grid. A 1D grid with 1000 particles initially positioned at the center of each cell is defined. Particles are moved randomly 10 times, with a maximum displacement of Δx. The resulting densities after this motion are shown for punctual and triangular distributions, along with the maximum and average deviation factors ζ, defined as the maximum and the average absolute difference between the density in the grid cells and the constant initial density. It is clear that by choosing the triangular distribution, the deviations are reduced for the same particle positions. The deviations for the expected uniform shape are big because of the low number of particles per cell chosen, only one, but it is clear that the density is smoothed.

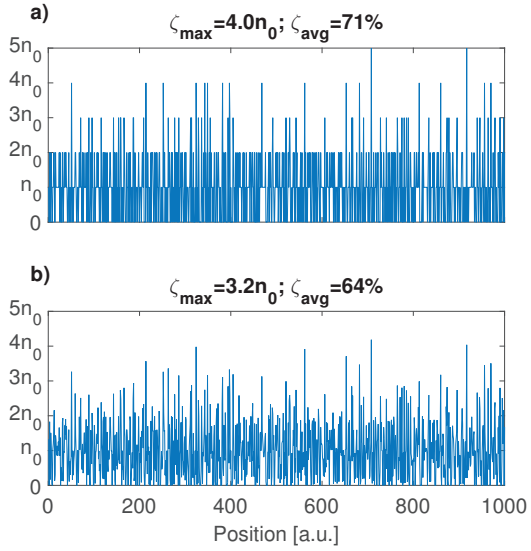

Figure 2.3: Density distributions after the random motion of particles for a) punctual and b) triangular macroparticle shape function. The deviation factors are shown.

2.3.3.2 Field interpolation

Once the extended distribution function for each macroparticle, as well as how to build it, have been explained, we are going to present how

to calculate the fields acting upon each particle.

The particle position is a real number, not restricted by the grid centers or borders, therefore its distribution function can fall within several cells at the same time. Fields and densities are defined in the grid, therefore to compute the fields acting upon each particle and update the charge and current densities, it is necessary to know "how much" of each particle belongs to each cell, or in other words, what is the volume (3D), the surface (2D) or the area (1D) of the distribution function that falls in the cells surrounding a particle. For this purpose we have to integrate the distribution function of each particle in each cell, since fields are defined at the grid borders, and the cells in this case are centered at the grid borders. Figure 2.4 illustrates this for a 2D example, in this case the total field on each particle would be:

$$E_{part} = \sum_{k=1}^{4} w_k E_k \tag{2.36}$$

where w_k is the integral of the distribution function in each cell centered at the grid borders and limited by the slashed lines. By definition $\sum_{k=1}^{4} w_k = 1$.

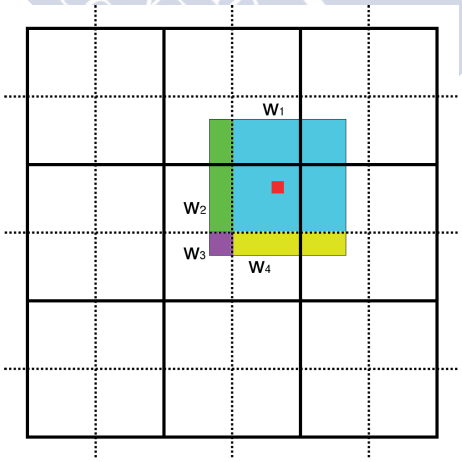

Figure 2.4: Example of how the interpolation mechanism would work in 2D. The particle position is represented by the red square and each weighting factor by w_k.

Via this method it is possible to calculate the electromagnetic fields acting upon each particle and therefore move into the last part of the loop, in which the particle motion is computed.

2.3.4 Update of the position and momentum

Once the fields acting upon each particle are computed, their position and velocity are updated through Lorentz's equation:

$$\frac{d\vec{p}}{dt} = \mathcal{Q}\left[\vec{E} + \frac{\vec{p}\times\vec{B}}{\mathcal{M}\gamma}\right] \tag{2.37}$$

where $\mathcal{Q} \equiv q/|q_e|$ and $\mathcal{M} \equiv m/|m_e|$ are the dimensionless charge and mass parameters. Once the momentum is calculated, the position of the particle is given by:

$$\frac{d\vec{r}}{dt} = \frac{\vec{p}}{\mathcal{M}\gamma} \tag{2.38}$$

Equation (2.37) can be solved via the Boris algorithm [187], taking into account that it represents a translation $(\vec{E})$ and a rotation $(\vec{p}\times\vec{B})$. This algorithm computes the effect of an electromagnetic field over a particle in a three-step process for updating the momentum and an additional step for the position. First the particle is moved linearly by the electric field in a time interval of $\Delta t/2$, after it's rotated by the magnetic field and finally is moved linearly again, figure 2.5 depicts this process.

2.3.4.1 First translation

To do this first movement, we will consider only the effect of the electric field with a timestep of $\Delta t/2$. We calculate the new momentum vector as:

$$\begin{aligned}\frac{d\vec{p}}{dt} = \mathcal{Q}\vec{E} \approx \frac{\vec{p}(t) - \vec{p}(t-\Delta t/2)}{\Delta t/2} \rightarrow \\ \rightarrow \vec{p}(t) \approx \vec{p}(t-\Delta t/2) + \mathcal{Q}\vec{E}\frac{\Delta t}{2}\end{aligned} \tag{2.39}$$

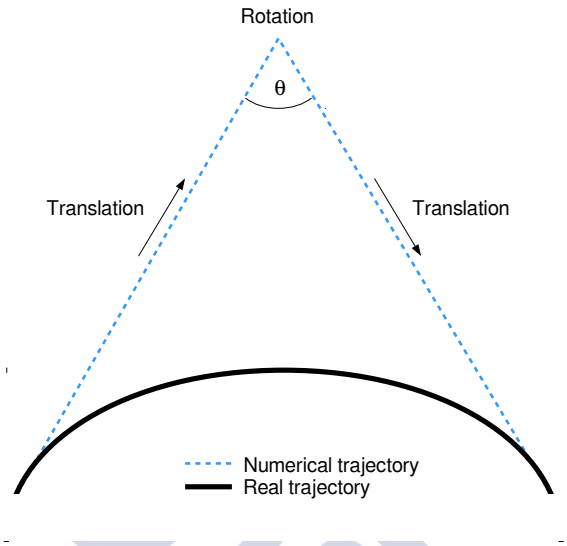

Figure 2.5: Boris algorithm depiction comparing numerical and analitical trayectories.

2.3.4.2 Rotation

Now that we have our transformed momentum, we need to account for the magnetic field. The magnetic field action is given by:

$$\frac{d\vec{p}}{dt} = \frac{\mathcal{Q}}{\mathcal{M}} \frac{\vec{p} \times \vec{B}}{\gamma} \tag{2.40}$$

with the relativistic factor given by $\gamma = \sqrt{1 + p^2}$.

Equation (2.40) expresses a rotation, since the equation reads as: "the variation of the momentum per time is given by the cross product of itself with the magnetic field", therefore the variation obtained is perpendicular to both and does not change in module, as proven by the equation:

$$\frac{d\vec{p}^2}{dt} = 2\vec{p}\frac{d\vec{p}}{dt} \propto \vec{p} \cdot (\vec{p} \times \vec{B}) = 0 \rightarrow p = constant \tag{2.41}$$

This means that the momentum vector will rotate around the axis

marked by the magnetic field because $\frac{d\vec{p}}{dt}$ and $\vec{p}$ form a plane perpendicular to $\vec{B}$.

Naming p^- and p^+ the momenta before and after the rotation, we can approximate equation (2.40) to estimate the value of the rotation angle, defined as the angle formed by the vectors before and after rotation, i.e. $\cos(\theta) = \frac{\vec{p}^- \cdot \vec{p}^+}{p^2}$.

$$\frac{d\vec{p}}{dt} \approx \frac{\vec{p}^+ - \vec{p}^-}{\Delta t};\ \ \vec{p} \approx \frac{\vec{p}^+ + \vec{p}^-}{2} \rightarrow \tag{2.42}$$

$$\rightarrow \frac{\vec{p}^+ - \vec{p}^-}{\Delta t} \approx \frac{\mathcal{Q}}{2\mathcal{M}\gamma}(\vec{p}^+ + \vec{p}^-) \times \vec{B} \rightarrow \tag{2.43}$$

$$\rightarrow \frac{|\vec{p}^+ - \vec{p}^-|}{|\vec{p}^+ + \vec{p}^-|} = \frac{\mathcal{Q}B}{2\gamma\mathcal{M}}\Delta t \tag{2.44}$$

Since we know that $(\vec{p}^+ \pm \vec{p}^-)^2 = 2p^2(1 \pm \cos(\theta))$ and $\cos(\theta) = \cos^2(\theta/2) - \sin^2(\theta/2)$, we obtain from equation (2.44) the rotation angle as:

$$\frac{|\vec{p}^+ - \vec{p}^-|}{|\vec{p}^+ + \vec{p}^-|} = \tan\left(\frac{\theta}{2}\right) = \frac{\mathcal{Q}B}{2\gamma\mathcal{M}}\Delta t \tag{2.45}$$

From the angle of rotation we can obtain the rotation matrix associated to it, knowing that, in general the rotation matrix around an arbitrary axis $\vec{t} = (t_x,\ t_y,\ t_z)$ is given by $\mathcal{R}$:

$$\mathcal{R} = \cos(\theta)\mathbb{I} + \sin(\theta)[\vec{t}]_\times + (1 - \cos(\theta))\vec{t} \otimes \vec{t} \tag{2.46}$$

where $\mathbb{I}$ is the identity matrix and the operator $[\vec{t}]_\times$ stands for $\vec{t}\otimes$.

To express $\mathcal{R}$ in more familiar terms we define the vector $\vec{t} \equiv \frac{\mathcal{Q}\Delta t}{2\gamma\mathcal{M}}\vec{B}$ such that $t = \tan\left(\frac{\theta}{2}\right)$ and from trigonometry we obtain:

$$\cos(\theta) = \cos^2(\theta/2)\left[1 - \tan^2(\theta/2)\right] = \frac{1 - t^2}{1 + t^2} \tag{2.47}$$

$$\sin(\theta) = 2\cos(\theta/2)\sin(\theta/2) = \frac{2t}{1 + t^2} \tag{2.48}$$

We are now ready to express equation (2.46) in matrix terms, taking into account the relations $1-\cos(\theta) = \frac{2t^2}{1+t^2}$, $t^2 = t_x^2 + t_y^2 + t_z^2$ and normalizing the rotation direction vector, i.e. $t_n \to t_n/t$. The matrix form of the rotation in equation (2.46) can be expressed as:

$$\mathcal{R} = \begin{bmatrix} 1 - \frac{2(t_y^2+t_z^2)}{1+t^2} & \frac{2(t_x t_y - t_z)}{1+t^2} & \frac{2(t_x t_z + t_y)}{1+t^2} \\ \frac{2(t_x t_y + t_z)}{1+t^2} & 1 - \frac{2(t_x^2+t_z^2)}{1+t^2} & \frac{2(t_y t_z - t_x)}{1+t^2} \\ \frac{2(t_x t_z - t_y)}{1+t^2} & \frac{2(t_y t_z + t_x)}{1+t^2} & 1 - \frac{2(t_x^2+t_y^2)}{1+t^2} \end{bmatrix} \tag{2.49}$$

Known this expression, the rotated momentum is obtained from:

$$\vec{p}^{+} = \mathcal{R}\vec{p}^{-} \tag{2.50}$$

2.3.4.3 Second translation

The procedure in this step is the same as in the first one, in this case we will go from $\vec{p}(t) = \vec{p}^{+}$ to $\vec{p}(t + \Delta t/2)$. The final momentum is expressed as follows:

$$\vec{p}(t + \Delta t/2) \approx \vec{p}(t) + \mathcal{Q}\vec{E}\frac{\Delta t}{2} \tag{2.51}$$

2.3.4.4 New position

Finally we can update the particles' positions, knowing that the velocity is defined as:

$$\frac{d\vec{r}}{dt} \equiv \vec{v} = \frac{\vec{p}}{\mathcal{M}\gamma} \tag{2.52}$$

Integrating numerically this equation, we obtain the new position, given by:

$$\vec{r}(t + \Delta t) \approx \vec{r}(t) + \frac{\vec{p}(t + \Delta t/2)}{\mathcal{M}\gamma(t + \Delta t/2)}\Delta t \tag{2.53}$$

To demonstrate the validity of this algorithm, figure 2.6 compares the analytical and numerical motion of an electron under the influence

of an elliptically polarized laser pulse, where it can be seen the quality of this method to reproduce the analytical curve. In this particular case, all numerical errors in the position are below $10^{-9}\lambda$.

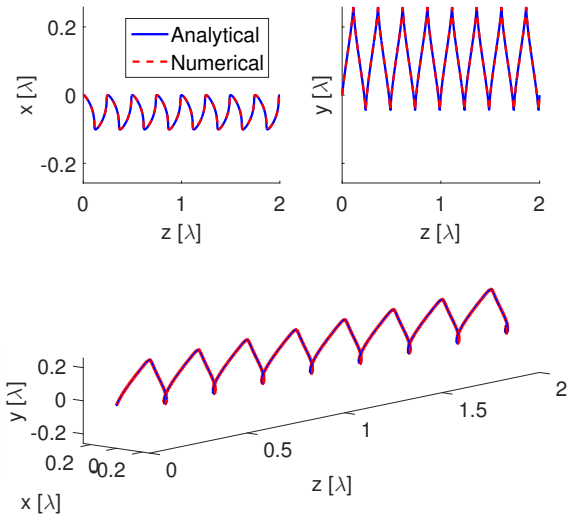

Figure 2.6: Comparison between analytical and numerical trajectories of an electron under the action of an elliptically polarized pulse of amplitude $a_0 = 1$ propagating along the z axis, with its principal polarization axes rotated $\pi/4$ in the $\overline{XY}$ plane and a ratio equal to 3 between the major and the minor axes of the ellipse.

Once the new positions and momenta for the particles are computed, the charge and current densities can be recalculated and the loop restarted.

2.4 PIC CODES AND HPC CLUSTERS

For the results obtained in this work, two PIC codes have been used: the first one is OSIRIS [188–190]. This code was developed by the "Instituto Superior Técnico" (IST) in Lisbon (Portugal) and the "University of California in Los Angeles" (UCLA) in Los Angeles (California, United States of America). The second one is named PICADOR [191, 192], developed by the Lobachevsky State University in Nizhny Novgorod (Nizhny Novgorod Oblast, Russian Federation), the Institute of Applied Physics of the Russian Academy of Sciences in Nizhny Novgorod

(Nizhny Novgorod Oblast, Russian Federation) and the Chalmers University of Technology in Gothenburg (Sweden). Both codes have proven to be sucessfull by several publications and have been used by several research groups throughout the world, unlocking many interesting results. In this thesis we have used mostly OSIRIS.

PIC codes demand very high computational resources, therefore they are usually built in a way that they can be executed using several processors at the same time, a process known as parallelization. The need to use several hundreds or thousands of processors to execute a simulation is quite common with these simulation codes, and therefore high performance computing (HPC) clusters are needed to execute them. In this thesis, three clusters have been used: The "Centro de Supercomputación de Galicia" (CESGA), located in Santiago de Compostela (Spain) and funded by the Galician regional government, the "Xunta de Galicia"; the cluster "Accelerates", located in Lisbon (Portugal) and funded by an Advanced Grant from the European Research Council (ERC); and the cluster "Mare Nostrum 4" of the Barcelona Supercomputing Center (BSC), located in Barcelona (Spain) and funded by the Spanish and Catalan governments and by the Polytechnic University of Catalonia (UPC).

USC
UNIVERSIDADE
DE SANTIAGO
DE COMPOSTELA

3 HIGH HARMONIC GENERATION IN OVERDENSE PLASMAS

As it was already detailed in the introduction, High Harmonic Generation (HHG) and its associated attosecond pulse production in the interaction between intense laser pulses and overdense plasmas is a nonlinear mechanism that produces a spectrum containing high harmonics of the fundamental laser frequency, that is carried in the reflected field. When a part of the high harmonic orders in the spectrum are filtered, the spatiotemporal shape of the reflected field shows the periodic emission of ultrashort bursts of radiation, with lengths typically in the order of the hundreds of attoseconds. In this section we will first depict some of the features of this HHG mechanism, and then we will show results related with techniques that we have designed to improve some of the features of this radiation mechanism.

3.1 FUNDAMENTAL CHARACTERISTICS OF HHG

The typical setup for obtaining high harmonics consists on a laser pulse impinging onto the surface of a solid density plasma. The laser electric field moves the electrons at the plasma surface while the pulse is being reflected, which has as a product the production of radiation in the form of high harmonic orders that accompany the reflected field.

Figure 3.1 displays the HHG spectrum; the reflected field; the corresponding attosecond pulse train once the highlighted part of the spectrum has been filtered; and the temporal evolution of the electron number density. In this case a linearly P-polarized pulse with an amplitude $a_0 = 10$ and an angle of incidence of $\theta = 45^\circ$ interacts with a plasma made of electrons and heavy ions with a steep density profile and a bulk density of $n = 100 n_c$. The superposition of the reflected laser field with the pulse train demonstrates that the emission of these pulses corresponds to the oscillations of the input laser field, as it is related to them.

Several factors affect the generation of the harmonic spectrum and its corresponding train of pulses, such as the laser peak intensity, the

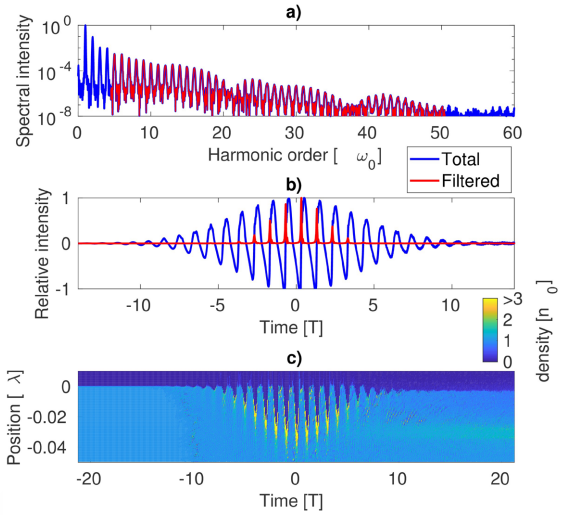

Figure 3.1: Example of a HHG spectrum for a gaussian laser pulse with FWHM of 25 fs and amplitude $a_0 = 10$ interacting with a steep plasma of density $n = 100n_c$ at an angle of incidence of $\theta = 45°$.

laser pulse shape, the angle of incidence, the plasma density and the shape of the plasma density at the target front, among others. The effect of these factors has been addressed in several publications [4, 5, 26, 27, 33–36, 43, 45–47], and their values are associated with the regimes of interaction described by the main theoretical models listed in the introduction section. For example, increasing the laser intensity or decreasing the plasma density triggers more intense oscillations of the surface electrons; using non-zero angles of incidence allows the use o P-polarization, that triggers more intense oscillations of the electrons at the surface, since the P-polarized component penetrates into the plasma; the existence of a pre-plasma region makes available lower density plasma regions that the laser can interact with, thus allowing the motion of more electrons to relativistic velocities. Apart from these factors, the use of P-polarized or S-polarized laser pulses changes the parity and polarization of the harmonics, as predicted by the selection rules of HHG [4, 27].

Other interesting factor to take into account is the pre-plasma, since

it can significantly modify the outcome of the laser-plasma interaction [43, 45] and it is very relevant from the experimental point of view, where a laser pulse with a perfect contrast is not possible to achieve, therefore, even for the highest contrast pulses, a short pre-plasma will exist at the arrival of the main laser pulse due to the expansion of the plasma into the vacuum. Unless specified differently, in this thesis all the simulations that include a pre-plasma region will assume the existence of a preplasma with exponential shape, which is supported by both theoretical and experimental studies [193–195], being described by the following equation:

$$n = n_0 \left(e^{\log(2)\frac{x-x_0+L}{L}} - 1 \right) \quad x \in [x_0 - L,\ x_0] \tag{3.1}$$

where n_0 is the bulk density, x the spatial coordinate and L the factor that parametrizes the length of the pre-plasma, defined as the scale-length of the pre-plasma.

Figure 3.2 shows examples of the harmonic spectrum generated by varying the laser pulse intensity, the angle of incidence, the plasma density and the scale-length of the pre-plasma, all of this considering linear P-polarized and S-polarized pulses. Some of the main features of HHG, already described in the literature, can be observed. All the cases shown in the figure take as a reference a setup with an amplitude $a_0 = 10$, a density $n = 100 n_c$, an angle of incidence $\theta = 45°$ and an scale-length $L = 0$. The difference between using P-polarized and S-polarized pulses is obvious, since in the latter the harmonic generation is less efficient and only odd harmonic orders are produced in the S-polarization axis, as predicted by the selection rules [27]. By increasing the intensity or decreasing the density of the plasma (while being overdense, that is $n \gg n_c$), it can be seen at first that the harmonic generation is more efficient at higher orders and that the spectrum extends well beyond the plasma density at $\omega_p = \sqrt{n/n_c}$. Increasing the scale-length enhances the harmonic generation substantially, as seen by the the relation between the fundamental and higher order harmonics, mainly due to the availability of low density regions for the pulse to interact with, but also generates a harmonic spectrum with a higher amount of noise, as seen by the spread of the harmonic peaks and the background signal. Using oblique

incidence enhances the harmonic generation in the P-polarized case, but does not affect substantially the S-polarized harmonics when using S-polarized pulses.

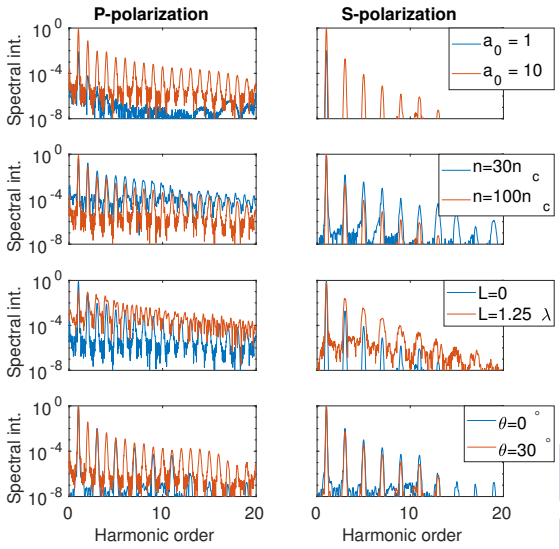

Figure 3.2: Examples of spectrums obtained in the P-polarization and S-polarization for P-polarized and S-polarized laser pulses, varying some of the parameters in the simulation, as indicated in the legends. The default parameters are $a_0 = 10$, $n = 100n_c$, $\theta = 45°$ and $L = 0$.

We have introduced and shown some of the main properties of HHG in the interaction between high intensity laser pulses and overdense plasmas. Examples and a more detailed analysis of what has been shown in the previous figures can be seen in the literature (see references [4, 5] and references therein), however with this quick introduction the reader can get a glimpse on the most fundamental properties of HHG without the need to read a substantial amount of literature.

3.2 BOOSTED FRAME TECHNIQUE

Since the cause of the emission of harmonic orders is the relativistic motion of the electrons at the plasma surface [27, 29, 39], it is very common to simulate this interaction with one-dimensional PIC simulations, in which only one spatial dimension and the three components of the ve-

locity are considered (as it has been done for the results shown in figures 3.1-3.2). In order to simulate oblique incidence in 1D, we use the boosted frame method [196], that consists on making a Lorentz transformation of the coordinate system with a velocity boost of $v = \sin(\theta)$, being θ the angle of incidence of the laser field, in the dimension where the laser is obliquely incident. In this new frame of reference the simulation transforms into a 1D simulation where the laser pulse impinges on the plasma in the normal direction. The validity of this method to compute the HHG spectrum has been verified in several papers [4, 27, 29].

The transformation of the relevant physical parameters by applying the Lorentz boost can be easily calculated from the Lorentz transformation laws, in this way the new quantities in the $(x',\ y',\ z')$ axis system, where the boost is $\vec{v} = -\sin(\theta)\hat{y}$, are written as:

$$n' = n/\cos(\theta) \tag{3.2}$$
$$\omega' = \omega\cos(\theta) \tag{3.3}$$
$$\tau' = \tau/\cos(\theta) \tag{3.4}$$
$$\Delta x' = \Delta x/\cos(\theta) \tag{3.5}$$
$$a_{0,x'} = 0 \tag{3.6}$$
$$a_{0,y'} = a_{0,p}\cos(\theta) \tag{3.7}$$
$$a_{0,z'} = a_{0,s}\cos(\theta) \tag{3.8}$$

where τ is the pulse width, Δx a distance in the longitudinal direction and $a_{0,i}$ refers to the dimensionless field amplitude for each of the new axes (indicated in the subindex).

In order to verify the validity of the use of 1D simulations and the boosted frame technique, we have ran comparisons between 1D and 2D PIC simulations, to observe if the reflected harmonic spectrum in both cases is the same. Figure 3.3 shows a perfect agreement between the harmonic spectrum for a P-polarized and a S-polarized pulse with amplitude $a_0 = 10$ and an angle of incidence of $\theta = 45°$, interacting with a plasma composed of electrons and heavy ions with a steep density profile and a density of $n = 100n_c$. The laser pulse used has a gaussian temporal profile in both cases, with a FWHM of 25 fs, and in the 2D

case its transverse profile is gaussian with a spot with a FWHM of 6λ, being λ the central wavelength of the laser. The spectrum in the 2D case is taken along the central axis for specular reflection.

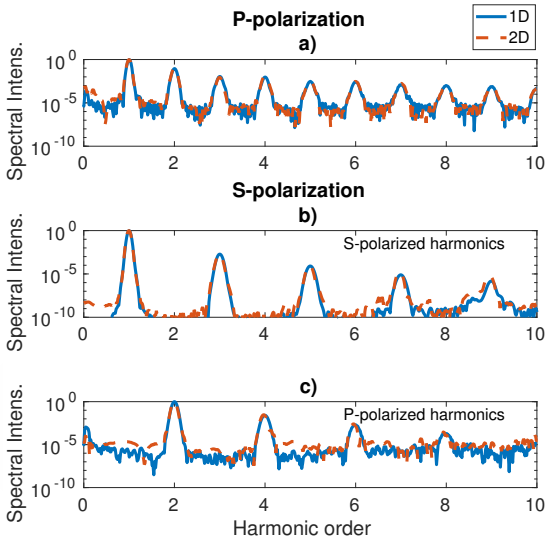

Figure 3.3: Harmonic spectrum for 1D and 2D PIC simulations for a a) P-polarized pulse and a b)-c) S-polarized pulse with the parameters $a_0 = 10$, $\theta = 45°$ and $n = 100n_c$.

3.3 MOTIVATION FOR THE MANIPULATION OF HHG

As described in the introduction and shown in the previous section, the HHG spectrum, when high order harmonics are filtered, appears in the spatial form of a train of attosecond pulses. These pulses can be used for several applications in atomic physics or plasma physics, however for many of these applications a high degree of tunability over the attosecond pulse train is needed.

Attosecond pulses produced in the interaction between a laser and a gas have been studied for a longer time than those in solids, since they can be obtained at much lower laser intensities than those studied here, hence the degree of tunability over these pulses when they are generated in gases is higher than the current one for HHG in laser-plasma interaction. Most of the applications of attosecond pulses have been

already implemented with high harmonics produced in gases, however the use of attosecond pulses from laser-plasma interaction can represent an advantage, since higher intensities and energies can be achieved. In order to do so it is needed to have a high degree of tunability over the attosecond pulse train.

In the following sections we will introduce methods to manipulate the properties of the attosecond pulse train, namely to achieve the isolation of a single or few attosecond pulses or to manipulate the polarization state of the attosecond pulses.

3.4 ISOLATION OF SINGLE ATTOSECOND PULSES

Some of the applications of attosecond pulses require the use of single isolated pulses, such as the probing of fundamental electronic dynamics in solid state physics [197], where attosecond pulses are used to explore electron dynamics via spectroscopy; the observation of fundamental electronic processes in atomic physics, such as the ionization of an atom under an intense electric field [198], where an attosecond pulse can be used to probe the tunneling process followed by the electron; or metrology under XUV pump-probe technologies [62], where XUV attosecond pulses are used both as pumping and probing tool.

The isolation of single attosecond pulses is a widely studied topic for HHG generated both in gases and overdense plasmas, where several techniques have been developed to achieve this isolation [46, 47, 53, 56–58, 199–204]. Up to date, for attosecond pulses produced in laser-plasma interaction, there are just a few methods to achieve this isolation, namely the Intensity Gating method [53], the Polarization Gating method [46, 47, 199, 200], the Attosecond Lighthouse method [56–58], and, most recently, the Frequency Gating method [201].

The Intensity Gating method [53] is the simplest and most natural method for isolating single attosecond pulses. It relies on the fact that the most intense harmonic generation corresponds to the most intense electric field oscillations, therefore by filtering higher orders of the harmonic spectrum the attosecond pulse train will be shortened, and if the laser pulse used is short enough, it could be possible the isolation of a single attosecond pulse. This mechanism is somehow always present

when a certain region of the HH spectrum is filtered.

The Polarization Gating method [46, 47, 199, 200] makes use of the dependence of HHG on the polarization state of the laser pulse, being optimal for linearly P-polarized pulses at oblique incidence and suppressed for circularly polarized pulses at normal incidence. Taking into account this dependence, one can use a laser pulse with a time-dependent polarization, such that the most intense central region of the pulse is linearly polarized and the rest is circularly polarized. If the linear polarization window is short enough, the attosecond pulse train will be restricted to this temporal window. This behaviour occurs as well in gas generated attosecond pulses, where the suppression for circularly polarized pulses occurs always and this method can be also implemented.

The Attosecond Lighthouse method [56–58] is a recently proposed method, that uses a modulation of the spatial distribution of the laser pulse to tilt the local direction of its wavefront, that is changing locally the direction of the wave vector $\vec{k}$, such that the generated attosecond pulses are emitted with different reflection angles. Under large enough propagation distances, the generated pulses can be regarded as isolated.

The latest and most recent of the methods to isolate attosecond pulses for HHG in laser-plasma interaction is the Frequency Gating method [201], that consists on the combination of two laser pulses of equal amplitude and envelope shape, with a short frequency shift between them, such that a beating pattern is formed in the resulting field, shortening in effective terms the pulse width and therefore reducing the amount of attosecond pulses in the train.

In the following text we will introduce a new proposal to implement a polarization gate for HHG in laser-plasma interaction, plus we will introduce the concept of Frequency Gating and explain its main features. These results for Polarization Gating and Frequency Gating have been published in references [200, 201], respectively.

3.4.1 Polarization Gating

As explained above, the polarization gating technique relies on the fact that the efficiency of HHG depends on the polarization of the laser pulse, being most optimal for linear P-polarized pulses at oblique

incidence and completely suppressed for circularly polarized laser pulses at normal incidence. Figure 3.4 shows the harmonic spectrum of the P-polarized reflected component for a linear P-polarized pulse and a circular pulse at two different angles of incidence ($\theta = \{0°,\ 15°\}$). The setup consists on a laser pulse of amplitude $a_0 = 10$ and a steep plasma profile of density $n = 100n_c$. It can be seen in figure 3.4 b) that the reflected field for the circular pulse at normal incidence only contains the fundamental frequency, and that at oblique incidence both spectra contain a higher number of harmonic orders. This increase on the harmonic orders is more prominent for the linear pulse than for the circular one.

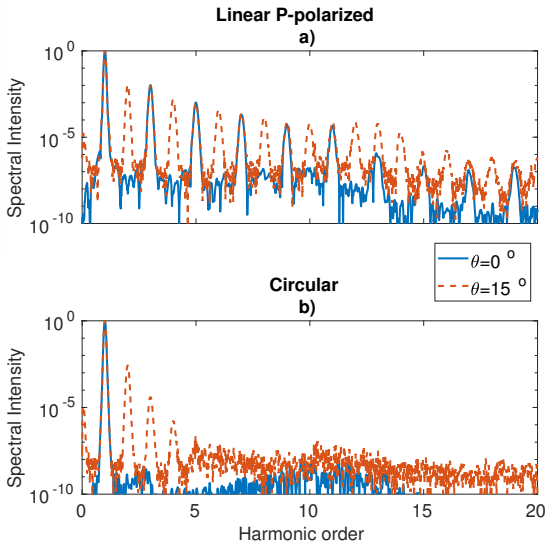

Figure 3.4: Harmonic spectrum of the P-polarized component for a) a P-polarized and b) a circularly polarized laser pulse, at the angles of incidence $\theta = \{0°,\ 15°\}$. Parameters are $a_0 = 10$ and $n = 100n_c$.

The suppression of the harmonic generation for circular pulses at normal incidence can be explained theoretically by analyzing the relativistic motion of a free electron under the influence of an electromagnetic field.

In a general case, the vector potential of a plane wave propagating in vacuum is given by:

$$\vec{A} = \frac{a_0}{\sqrt{a^2+b^2}}\left(a\cos(\phi)\hat{x} + b\cos(\phi+\delta)\hat{y}\right) \tag{3.9}$$

where ϕ is the oscillatory phase, δ a phase difference between the polarization components and a and b two constants to account for the balance in amplitude for the two components.

The Lorentz equation for an electron under the influence of this field is given by:

$$\vec{F} = \frac{d\vec{p}}{dt} = -\vec{E} - (\vec{v}\times\vec{B}) = \frac{\partial\vec{A}}{\partial t} - \left(\frac{\vec{p}}{\gamma}\times(\vec{\nabla}\times\vec{A})\right) \tag{3.10}$$

where we have used the relation between the electromagnetic fields and the vector potential.

This equation can be solved, obtaining that the momentum components of this electron are given by:

$$\vec{p}_\perp = \vec{A} \tag{3.11}$$

$$\vec{p}_\parallel = \frac{|\vec{A}|^2}{2} \tag{3.12}$$

where the indexes $\perp$ and $\parallel$ refer to the perpendicular and parallel directions relative to the propagation direction, in this particular example $\hat{z}$.

This motion can be extended into a simple nonlinear fluid model for HHG (see section IIIa in reference [4] for more details). In it the generated harmonic orders are explained by the nonlinear charge current densities generated in the plasma that contain oscillatory components that account for the harmonic spectrum. This can be easily seen from the wave equation for the vector potential:

$$\vec{\nabla}^2\vec{A} - \frac{\partial^2\vec{A}}{\partial t^2} = \frac{n\vec{p}}{\gamma} \tag{3.13}$$

where γ is the relativistic factor of the electrons, given by $\gamma = \sqrt{1+\vec{p}^2}$. Here we have assumed that the ion velocity in our time scale in negligible

and therefore the current density is given by the electron contribution: $\vec{J} = -n\vec{v} = -n\vec{p}/\gamma$.

In the case of normal incidence, the only term responsible for the longitudinal oscillations of the electrons is the $(\vec{v} \times \vec{B})$ term of the Lorentz equation, that leads to the longitudinal momentum component in equation (3.12). When the polarization of the electric field is circular ($a = b$ and $\delta = \pi/2$), the quantity $|\vec{A}|^2$ becomes constant ($|\vec{A}|^2 = a_0^2/2$) and longitudinal oscillations disappear. In this case and for normal incidence, the electrons get pushed in the longitudinal direction, but do not oscillate, thus they do not trigger any phase-dependent oscillations in γ that influence the current and yield to a harmonic spectrum.

Taking into account the dependence of HHG with the ellipticity of the laser pulse, the idea behind the Polarization Gating technique is to use a pulse with a time-dependent polarization, consisting on a circularly polarized pulse whose central and most intense region is linearly polarized, such that HHG is favored in a short temporal window.

In order to address how much the efficiency of the HHG process is affected by the ellipticity (ε) of the laser pulse, figure 3.5 shows the harmonic yield, that is the integral of the harmonic spectrum between two harmonic orders ($Y = \int_{\omega_1}^{\omega_2} d\omega |E_\omega|^2$), for several cases varying the angle of incidence and the selected harmonic interval. The parameters are a laser pulse of amplitude $a_0 = 10$ and a steep density profile with density $n = 100 n_c$. The ellipticity of the pulse in this case is defined considering that the major axis of the ellipse is the P-polarized component, thus the polarization vector of the field is given by $\vec{E} = \frac{a_0}{\sqrt{1+\varepsilon^2}} (\varepsilon \cos(\phi)\hat{s} + \sin(\phi)\hat{p})$. It can be observed that the generation is optimal for linear polarization, and it decreases as the ellipticity increases. The decrease of the harmonic yield, and therefore the efficiency of the gating method, is faster as the incidence angle approaches $\theta = 0°$, however the absolute efficiency is reduced substantially at normal incidence, but this case does not present interest from the experimental point of view, where oblique incidence is needed to avoid damage by the expelled particles from the solid target or the reflected radiation.

In this section we propose a new method for Polarization Gating, consisting on the use of a nonlinear optical effect known as Cross Po-

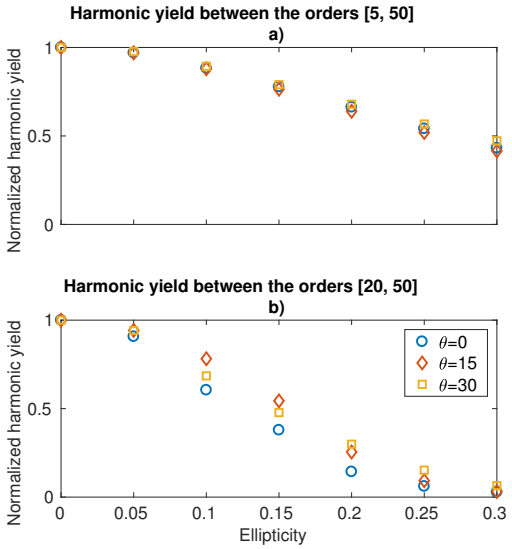

Figure 3.5: Harmonic yield dependence on the ellipticity for the harmonic orders in the intervals a) $[5,\ 50]$ and b) $[20,\ 50]$ for different angles of incidence $\theta = \{0°,\ 15°,\ 30°\}$. The amplitude of the electric field and the plasma density are $a_0 = 10$ and $n = 100n_c$, respectively.

larized Wave Generation (XPWG) [205] to generate a polarization gate. The results shown below have been published in reference [200].

XPWG is a nonlinear mechanism that occurs in a set of specific kind of crystals, such as BaF_2 crystals, by which a linearly polarized laser pulse passing through the crystal, with an amplitude above a certain threshold value, converts part of its energy into a perpendicularly polarized component. At the output a laser pulse with a time-dependent polarization is obtained by combination of the fundamental wave (FW) and the cross polarized wave (XPW), both waves being phase-matched. This pulse is linearly polarized but its polarization axis is rotated with time, since the efficiency of the XPWG depends on the local field amplitude.

The XPWG in BaF_2 crystals can be calculated numerically. In our case it is obtained via a numerical code, making use of a simplified model for XPW in the low-efficiency limit [206, 207]. This code simulates the propagation of the laser pulse across the crystal with the nonlinear

Schrödinger equation (NLSE) using a split-step Fourier method. Figure 3.6 shows an example of the intensity profiles for the FW and XPW output fields when a 25 fs FWHM gaussian laser pulse is focused in the XPW crystal. It can be seen that the XPWG is more efficient as the intensity of the FW grows, thus generating a narrower pulse for the XPW.

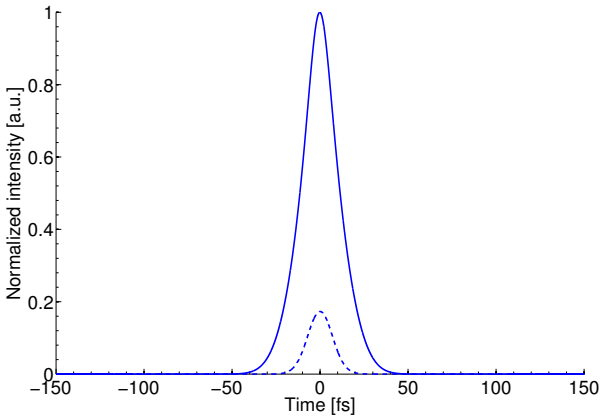

Figure 3.6: Intensity profile of the FW (solid line) and XPW (dashed line).

If the pulse consisting in the combination of the two waves goes across a $\lambda/4$ wave plate, such that the polarization of the central part of the pulse coincides with the wave plate axis, the output would be a pulse linearly polarized in the center and elliptically polarized in its borders. The setup proposed for generating this time-dependent polarized pulse is shown in figure 3.7.

The addition of the wave plate transforms the polarization state of the pulse, from a linear one at the pulse center to an elliptical one outside of the center. The maximum ellipticity that can be obtained can be calculated from the ratio between the peaks of the FW and XPW, as this will determine the inclination of the polarization axis with respect to the wave plate axis outside of the central region. The maximum ellipticity is given by $\varepsilon_{max} = \sqrt{I_{XPW}/I_{FW}}$. Figure 3.8 shows, for the intensity profiles in figure 3.6, a 3D view of the fields before and after passing through the wave plate.

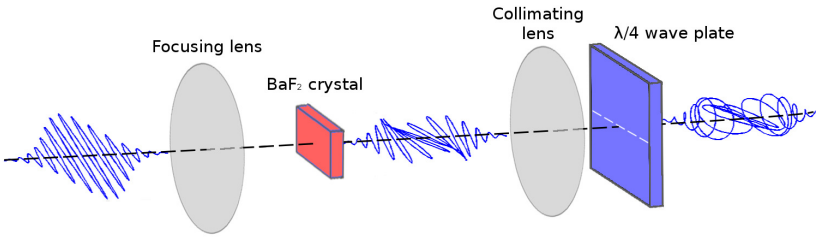

Figure 3.7: Depiction of the setup proposed to obtain a time-dependent ellipticity in the pulse.

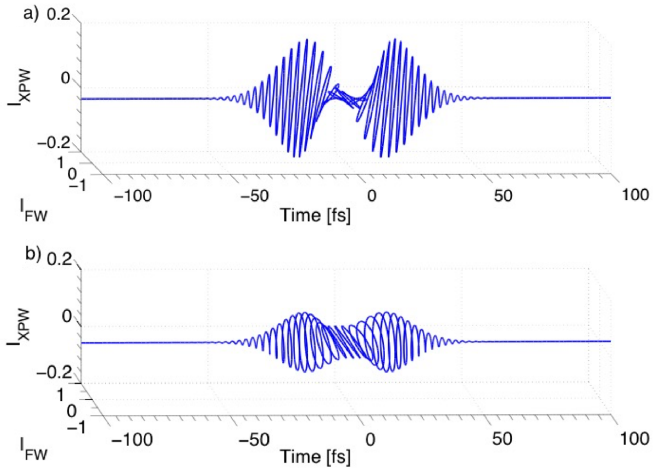

Figure 3.8: Three-dimensional view of the laser pulse obtained from the combination of the FW and XPW a) before and b) after passing through the $\lambda/4$ wave plate.

Figure 3.8 displays the time-dependent polarization pulse obtained with the setup shown in figure 3.7. For analyzing the emission of the train of attosecond pulses and to address the feasibility of this method, PIC simulations are used, where the laser pulse obtained from the proposed setup is used as an input pulse.

PIC simulations are performed in 1D with the boosted frame configuration, considering initially a P-polarized gaussian pulse with a FWHM of 25 fs and a central wavelength of $\lambda = 800$ nm. The intensity of the pulse is 2.05×10^{19} W/cm^2 ($a_0 = 3.08$) and the angle of incidence is $15°$.

The lase pulse interacts with an overdense plasma composed of electrons and heavy ions with a number density of $n = 70n_c$. A preplasma region with a scale-length of 0.3λ is considered. The number of particles per cell in the simulated plasma is 400. The simulation advances in time steps of $0.005/\omega$ with a spatial resolution of $0.01c/\omega$, that is 628 points per wavelength. The associated attosecond pulses are calculated performing the inverse Fourier transform to a filtered region of the reflected harmonic spectrum, between the harmonic orders $\omega \in [30,\ 50]$.

The parameters chosen for the laser pulse are determined by the damage limit for the BaF_2 crystal, taking care of avoiding undesired higher-order nonlinear effects. This lowering of the pulse intensity in comparison with the amplitude used in the previous figures makes HHG less efficient, therefore makes it necessary to use a plasma with a non-zero scale-length in order to trigger a more efficient generation of high harmonic orders.

Figure 3.9 shows the pulse train and the harmonic spectrum obtained for the initial linearly polarized pulse, where it can be observed that, by filtering harmonic orders of such a high order (> 30), a short train of pulses is already obtained.

If the field obtained from the proposed setup with the XPW crystal plus the $\lambda/4$ wave plate is used instead of the linear P-polarized pulse, then the reflected field; the train of attosecond pulses; the input ellipticity curve and the harmonic spectrum, shown in figure 3.10, are changed in comparison with the ones in figure 3.9. However, with the parameters chosen for the simulation, it can be seen that the ellipticity curve generated by the proposed setup is not enough for the shortening of the pulse train, since not so high values of ellipticity are obtained and their change is not fast enough, such that the most intense part of the input laser pulse is almost linearly polarized.

To improve the previous result, a modification to the original setup is proposed, as shown in figure 3.11. In this setup the two polarization components obtained from the crystal are separated, such that the FW goes through a dispersive material that adds a second order phase, named as Group Delay Dispersion (GDD), that increases the width of the FW, thus reducing its peak intensity and increasing the ratio between the FW

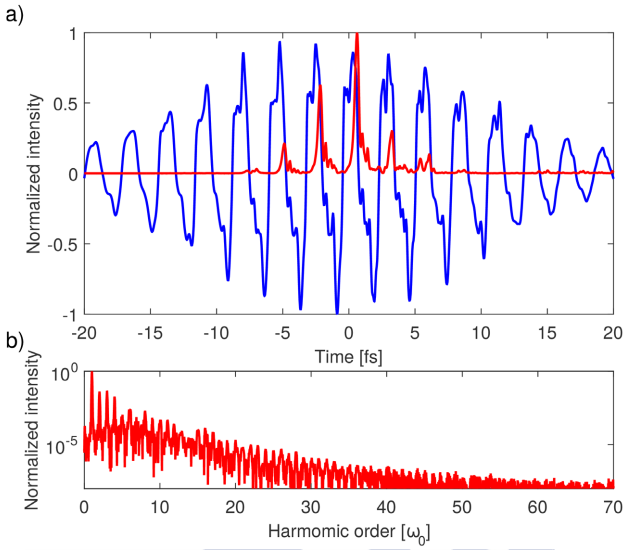

Figure 3.9: Reflected field (blue) and filtered attosecond pulse train (red). The bottom panel shows the reflected harmonic spectrum.

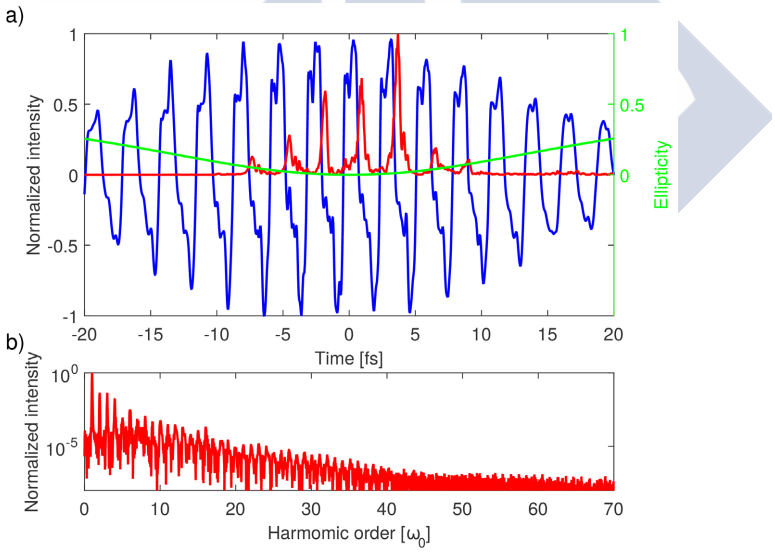

Figure 3.10: Reflected field (blue), input ellipticity curve (green) and filtered attosecond pulse train (red). The bottom panel shows the reflected harmonic spectrum.

and XPW, therefore yielding to a higher ellipticity outside of the central region of the laser pulse. This has as a subproduct a decrease on the peak intensity of the laser pulse, thus reducing the efficiency of the HHG process, but creates a more efficient ellipticity curve.

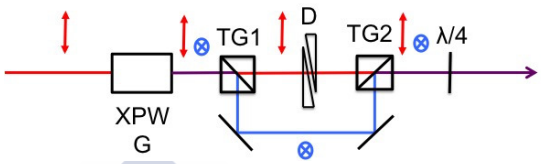

Figure 3.11: Modification of the original setup of figure 3.7: D is a dispersive material; TG1 and TG2 are two Taylor–GLAN polarizers orthogonally placed to separate and merge FW and XPW waves. The red arrow and the blue circle represent the polarization of the FW and the XPW waves, respectively. The purple color indicates collinear propagation of the FW and XPW.

The ellipticity curves for different cases of GDD are shown in figure 3.12. It can be observed that as the GDD increases the polarization window gets narrower and the maximum ellipticity increases. In principle a laser pulse with an ellipticity curve like the ones for a GDD of 800 fs^2 and 1000 fs^2 should be able to produce a polarization window better than the one shown in figure 3.10.

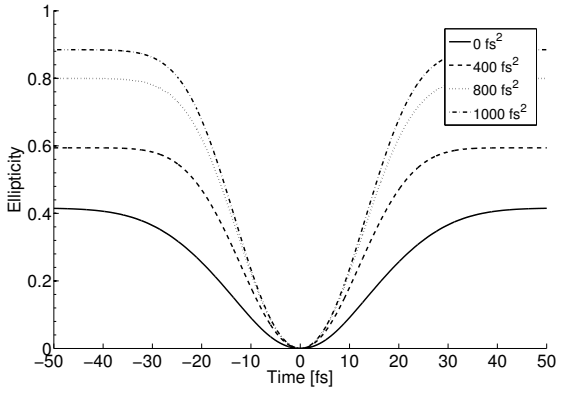

Figure 3.12: Variation of the ellipticity along the pulse duration. Simulations have been done for different GDD values: 0 fs^2 (solid line), 400 fs^2 (dashed line), 800 fs^2 (dotted line), and 1000 fs^2 (dot-dashed line).

The FW and XPW intensity profiles obtained with the new setup

for a GDD of 1000 fs^2 are shown in figure 3.13 a). In this case, the ratio between the peaks of the intensity profiles is near the unity, a substantial improvement in comparison with the curves in figure 3.6. The time-dependent polarized pulse after the wave plate is depicted in figure 3.13 b). The ellipticity in the outer regions of the pulse is much bigger than the presented in figure 3.8.

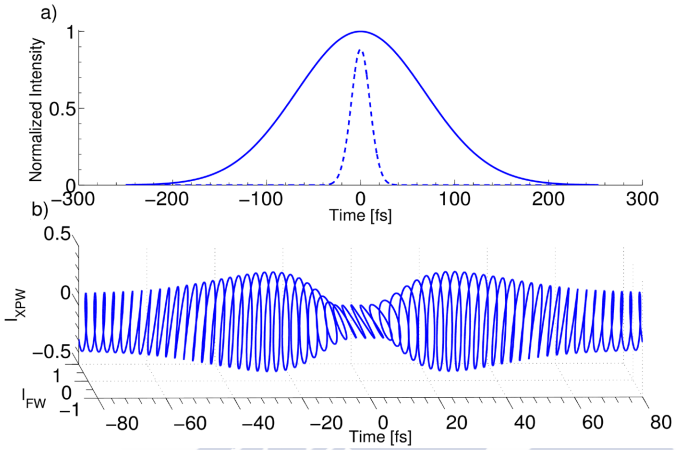

Figure 3.13: a) Normalized intensity profiles at the exit of the BaF_2 crystal for the FW pulse (solid line) and the XPW pulse (dashed line). b) Optical pulse after the $\lambda/4$ wave plate. The dispersive material adds a GDD of 1000 fs^2 to the FW.

For the case with a GDD of 1000 fs^2, the reflected field and the resulting attosecond pulse train are shown in figure 3.14. In this case, we can observe that it is possible to achieve the isolation of a single attosecond pulse when the harmonic orders in the interval $[30,\ 50]$ are filtered. It can be also observed that the reflected field, in comparison with the reflected field in figures 3.9 and 3.10, is only strongly modulated in the central part of the pulse, meaning that HHG is more restricted in this case to the central part of the pulse, and suppressed out of it due to the ellipticity curve. This effect can be seen also in the reflected spectrum, where the harmonic generation is much less efficient in this case, partly due to the decreased FW peak intensity and partly due to the narrowing of the linearly polarized region of the pulse.

It can be observed that, along with the isolated attosecond pulse,

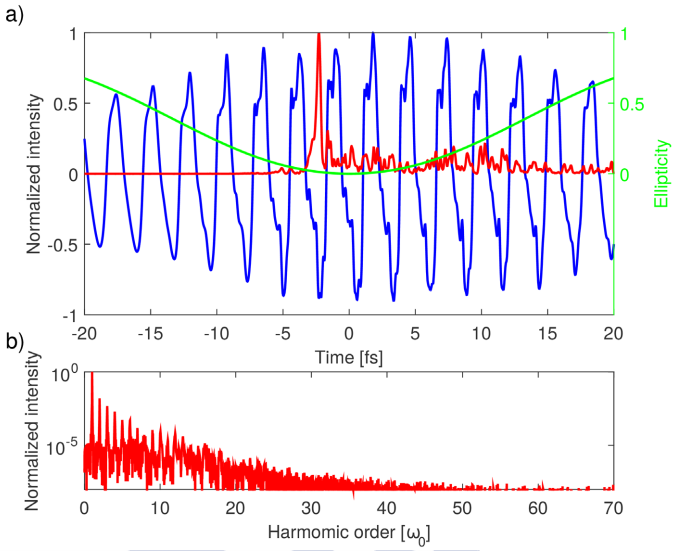

Figure 3.14: Reflected field (blue), input ellipticity curve (green) and filtered attosecond pulse train (red). The bottom panel shows the reflected harmonic spectrum.

there is a significant amount of noise because of the non-coherent emitted radiation, which is not negligible in relation to the HH spectrum due to the decreased efficiency of the HHG. To demonstrate that the isolated attosecond pulse shown in figure 3.14 is nor a numerical artifact nor a non-coherent burst of radiation, figure 3.15 shows the attosecond pulse train obtained for different cases in which the lower limit of the filtered harmonic region is changed. It can be observed that our attosecond pulse relates to one of the pulses in the original train of pulses obtained by filtering lower orders. It is clear that the background noise increases as the lower limit of the filtering interval increases, that is because the peak intensity in the filtered train decreases substantially in absolute terms, as the attosecond pulse peak intensity in panel c) is a 14% of the one in panel a).

In conclusion, the Polarization Gating technique takes advantage of the HHG dependence on the ellipiticity of the laser pulse to reduce the number of attosecond pulses in the train, or even to isolate a single one. We have proposed a new way to produce polarization gates for HHG in

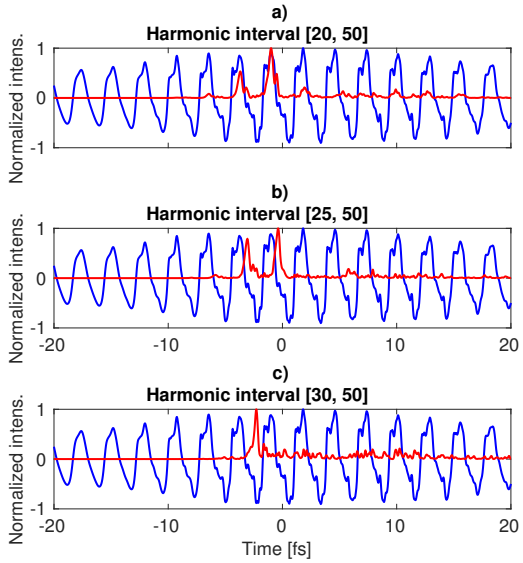

Figure 3.15: Attosecond pulse trains for the case with a GDD of 1000 fs^2 obtained by changing the lower limit of the filtering region to the harmonic order a) 20, b) 25 and c) 30.

solids using multi-cycle laser pulses. With this method we are able to generate laser pulses with a time-dependent polarization using a XPW crystal and a $\lambda/4$ wave plate. By adding a second order dispersion to the FW pulse we obtain an increase on the ratio between the FW and XPW pulses, thus producing a more optimal polarization gate. PIC simulations reveal that the polarization gate can reduce the number of pulses in the attosecond train up to the isolation of a single one in the most optimal case.

The main advantages of this approach are the simplicity of the setup and its feasibility to be used with multicycle laser pulses with lower intensities than those reported in the literature using multicycle lasers. The setup relies on the use of non-expensive optical elements arranged in a simple manner. The use of shorter laser pulses and higher peak intensities with a steep density profile should produce “cleaner” results in terms of background noise, however we chose these values in order to be realistic on what can be achieved with a table-top laser source and

non-expensive elements.

3.4.2 Frequency gating

To our knowledge, this is the most recent method in the literature for the isolation of single attosecond pulses, and its proposal is an original result from this thesis [201]. The main idea behind this method consists on the coherent combination of two laser pulses with equal amplitude and a non-integer ratio between their central frequencies, such that a beating pattern is formed in the resulting field. The coherent sum of the two pulses generates a slow oscillating component that, combined with the pulse envelope, forms a beating pattern and restricts the most intense region of the new pulse to a narrower window than this at the original pulse, being able to reduce the number of pulses in the train, even isolating one single pulse. Setups involving the coherent combination of more than one pulse and forming a beating pattern have been already studied extensively as a mean to isolate single attosecond pulses in HHG using gas targets [208–212], where it is possible to achieve isolated attosecond pulses very efficiently, even for multicycle laser pulses. In the case of laser-plasma interaction using solid targets, the effect of the combination of multiple laser pulses has been also studied, but to our knowledge never with this purpose and approach [45, 51, 52, 213, 214].

Let us consider two short pulses with frequencies ω_1 and ω_2, respectively, given by $E_j = \Gamma(t)\cos(\omega_j t)$, where $\Gamma(t)$ is the envelope function. The coherent sum of these two waves can be written as:

$$E = E_1 + E_2 = 2\Gamma(t)\cos\left(\frac{\omega_2+\omega_1}{2}t\right)\cos\left(\frac{\omega_2-\omega_1}{2}t\right) \qquad (3.14)$$

This means that there is a fast and slow oscillating wave. The frequency of the slow oscillating wave $(\omega_2 - \omega_1)$ can be tuned, in combination with the pulse envelope $\Gamma(t)$, by varying the frequency values, to create a beating pattern that yields to a narrower intense region. Figure 3.16 depicts, for a gaussian envelope function given by $\Gamma(t) = e^{-4log(2)(t/\tau)^2}$, several cases with different frequency shifts. We have used as principal wavelength of $\lambda_1 = 800$ nm $(\omega_1 = 2\pi\frac{c}{\lambda_1})$ and a FWHM of $\tau = 20$ fs.

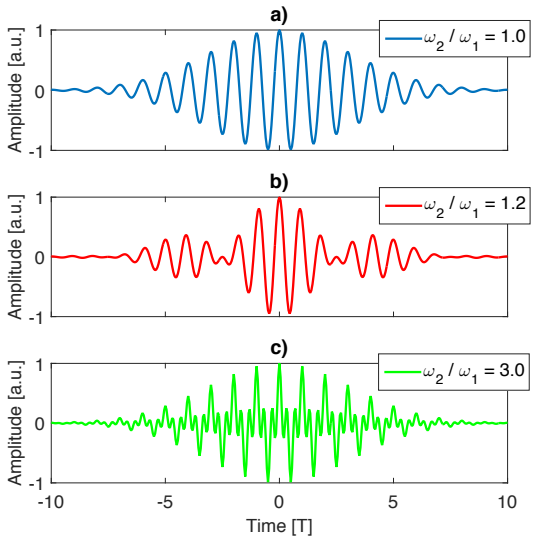

Figure 3.16: Laser pulses obtained through the combination of two frequency shifted pulses of a) equal frequency, b) a ratio of $\omega_2/\omega_1 = 1.2$ and c) a ratio $\omega_2/\omega_1 = 3$. The reference wavelength is $\lambda_1 = 800$ nm and the FWHM is $\tau = 20$ fs. The x axis is in units of the laser period, T.

It can be seen in figure 3.16 b) how the central and most intense part of the pulse becomes narrower when the frequency shift between the two pulses is tuned properly. Therefore HHG will be favoured for this smaller window of time. If the frequency shift is higher, such as in figure 3.16 c), fast oscillating corrections will be added to the original shape of the pulse, but the envelope of the most intense peaks will remain unchanged, disappearing the small temporal window from figure 3.16 b).

A more detailed analysis of the pattern formed by the combination of the two waves is shown in figure 3.17. Where it is seen both the electric field and the slow oscillating envelope wave. The 2D maps demonstrate in a more general way what is pointed out in figure 3.16, showing that as the frequency ratio increases, the central part of the pulse gets narrower, but up to a certain limiting frequency ratio, where more oscillations start to appear in the slow oscillating envelope. The limiting frequency ratio depends on the pulse width, as it grows for shorter pulses.

To check for the validity of this mechanism, we perform Particle-

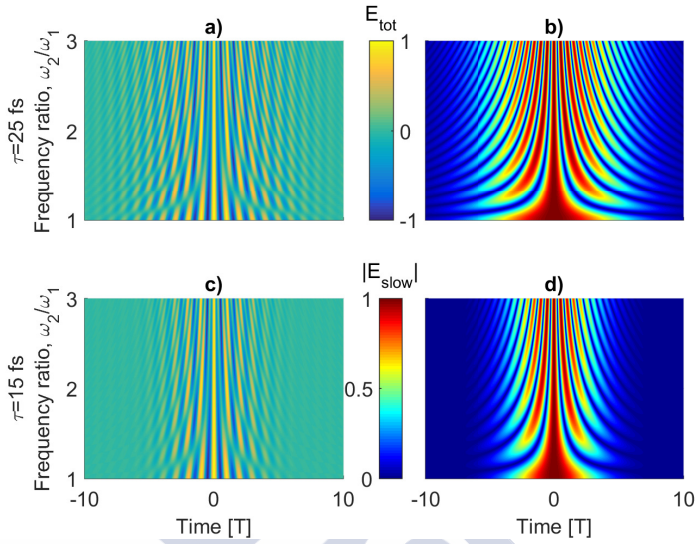

Figure 3.17: a)-c) Electric field obtained through the combination of two frequency shifted pulses and b)-d) slow oscillating envelope of that field. The color maps are shown for two FWHM of $\tau = \{15,\ 25\}$ fs. The reference wavelength is $\lambda_1 = 800$ nm. The x axis is in units of the laser period, T.

In-Cell (PIC) simulations. The simulations are done in 1D using P-polarized pulses with the boosted frame method. The target is composed of electrons and heavy ions with a number density of $100n_c$. We assume a steep density profile. The number of particles per cell is 200. The temporal and spatial resolution of the simulation box are $0.0025/\omega$ and $0.005c/\omega$, respectively, where ω is the frequency of the laser pulse, with a wavelength of $\lambda = 800$ nm. The laser pulses are initialized inside the simulation box with a gaussian profile, a dimensionless amplitude of $a_0 = 4$ and an angle of incidence of $45°$. The simulation runs until the whole pulse is reflected, that is the time that it would take it to return to its original position if the target would be a perfect mirror. The train of attosecond pulses is obtained by performing the inverse Fourier transform to the harmonic orders between the 5^{th} and the 50^{th} in the reflected field.

In order to study this mechanism and achieve an optimal configuration to produce the isolation of one single pulse or a few ultrashort

attosecond pulses, we have evaluated different ratios between the central frequency of both laser pulses. Figure 3.18 displays the result obtained by properly tuning the frequency shift to a ratio of $\omega_2/\omega_1 = 1.3$. In this case, in which a laser pulse with a FWHM of $\tau = 25$ fs has been used, it leads to almost the isolation of a single attosecond pulse in the filtered train of pulses. It can be seen clearly in the oscillations of the electron density that the most intense oscillations, associated to the generation of the most intense pulses with a higher frequency content, are confined into a shorter temporal window.

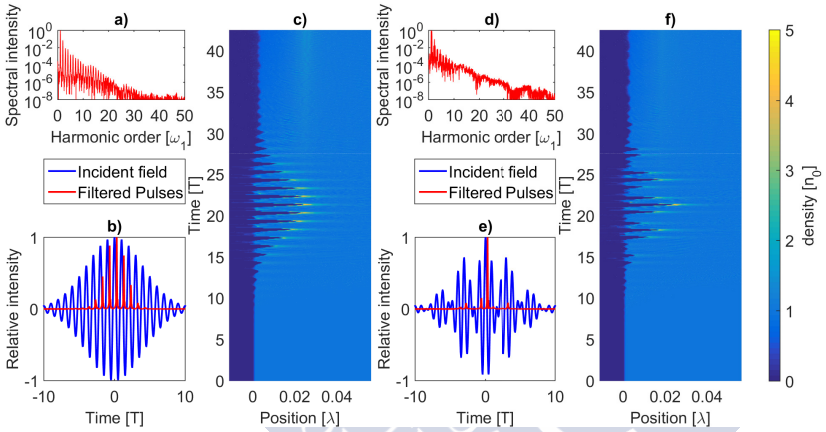

Figure 3.18: Comparison of two simulations to depict the isolation of a single attosecond pulse in the filtered pulse train. Both simulations are performed with two pulses of a)-c) equal frequency and d)-f) a frequency ratio of $\omega_2/\omega_1 = 1.3$. The comparison between the reflected pulse trains in b) and e) and the electron density oscillations in c) and f) clearly shows the narrowing of the HHG window.

Figure 3.18 proves that this method is able to shorten the pulse train substantially. Hence we proceed to perform a proper parametric scan in order to unravel if there is an optimal frequency ratio for the attosecond pulse isolation, and the relation between the FWHM of the input pulse and the best isolation efficiency. The criterion to evaluate the goodness of our results is given by the number of pulses contained in the reflected train, as well as their intensity in relation to the most intense one. We define the isolation efficiency (ξ) as:

$$\xi = \prod_{j=1}^{N-1} \left(1 - \frac{I_j}{I_0}\right) \tag{3.15}$$

where $N > 1$ represents the number of pulses in the train with a peak intensity I_j above 5% of the maximum peak. If $\xi = 1$ the isolation is perfect. Increasing the number of pulses in the train or their relative intensity to the most intense pulse, provokes a decrease in ξ up to the limit when the pulse cannot be regarded as isolated anymore ($\xi \sim 0$). This definition of the efficiency permits us to obtain a low isolation efficiency both if there are few pulses in the train with a high intensity in relation to the most intense pulse or if there are several pulses in the train with a low relative intensity.

We have performed simulations for frequency ratios (ω_2/ω_1) between the values 1 and 2 and for several FWHMs in between 5 fs and 55 fs. For each pulse width we have checked for the frequency ratio that yields to the highest isolation efficiency and the corresponding efficiency. Figure 3.19 shows the results obtained for input pulses with a FWHM of a) 10 fs, b) 25 fs and c) 40 fs. In the left column it is shown 2D maps that depict, for each frequency ratio, the pulse train obtained over time (normalized to the maximum at each frequency ratio, for the sake of visualization), these 2D maps demonstrate that the shape of the pulse train over time varies for different frequency ratios. In the two columns on the right, the isolation efficiency and the intensity of the most intense pulse in the train are shown, respectively, the former is plotted to demonstrate quantitatively that the isolation efficiency varies with the frequency ratio and the latter to show the normalization factor (the maximum intensity on the pulse train) for each frequency ratio in the normalized 2D maps of the left column.

Figure 3.19 reveals several interesting features of this gating method. First of all, it is clear that different isolation efficiencies can be obtained by tuning the frequency shift between the two pulses. The optimal ratio for isolation is shifted upwards as the pulse FWHM decreases. This makes sense, because for a narrower envelope the "slow" frequency $(\omega_2 - \omega_1)$ must be increased in order to oscillate within the envelope

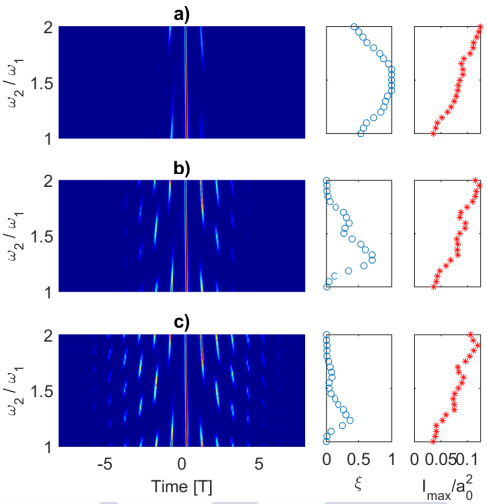

Figure 3.19: Results of the parametric scan for different pulse widths of a) 10 fs, b) 25 fs and c) 40 fs. In the left column it is displayed the train of pulses over time for each frequency ratio. The signal is normalized to the most intense pulse in each frequency ratio. In the right columns the isolation efficiency (ξ) and the maximum intensity in the central pulse of the train is depicted for each frequency ratio.

width, as it could be already inferred from figure 3.17. Secondly, as the ratio between frequencies goes beyond this optimal value, the oscillatory laser field peaks return to their original position with high frequency corrections (as shown in figures 3.16 c) and 3.17), causing the generation or more complex dynamics at the plasma surface and the creation of pulse trains with several ultrashort pulses in them, with a higher peak intensity, as it can be observed in figure 3.19 when the frequency ratio approaches the value 2. It can be also noted that, as the FWHM of the pulse increases, the maximum isolation efficiency decreases, therefore establishing a limitation for this gating method. On the other hand, if the pulse width is too low, the pulse envelope itself isolates a single attosecond pulse, due to the existence of a few oscillations within the pulse width. In this case the use of a gating method becomes pointless and high isolation efficiencies are achieved for several frequency shifts. An example is shown in figure 3.19 a), where for a frequency ratio equal to the unity (i.e. the pulse original shape), for a pulse with a FWHM of

10 fs, the isolation efficiency is nearly the same as in the most optimal case for a pulse with a FWHM of 40 fs, as shown in figure 3.19 c). It is clear that there is a frequency ratio for which the isolation is optimal, and that it varies with the pulse width.

To further emphasize these results, we have also analyzed how the train of attosecond pulses is changed by fixing a certain frequency ratio and varying the laser pulse FWHM. Figure 3.20 shows the incident laser field as well as the reflected train of pulses for two fixed frequency ratios and two different values of the FWHM. It is clear from this figure that the optimal frequency ratio varies for different pulse widths. In figure 3.20 a), in which a frequency ratio of 1.4 has been used, it can be seen that the isolation is better for the width of 15 fs, in comparison with the case in figure 3.20 b), in which a frequency ratio of 1.2 has been used, whereas the opposite occurs for the pulse with a FWHM of 30 fs, in Figs. 3.20 c)-d), where the isolation efficiency is higher for a ratio of 1.2.

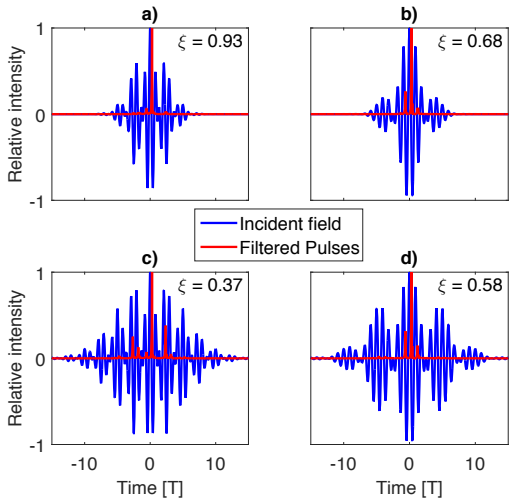

Figure 3.20: Trains of pulses generated for the mix of pulses with a frequency ratio of a)-c) $\omega_2/\omega_1 = 1.4$ and b)-d) $\omega_2/\omega_1 = 1.2$. The pulses FWHM are a)-b) 15 fs and c)-d) 30 fs. The isolation efficiency is shown in the upper-right corner of each plot.

To summarize the results obtained from the parametric scan, figure 3.21 shows the optimal frequency ratio and the maximum isolation efficiency found for each FWHM. It depicts how as the pulse FWHM

increases, the frequency ratio for an optimal result decreases and the isolation efficiency in the best scenario decreases as well, which establishes a limitation to isolate an attosecond pulse with a given FWHM. Interestingly, this decrease slows down as the FWHM increases, reaching a limit value for the frequency ratio of 1.2, while on the other hand the isolation efficiency decreases as the FWHM increases, as expected.

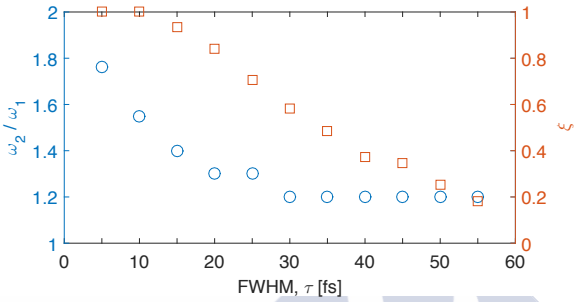

Figure 3.21: Frequency ratio (blue circles) for the optimal isolation and the associated isolation efficiency (red squares) for each FWHM.

It is possible to estimate the dependence of the optimal frequency ratio for the attosecond pulse isolation on the FWHM of the laser pulse. Establishing a criterion to determine when the width of the central part of the slow oscillating wave is short enough and the peak of the second maximum of the slow envelope is low enough, we can obtain a curve that relates the ratio and the FWHM for the optimal isolation. This curve in general will depend on the envelope of the laser pulse, as it determines the overall shape of the resulting field, which means that the results in figure 3.21 would change for a $\sin^2$ or a rectangular envelope, for example. In our case the slow oscillating envelope is given by:

$$|E_{slow}| = e^{-4\log(2)\left(\frac{t}{\tau}\right)^2} \left|\cos\left(\frac{R_\omega - 1}{2}\omega t\right)\right| \tag{3.16}$$

where we have defined the quantities $R_\omega \equiv \omega_2/\omega_1$ with $\omega \equiv \omega_1$ for simplicity.

A very simple criterion to calculate the curve for optimal isolation is established by analyzing the peak of the first local maximum of the

slow envelope (after the central one). This first maximum occurs when $\frac{R_\omega - 1}{2}\omega t = \pi$ and its value is given by:

$$E_{peak} \equiv \left| E_{slow}\left(t = \frac{2\pi}{\omega\left(R_\omega - 1\right)}\right)\right| = e^{-\frac{16\pi^2 \log(2)}{(R_\omega - 1)^2 \omega^2 \tau^2}} \tag{3.17}$$

We assume that when this peak has a certain constant value, the HHG efficiency outside of the central region is such that the isolation is the most optimal. This approximation assumes that there will be at least a local maximum in the beating pattern apart from the central one, therefore it implicitly assumes that it will work only for FWHM above a certain value.

The curve that gives a constant value in equation (3.17) is given by:

$$R_\omega = 1 + \beta \frac{4\pi\sqrt{\log(2)}}{\omega\tau} \tag{3.18}$$

where β is a free parameter given by the fixed constant value for E_{peak} by the equation $\beta = (-\log(E_{peak}))^{-1/2}$, by fitting this parameter to the obtained data we implicitly overcome the assumption for the width of the central region, since fixing the value of E_{peak} will yield to a specific width of the central region in terms of the FWHM.

By performing a numerical fit to the data, it can be seen that the best fit is given by the equation $R_\omega = 1.157e^{2.356/\tau}$, that approximated for $\tau \gg 2.356$ can be written as $R_\omega \approx 1.157 + 2.726/\tau$. This approximated curve is similar to our theoretical estimation in equation (3.18) for $\beta = 0.612$, given by $E_{peak} \approx 0.07$, and adding a constant term of 0.157. Figure 3.22 shows the obtained data from the simulations plus the theoretical curves for different values of E_{peak} and it also shows the numerical fit plus the theoretical equation modified by adding the constant $\delta = 0.157$. It can be seen that, although coming from a very simplistic approximation, the results and the theoretical curves are similar for the highest values of the FWHM.

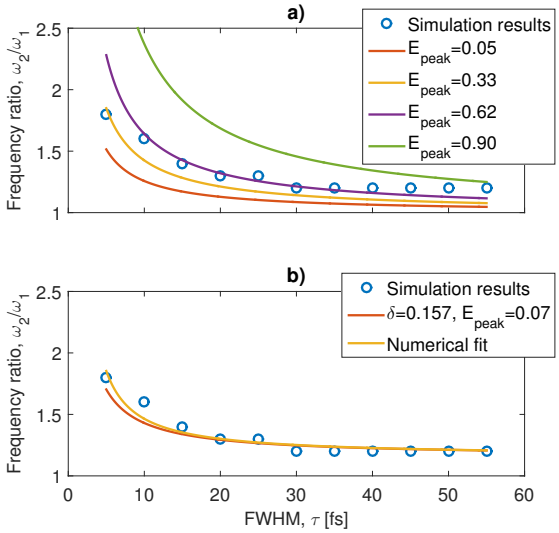

Figure 3.22: Optimal frequency ratios for each FWHM plus a) theoretical curves obtained from our simple estimation and b) best numerical fit plus our modified theoretical curve.

3.4.2.1 Effect of deviations from ideality

The results shown before rely on a very ideal situation, in which the pulses have a perfect gaussian shape and are perfectly phase-matched, or the pre-plasma does not exist. This is an approximation and does not match the case corresponding to a realistic situation, where it is difficult to implement a setup exactly like the one described for this frequency gating technique. In light of these facts, we will briefly address the effect of the global phase difference between the two pulses and of the existence of a pre-plasma.

The 2D maps in the left column of figure 3.19 show an asymmetry in the pulse train in relation to the location of the central pulse, this is more obvious in figure 3.19 b)-c), where the train of pulses is longer than in figure 3.19 a), and the central attosecond pulse does not get fully isolated, even in the most optimal configuration. A variation of the carrier envelope phase (CEP) of the input laser pulse could vary the shape of the train, contributing to an enhancement or a deterioration

of the isolation efficiency. We have analyzed the effect of varying the CEP of the input pulse from $0°$ to $360°$ for the most optimal ratio for two pulses with a FWHM of 25 fs ($\omega_2/\omega_1 = 1.3$). Figure 3.23 a) shows a 2D map of the resulting pulse train for each CEP, normalized to the maximum intensity at each CEP for the sake of visualization. A change in the global phase of the input pulse affects the shape of the attosecond pulse train, as it is shown in figure 3.23 b). In this figure we can observe the isolation efficiency for each CEP, revealing how crucial is to choose the CEP wisely. Increasing the CEP produces a decrease in the isolation efficiency until a minimum is reached at a CEP of $130°$, where it becomes almost zero. After this value, the isolation efficiency increases again until achieving a value approximately constant in the CEP range $[260°,\ 360°]$. The plots in figure 3.23 c)-d) display the input laser pulse and the obtained attosecond pulse train for c) the optimal isolation case with a CEP of $0°$ and d) the worst case at $130°$. They have been included to highlight the shape of the input pulse and the attosecond pulse train for different CEP. We can conclude that a good control over the CEP is needed to guarantee the optimal isolation of the attosecond pulse.

The effect of the pre-plasma is also an important factor to take into account, since we already know that can change substantially the outcome of HHG. In all previous simulations it has been used a steep plasma profile, in which density grows from zero to the assumed solid density with a step-like function. Here we analyze the effect of the existence of a pre-plasma for the proposed gating technique.

To address the effect of pre-plasmas, we have chosen the optimal frequency setup for three different pulse widths of 15, 20 and 25 fs. In this way we will be able to observe the effect of the pre-plasma and its dependence on the pulse width, if there is any. Figure 3.24 displays the effect of the existence of a pre-plasma in the a) isolation efficiency and b) intensity of the most intense ultrashort pulse.

Figure 3.24 depicts, for the three FWHM studied, that although the intensity of the central pulse grows substantially for a group of scale-lengths, the isolation efficiency lowers as the scale-length increases, which means that not only the most intense pulse is poorly isolated,

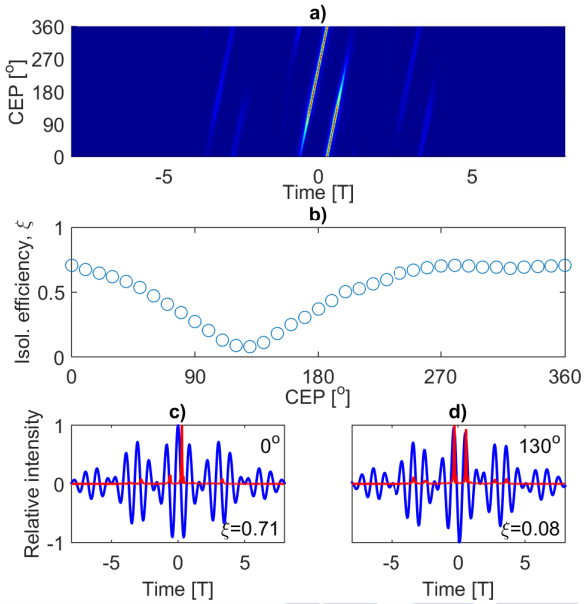

Figure 3.23: Results obtained varying the CEP with a pulse of FWHM $\tau = 25$ fs and a frequency ratio of $\omega_2/\omega_1 = 1.3$. a) A 2D map shows the temporal shape of the attosecond pulse train varying the CEP, the signal is normalized to the most intense pulse for each CEP. The isolation efficiency for each CEP is shown in b). Panels c) and d) show the input pulse (blue) and the corresponding attosecond pulse train (red), both normalized to the unity, at c) CEP$= 0°$ and d) CEP$= 130°$

but due to its increase in intensity, the accompaning pulses will be also more intense in absolute terms. The isolation efficiency, in figure 3.24 a), presents a decrease as soon as the pre-plasma is taken into account, and it keeps approximately constant until it drops to zero. The maximum intensity on the pulse train, in figure 3.24 b), experiences a similar trend, having a linear growth until an scale-length of 0.3λ and a plateau for the rest of scale-lengths, with a slight decrease for the highest scale-lengths evaluated. Both plots show two local maxima at the scale-lengths of 0.3λ and 0.6λ, respectively. This behaviour could be related to the fundamental processes of HHG in overdense targets, since long pre-plasma regions change the balance between the different absorption mechanisms and modify the particle dynamics at the plasma surface. The growth of approximately one order of magnitude of the peak intensity

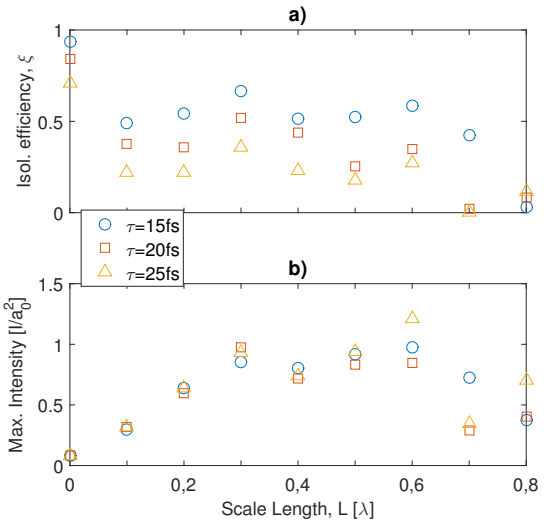

Figure 3.24: Effect of the pre-plasma on the gating technique displayed in the a) isolation efficiency and b) intensity of the most intense pulse of the train. The frequency ratio is chosen as the optimal one for each FWHM, that is $\omega_2/\omega_1 = 1.4$ for $\tau = 15$ fs and $\omega_2/\omega_1 = 1.3$ for $\tau = \{20,\ 25\}$ fs.

in the attosecond pulse train is in accordance with the enhancement of HHG for targets with a pre-plasma. These results demonstrate that the existence of a pre-plasma region will be detrimental for the functioning of this gating technique.

In conclusion, it has been proven that the combination of two laser pulses of equal amplitude and envelope, with a properly tuned small frequency shift between them, creates a beating pattern that yields to the isolation of a single attosecond pulse once high harmonic orders have been filtered in the reflected field. This frequency gating works well for a wide range of FWHM below ~ 35 fs, being able to isolate one or a few attosecond pulses. The experimental implementation of this method would require a good control over the central frequency of the two pulses involved and the carrier envelope phase, as it has been proven that it can affect the shape of the attosecond pulse train substantially. The existence of pre-plasmas has been proven detrimental for this gating techinque, therefore its optimal implementation would require the use of very high

contrast laser pulses. Its impact could be interesting in comparison with other gating methods, being an additional way to isolate attosecond pulses.

3.5 MANIPULATION OF THE ATTOSECOND PULSE POLARIZATION

It is very interesting to have control over the properties of the attosecond pulse train for several applications. One of these properties is the polarization state of the attosecond pulses, being in particular attractive the generation of circularly polarized ultrashort pulses, that find their application in atomic physics and magnetism at the nanoscale, where it is possible to study the spin dynamics of magnetic materials [215] or the lattice and electronic properties of graphene [216, 217], for example, with X-ray magnetic circular dichroism [218], a technique that can be also used with circularly polarized XUV-Soft X Ray attosecond pulses from HHG [219].

The possibility of achieving circularly polarized sub-femtosecond pulses was recently demonstrated using gas targets [220–222], where this result is achieved by combining two non-collinear and frequency-shifted laser pulses in the gas target. In laser-plasma interaction, it was very recently shown in a very simple manner that the polarization of laser-plasma generated attosecond pulses can be manipulated to achieve, in general, elliptically polarized trains of pulses [59, 60], however the degree of knowledge on how these pulses are generated, which are their most optimal setups or which are their properties is very low.

In this section we demonstrate how to control the ellipticity of attosecond pulses in laser-plasma interaction for a wide range of parameters related to the RES regime. In particular we demonstrate the production of circularly polarized attosecond pulses for a big variety of setups. Moreover, we show that RES theory [44] perfectly describes the polarization properties of the generated attosecond pulse train for arbitrary polarization and angle of incidence of the laser pulse. By choosing the interaction parameters accordingly, one can therefore produce XUV pulses of any preassigned ellipticity. The results in this section are currently under peer review [223].

The idea behind this study is that when non-linearly polarized pulses are used to generate harmonics, the harmonics are generated in both polarization components, with both odd and even parity and with comparable amplitudes. This is a concept long known from the HHG selection rules, however it had never been used to produce elliptically polarized attosecond pulses until very recently. Knowing this, we propose to perform a parametric scan varying the polarization state of the input pulse and its angle of incidence, and analyzing the polarization state of the produced attosecond pulses, once a part of the HH spectrum is filtered. This study will allow us to determine which are the configurations that produce circularly polarized pulses and if there is a parameter region that can be parametrized in order to lead experimentalists towards the application of these results.

Before introducing the results, we will briefly present some of the parameters that will be used to describe the polarization states. A wave with a certain polarization state impinging onto a surface with an angle of incidence θ can be described by the combination of two perpendicularly polarized fields, with a phase difference ϕ between them. For a field propagating towards the surface $x = 0$, the complex expression of the field will be:

$$\vec{E} = \frac{a_0}{\sqrt{E_p^2 + E_s^2}} \left(E_p \hat{p} + E_s e^{i\phi} \hat{s} \right) e^{i\varphi} \tag{3.19}$$

where for simplicity we have considered a plane, infinite wave. The variable $\varphi \equiv \vec{k} \cdot \vec{r} - \omega t = \cos(\theta)x - \sin(\theta)y - \omega t$ is the propagation phase. The $\hat{p} = \sin(\theta)\hat{x} + \cos(\theta)\hat{y}$ and $\hat{s} = \hat{z}$ vectors refer to the P-polarized and S-polarized components of the pulse, that is the component contained in the incidence plane and the one perpendicular to it, respectively. These components have a normalized amplitude E_p and E_s, respectively.

A polarization state can be characterized by two different sets of variables: (1) the ratio between the minor and the major of the two components, that is $\eta = E_s/E_p$ if $E_s < E_p$ and viceversa, and the difference of phase ϕ between them or (2) the azhimut Ψ, which is the inclination of the polarization state (in general of the major axis of the ellipse) with respect to the plane of incidence, and the ellipticity ε,

which is the ratio between the minor and major axes of the ellipse in the polarization plane. Figure 3.25 exemplifies these parameters by showing both polarization components, their 3D view and their polarization state.

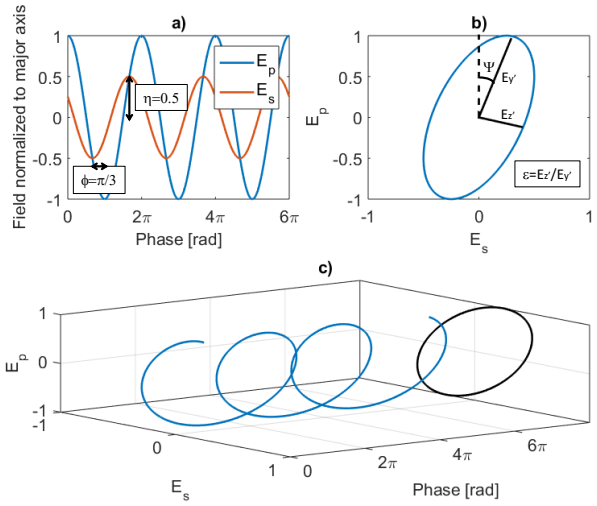

Figure 3.25: Example of an elliptically polarized pulse. a) The input polarization components, indicating the phase difference ϕ and the ratio η, b) integrated view of the polarization state in the polarization plane, indicating the azhimut Ψ and the ellipticity ε and c) a 3D view of the polarization state, with the integral over the propagation direction.

It is possible to make a transformation from one set of variables to the other, taking into account that the azhimut can be calculated by:

$$\tan(2\Psi) = \pm\frac{2\eta}{1-\eta^2}\cos(\phi) \tag{3.20}$$

where the $\pm$ sign is used depending on where is the major axis, in the P-polarization axis $(+)$ or in the S-polarization axis $(-)$. The system of axes in which E_p and E_s are defined can be rotated by that angle, in order to be in the axes system $(y',\ z')$ where the ellipse is centered. The new components, referred to the new axis system, can be written as:

$$E_{y'} = \cos(\Psi)E_p - \sin(\Psi)E_s e^{i\phi} \tag{3.21}$$
$$E_{z'} = \sin(\Psi)E_p + \cos(\Psi)E_s e^{i\phi} \tag{3.22}$$

The ellipticity would be finally calculated from the ratio between the minor and the major of the modulus of both components, that is $\varepsilon = |E_{z'}|/|E_{y'}|$ if $|E_{z'}| < |E_{y'}|$ and viceversa.

As an example, we can apply equations (3.20-3.22) to the case shown in figure 3.25, where the ratio is $\eta = 0.5$ with the major axis P-polarized and the phase difference is $\phi = 60°$. The azhimut is then given by $\Psi = 16.9°$ and the ellipticity is $\varepsilon = 0.40$, which is consistent with figure 3.25 b).

Knowing all the parameters involved in the characterization of a polarization state, we can show the results on the control of the polarization of attosecond pulses. Taking as an example the previous works on this topic [59, 60], it is clear that a non-linear pulse under a non-zero angle of incidence will produce harmonics and attosecond pulses with an elliptical polarization state. We have performed a parametric scan by changing the polarization state of the input pulse and its angle of incidence and analyzing the polarization state of the attosecond pulses.

This study requires the analysis of a 3D set of data, that would easily require to run several thousands of PIC simulations and would require a enormous amount of humane and computer work. However, it is known that the RES model is able to reproduce the motion of the electrons at the plasma surface and the shape of the reflected field, once the parameters employed are in what can be defined as "RES regime", that is a dimensionless field amplitude $a_0 \gg 1$ and a relativistic similarity parameter $S = n/a_0$ in the range $[0.05,\ 5]$. Therefore in order to avoid the inconvenience of running such a huge amount of simulations, we performed our study with RES calculations. In order to justify the use of RES calculations, we need to demonstrate that their predictions match those from PIC simulations to demonstrate that (1) the RES theory provides an overall accurate description for this problem and (2) the results can be scaled to various plasma densities and laser amplitudes as they predominantly depend only on the ratio S between them.

For this purpose we perform three equivalent PIC simulations varying the values of the radiation amplitude a_0 and the plasma density n, that are changed proportionally so that $S = n/a_0$ is the same for all cases. In the simulations the incident laser radiation has a form of cir-

cularly polarized pulse with a rectangular profile and a duration of 3 periods. This pulse takes values for the amplitude a_0 of 190, 100 and 50 and impinges at an angle of $\theta = 45^\circ$ onto a plasma with a steep density profile and density n of 360, 190 and 95, respectively. PIC simulations were performed in 1D with the boosted frame technique and using the code PICADOR [191, 192] with the following parameters: A spatial and temporal resolution of 0.0012 in simulation units, in which a laser pulse with a length of 3λ and a rectangular profile interacts with a plasma with a width of λ and a steep density profile, with a number of 100 particles-per-cell in it. The simulation runs until the whole pulse is reflected, that is the time it would take if the plasma behaved like a perfect mirror. Figure 3.26 shows a) the temporal evolution of the electron density distribution, as well as of the reflected field b) S-polarized and c) P-polarized components. The simulation results are compared with the numerical computation of the differential equations of the RES theory (see reference [44]) and a perfect agreement can be clearly seen.

It is important to note that the different values of amplitude used in figure 3.26 can potentially affect the degree of ion motion and the role of radiation reaction. We thus account for these effects in our PIC simulations. In terms of charge to mass ratio the considered cases can be related to the Cu ions ionized twice, four and eight times. However, since we here consider only the physics of laser-plasma interaction, we leave the questions about the realistic material density and the level of ionization outside the scope of this thesis. Figure 3.26 demonstrates that the results are well scalable at least down to $a_0 = 50$ and do not alter significantly due to the ion motion and radiation reaction for amplitudes at least up to $a_0 = 190$, at least within three laser cycles. By using extreme values for the amplitude of the laser pulse, we can clearly observe that our study must be restricted to the limits where the RES model applies and other effects neglected in the model like ion motion can be indeed neglected. Figure 3.27 shows a comparison of the reflected field between three cases with the same S parameter, one in which the RES model does not apply ($a_0 = 1$), one in which the RES model applies and other effects can be neglected for our pulse length ($a_0 = 100$) and one in which, within three laser cycles, we can begin to see a deviation

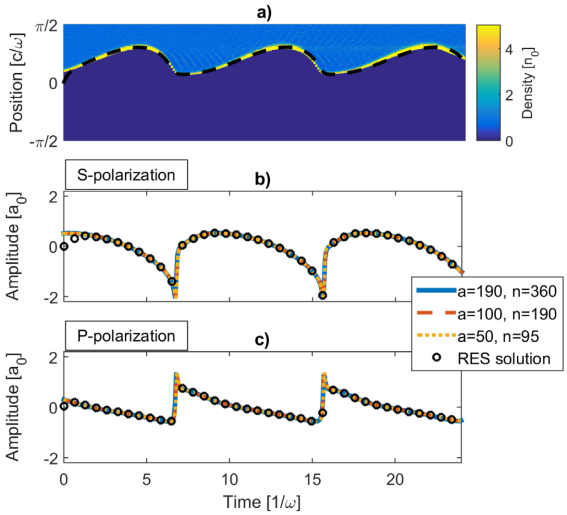

Figure 3.26: The results of PIC simulations for several amplitudes a_0 (see values in the inset) of a circularly polarized pulse incident obliquely ($\theta = 45°$) onto a plasma with the proportional density n so that $S = n/a_0 = 1.9$: the electron density distribution in the boosted frame a) and the reflected electric field components in S-polarization b) and P-polarization c). The results are in perfect agreement with the RES theory calculations that are shown through a): the thin sheet position (dashed curve) and b)-c): the reflected field components (circles) as functions of time.

of the results due to ion motion ($a_0 = 1000$). These fields are plotted along with the results predicted by the RES model (black circles).

Based on the obtained agreement and knowing the limits of applicability, we can now use the RES theory for assessing the opportunities for varying the ellipticity of the attosecond pulses through the variation of the interaction parameters. To characterize the polarization state of the laser radiation we use two parameters: the ratio η of the smaller of the P-polarized and S-polarized component amplitudes to the larger of the two and the phase difference ϕ between the components. We vary the angle of incidence θ, the ratio η, and the phase difference ϕ. The parameter space spans angles of incidence θ between $[0°,\ 60°]$, phase differences ϕ between $[0°,\ 90°]$ and ratios for the component amplitudes between $[0,\ 1]$. We consider both the case when the amplitude of the P-component is larger than the one of the S-component and viceversa. In the limit of $\eta = 0$, these cases correspond to P-polarization and S-

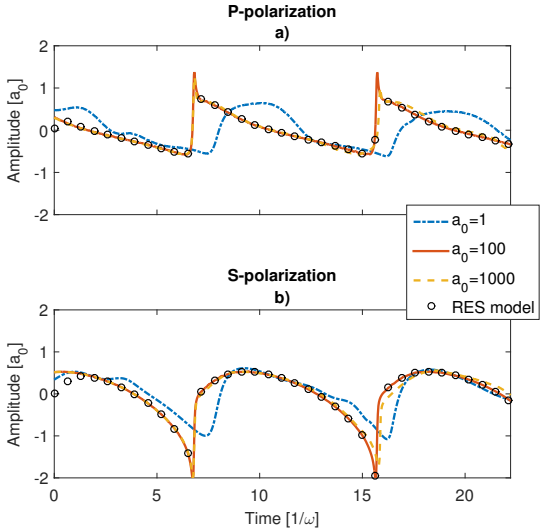

Figure 3.27: Results of PIC simulations and results predicted by the RES model (black circles) for several amplitudes a_0 of a circularly polarized pulse incident obliquely ($\theta = 45°$) onto a plasma with the proportional density n so that $S = n/a_0 = 1.9$. The clear deviation in the limiting cases ($a_0 = \{1,\ 1000\}$) demonstrates that our calculations are restricted to a specific set of values for the laser amplitude.

polarization, which we use to denote them on the diagrams. For the outgoing radiation we filter out the harmonic orders outside the range of $\omega \in [30,\ 60]$ and calculate the ellipticity ε of the resulted burst of radiation. These calculations are done for two values of similarity parameters $S = 1.9$ and $S = 0.3$.

Before showing the results of the parametric scan, figure 3.28 is presented to explain how the ellipticity of the attosecond pulses from a RES calculation is obtained, in this case for circularly polarized attosecond pulses. The spectrum of the reflected fields is calculated, and with it the ratio between the harmonic peaks. The ponderated average of all these ratios in the filtered HH region gives the ratio between the attosecond pulse components, whose phase difference is measured in the region of interest where they are emitted. The ratio and phase difference between the components are afterwards used to measure the azhimut Ψ and the ellipticity ε.

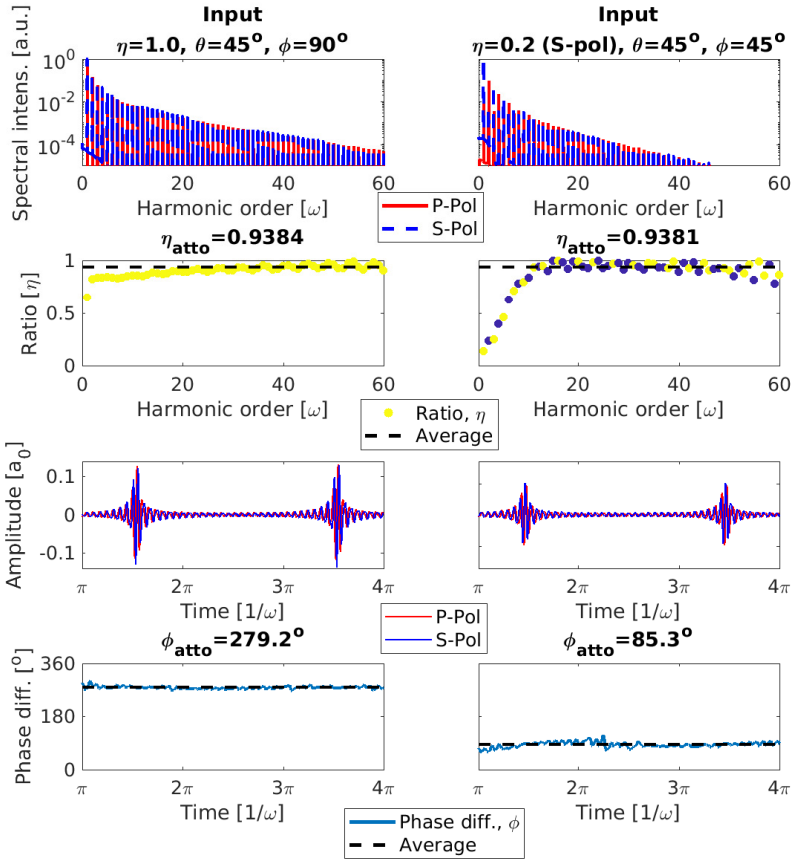

Figure 3.28: Example of a circularly polarized train of pulses for two different inputs. Each of the rows show: the spectrum of both components, the ratio between each of the harmonic peaks (colored depending on which is the major axis, yellow if the major axis is the same as the input one), the filtered train of pulses (enlarged to see the details) and the phase difference between the pulses. The ellipticity for each of the cases is $\varepsilon = 0.88$ for the left column and $\varepsilon = 0.98$ for the right column.

The results from the parametric scan are shown in figure 3.29. The top panels of figure 3.29 show 2D maps of the ellipticity of the filtered attosecond pulses, that are built by fixing one of the parameters of the parametric scan in each row of the figure (the fixed values have been chosen arbitrarily). The results for the ellipticity in the three-dimensional

space of parameters are shown in the last row of figure 3.29, showing isosurfaces for the ellipticity of the attosecond pulses.

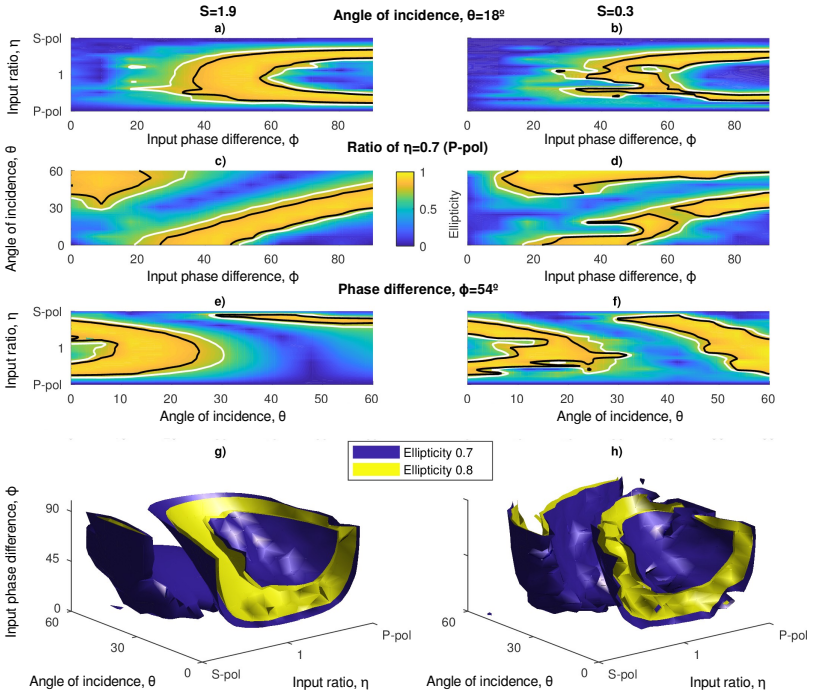

Figure 3.29: Ellipticity of the filtered attosecond pulses for the case of $S = 1.9$ a), c), e), j) and $S = 0.3$ b), d), f), h). Results are shown for three examples of input parameters: $\theta = 18°$ a)-b), $\eta = 0.7$ with the P-polarized component being the major one c)-d) and $\phi = 54°$ e)-f). The contours indicate ellipticities of 0.7 (white) and 0.8 (black). The panels j) and f) show the isosurfaces for the ellipticity equal to 0.7 (blue) and 0.8 (yellow) in the three-dimensional space of parameters.

In figure 3.29 we can distinguish two isolated prominent regions of parameters that correspond to the generation of almost circularly polarized ($\varepsilon > 0.8$) attosecond pulses. The first region spans from $\theta = 0$ to $\theta \approx 40°$ and remains almost unchanged for both $S = 0.3$ and $S = 1.9$. This region can be roughly fitted by an expression that could be used to guide experiments and the development of a reliable source of circularly polarized XUV pulses:

$$\left(\frac{1-\eta}{0.7}\right)^2 + \left(\frac{90-\phi}{54}\right)^2 = \left(\frac{64-\theta}{57}\right)^2 \tag{3.23}$$

The second region appears only for large incidence angles $\theta > 45°$ and is more broad for $S = 0.3$ than for $S = 1.9$. The fact that it is more prominent for small values of S points to the fact that this region appears as a unique feature of RES regime. In contrast to the first region, the second region can span to $\phi = 0$ (see, for example, ϕ-θ map for $S = 1.9$). This means that linearly polarized laser pulses under optimal orientation of the target can provide the generation of almost circularly polarized attosecond pulses.

We have demonstrated that circularly polarized attosecond pulses can be produced in a variety of configurations for the polarization of the input laser pulse and its angle of incidence. However, the emitted amplitude varies across these configurations (as illustrated in the examples of figure 3.28), therefore one can search for the configuration that leads to the most intense circular pulse. For $S = 1.9$ the highest amplitude is obtained for $\theta = 36°$, $\phi = 81°$ and $\eta = 0.5$ with the P-polarized axis being the major one. For these parameters the generated pulse has the duration of $\tau = 85$ as (FWHM for intensity), an ellipticity of $\varepsilon = 0.84$ and an amplitude of $0.29a_0$, which is, to our knowledge, higher than reported elsewhere [59, 60]. Figure 3.30 illustrates the pulse train for this case. It displays the spectral and temporal form of a pulse train for both the RES model calculations and PIC simulations, showing a good agreement between them.

We can conclude that in the RES regime of laser-plasma interaction the ellipticity of generated attoseconds bursts can be tuned in a wide range of values by adjusting the target orientation and the ellipticity of the incident laser radiation. Achieving almost circular polarization is possible in a variety of configurations within two regions distinguishable in the space of related parameters: one region appears for incidence angles $\theta > 45°$ and another for $\theta < 40°$. The region for large angles becomes more prominent for small values of relativistic similarity parameter S and thus can be uniquely attributed to RES regime. It is notable that this region indicates the possibility of producing almost circularly polarized

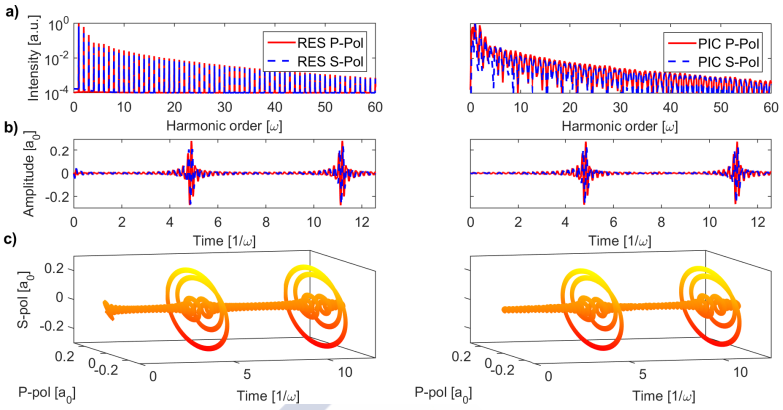

Figure 3.30: Circularly polarized pulses obtained for the optimal parameters when $S = 1.9$. The left column represents the result from RES calculations and the right column those from PIC simulations. In each row it is shown a) the reflected spectral intensity for both polarization components, normalized to the fundamental harmonic order, b) the temporal shape of the pulses obtained from filtering the harmonic orders between 30 and 60 and c) a 3D view of these pulses, to better highlight their polarization state.

bursts by linearly polarized laser radiation under the appropriate orientation of the target. The region for small angles does not alter significantly with the change of S. The provided mathematical fitting for this region can thus be used as a universal robust guidance for experiments and further developments. For obtaining more accurate predictions with the account for particular pre-plasma and laser parameters one can make calculations with RES theory [44], which was shown to be in a perfect agreement with PIC simulations in the performed study.

3.6 CONCLUSIONS

The generation of high harmonic orders of the laser central frequency when an intense laser pulse and a solid material interact is a nonlinear mechanism that has as a product the emission of ultrashort pulses, typically below the femtosecond, once a high harmonic region of the reflected spectrum has been filtered. These pulses can be used in several timely applications as a sensing tool in atomic physics or in the study of materials at the nanoscale, for example.

In this chapter, first we have introduced the properties of this harmonic generation and their related attosecond pulses, and after we have

introduced techniques to manipulate the properties of the attosecond pulse train to make it suitable for different applications.

We have proposed a new setup for the implementation of a polarization gate consisting on the use of Cross Polarized Wave Generation crystal, a $\lambda/4$ wave plate and a dispersive material. This setup overcomes the need for few-cycle pulses of very high intensities ($I \gg 10^{18}$ W/cm^2), needed for other setups, and therefore its implementation would be less costly than in other known setups.

We have introduced a new gating method, named Frequency Gating, that consists on the coherent combination of two frequency shifted pulses, such that the resulting field forms a beating pattern that shortens the pulse train. We have addressed the quality of this method, that is able to isolate efficiently ($\xi > 0.5$) single attosecond pulses using gaussian laser pulses with FWHMs up to 35 fs. We have also addressed the limitations of this method, finding that an extremely good contrast of the input pulse, a good control over the CEP and a well defined central frequency are needed.

Finally, we have shown, using the RES model, how the polarization of the attosecond pulse train changes by varying the polarization state and the angle of incidence of the laser pulse. We have focused on the production of circularly polarized attosecond pulses, more interesting from the applied point of view, and we have found that the production of these pulses occurs in a wide variety of configurations, existing a region of the parameter space, that we parametrized mathematically as an ellipsoid, independent on the relativistic similarity parameter S (at least in the RES regime), for which circular pulses are always produced. This last result is very interesting, since it can lead the direction of experiments aiming to generate this kind of pulses in ultraintense laser facilities.

In summary, HHG in laser-plasma interaction with overdense targets is a very interesting mechanism for the production of sub-femtosecond pulses, whose properties can be tailored for several applications. The possibility of accessing easily to higher energies and intensities than those obtained for gas-generated attosecond pulses, suggests that in the future these pulses will be used more commonly than what they do now,

however there is still a big amount of theoretical and experimental work to advance in this field.

4 PROTON ACCELERATION

Proton acceleration via the TNSA mechanism has proven to be an efficient method to accelerate protons (or ions) into the MeV regime using table-top laser sources [6, 7]. Its general features and applications have been detailed in the introduction of this thesis. Here we will first show the basic technical details of this acceleration mechanism, to display afterwards a proposal to enhance the maximum energy of the accelerated protons by nanostructuring the target front surface [224].

As it was explained in the introduction, in this mechanism a high intensity laser interacts with a few-micron thick solid target to produce energetic ions [71, 76, 108, 110]. The laser pulse ionizes the target surface and heats up the electrons on it; these electrons propagate across the target due to the ponderomotive force that the laser pulse exerts over them and escape perpendicularly to the rear surface. This generates a spatial charge separation in the rear surface that yields a strong longitudinal field which can accelerate positively charged particles located in the vicinity of the surface, typically protons. The accelerated beam of particles via this mechanism has a clear directionality and an energy spectrum that decreases with increasing energy up to an abrupt cutoff. Figure 4.1 illustrates this process.

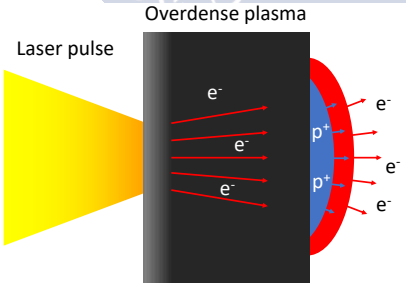

Figure 4.1: Illustration of the TNSA mechanism: a laser pulse is focused at the surface of an overdense plasma, pushing the electrons across the target. The accelerated electrons exit the target through the rear surface, generating a spatial charge separation that accelerates positively charged particles at the surface, usually protons.

PIC simulations are usually employed as a tool to study the properties of the ion beam and the characteristics of this mechasism. These simulations allow us to calculate on a nanometric scale the interactions that govern this particle acceleration mechanism, being able to provide reliable results that can be verified in a laboratory afterwards. Since the motion of the particles is the most important factor to take into account in these simulations, in order to provide reliable results in quantitative and qualitative terms, the simulations must be performed in 3D, however it is extremely expensive, in terms of calculation time, to perform realistic 3D TNSA simulations with a proper numerical resolution and allowing also for enough expansion time, therefore two-dimensional simulations are usually chosen to study the properties of TNSA as a first approach. While it is known that 2D simulations overestimate the accelerating longitudinal field and the energy of the accelerated protons [225, 226], they are able to give valid results in qualitative and relative terms, and they are a very common tool to study this acceleration mechanism.

Figure 4.2 shows an example of the outcome of a TNSA acceleration process. In this example, a laser pulse impinges normally on the surface of a flat target composed of three-times ionized silicon and electrons, with a thin layer on protons on the rear surface of lower density. The main target has a thickness of 2λ with a density of $90n_c$ and the proton layer has a thickness of 0.15λ with the same density. The number of particles per cell is 25 per species. The density has a steep profile as we consider a high contrast laser. The laser pulse is launched from the left wall of the simulation box, with a peak intensity of 3.45×10^{19} W/cm^2 ($a_0 = 4$), a FWHM of 25 fs (with a sin^2 temporal profile), a wavelength of $\lambda = 800$ nm and a focus with a gaussian spot of diameter 6 μm. The laser pulse is polarized in the simulation plane. The simulation box has a width and length of 50λ with a spatial resolution of 0.02 in simulation units, that is $\sim 0.0032\lambda$.

Several things can be observed from the simple example shown in figure 4.2. The TNSA simple picture is fulfilled: a) The electrons go across the target through the rear surface, generating a b) longitudinal field, that pulls the c) protons in the same direction, being accelerated in the d) normal direction of the target surface, with a e) clear directionality

and an f) energy spectrum with a clear cutoff. It can be observed that the proton cutoff energy is in the MeV range, even though only a very small percentage ($\sim 3\%$) of the laser energy has been absorbed by the plasma.

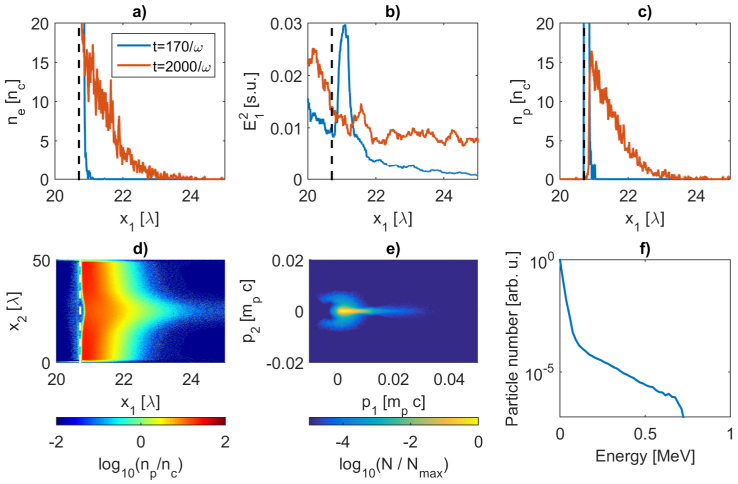

Figure 4.2: Results from TNSA for the simulation described in the text to illustrate the acceleration mechanism. The top panels show a line analysis on the laser propagation axis (x_1) at the center of the target ($x_2 = 25\lambda$) of a) the electron density, b) the accelerating longitudinal field and c) the proton density, at two different times: when the acceleration process its in its initial stage ($t = 170/\omega$) and when the protons reach a nearly constant energy ($t = 2000/\omega$). The bottom panels show the properties of the accelerated protons at the time $t = 2000/\omega$, such as d) the 2D proton density, e) the $p_1 - p_2$ phasespace and f) the energy spectrum. The dashed lines indicate the original position of the target rear surface, where the proton layer starts.

4.1 TARGET ENGINEERING TO IMPROVE THE TNSA OUTCOME

Proton acceleration via TNSA using table-top intense laser sources is able to yield accelerated protons in the MeV regime with controlled beam properties, however this is not sufficient for some applications, where higher energies or a higher particle number are needed. An interesting feature of TNSA is that it requires the use of solid targets, which can be manufactured with a variety of properties to make the acceleration more efficient. This subject has received a wide attention because the optimization of the targets opens a way to produce more energetic protons, or even to enhance other properties of the proton beam, without the need of increasing the laser power.

Different approaches to enhance the acceleration process by manipulating the target properties have been used: the simplest and most common of these approaches consists in varying the target thickness [115, 227–234], since the energy and density of the electrons on the rear surface (and thus the accelerating field) depend on how much material the electrons have to go across. It has been observed that if the pulse contrast is not good enough, that is if there is a long pre-plasma, the accelerated proton energy and number are maximized at a certain thickness, whereas for a suitable contrast, simulations show that the proton energy simply decays with increasing thickness. Other approach taken to enhance the accelerated particle properties consists in nanostructuring the back surface of the target [116, 117], in this way it is possible to distribute the proton contamination layer on such a way that the geometrical properties of the proton beam can be tailored and measured more accurately, or it is possible to manipulate the energy spectrum of the beam by reducing the transverse dimensions of the contamination layer. Some studies have also addressed the effect of growing a layer of low density foam on top of the target [118, 119, 235], which increases the number of electrons going across the plasma by letting the laser pulse energy to be absorbed by the low density foam, thus increasing the accelerated particle energy.

In the last few years, several publications have reported that adding periodic nanostructures on the target front surface enhances drastically the laser energy absorption [122, 235–242]. This generates protons with much higher energies than the ones obtained when targets with a flat surface are used [123, 235, 240–249], therefore these targets represent a very interesting candidate to study for applications where the energy of the protons has to be increased in comparison with the setup where a flat target is used. The nature of this enhancement is still a matter of discussion, as there are some models explaining why this happens, but there is not a solid theory yet, however it is known that the enhancement on the energy absorption and on the proton energy is strongly dependent on the shape of the structures, as well as on the angle of incidence of the impinging laser [122, 123, 235–237, 239, 240, 242, 246], that is in the geometry of the experiment. The variety of parameters and structures

that can be used to study this enhancement is quite big, thus leaving room for further research on the effects of different kinds of setups.

In summary, it is possible to modify the target properties to enhance several features of the proton beam for TNSA. Nanostructuring the target front surface represents a very promising candidate to improve the energy of the protons and the transfer of energy from the laser pulse to the electrons, thus making this acceleration mechanism available to applications that otherwise would not be possible to implement, without having to increase the laser intensity.

4.2 PROTON ACCELERATION IN NANOSTRUCTURED TARGETS

The main purpose of this section is to show how the geometry of periodic nanostructures on the target surface can be optimized to achieve a higher laser energy absorption and proton energies, in particular for triangular nanostructures. Several studies have addressed the effect of periodic nanostructures at the top of the target on proton acceleration via TNSA, these works have analyzed the effect of different structure shapes and dimensions, and it has been found that triangular nanostructures yield to higher absorption rates and more efficient proton acceleration in comparison with other kinds of structures, both in PIC simulations and experiments [122, 123]. The reason behind choosing triangular structures is that, although they have been found to yield to very interesting results, no extensive study of their effect on TNSA has been performed.

In this section, we introduce an analytical model to account for the increase in the energy absorption due to the presence of the periodic triangular nanostructures. Two-dimensional PIC simulations are performed afterwards to study the effect of the structure parameters, to find the optimal target design for obtaining maximal laser absorption and proton cutoff energy and to address the effect of using oblique incident laser pulses. The obtained results allow us to propose an optimal experimental configuration to acquire more energetic protons. Finally, the robustness of the results under deviations from the ideal situation is analyzed.

With the results obtained in this section, we are able to propose an optimal structured surface for improving the energy absorption as well as the energetic proton production, that could be fabricated and

used experimentally, providing a robust strategy to obtain higher energy protons without the need of using a higher laser intensity.

4.2.1 Analytical model of electron dynamics

In this subsection we introduce a simple analytical model to understand the electron motion in the presence of the laser field within the periodic structures at the target surface. The laser energy absorption is directly related to the electron heating, since electrons are the lightest particles in the plasma and the first to interact with the laser field. Understanding how electrons absorb the laser energy and carry it towards the rear of the target is crucial to select an optimal surface structure.

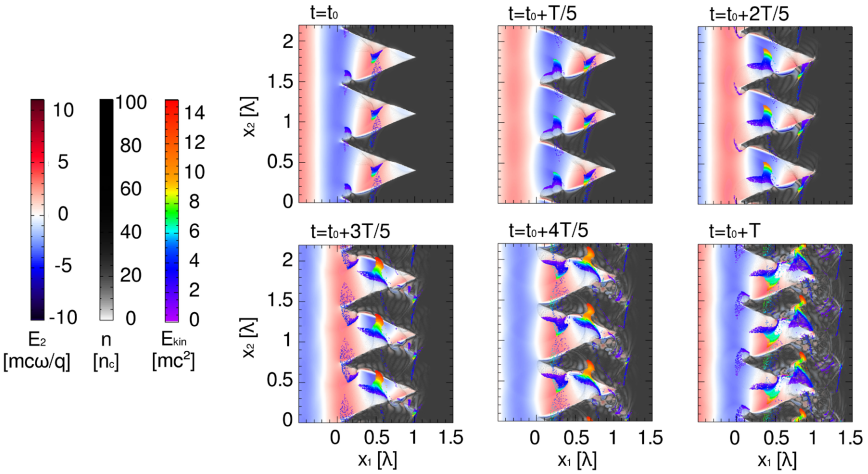

Figure 4.3: Illustration of the electron dynamics over a laser period T, taken from a PIC simulation, with six snapshots of the electron density, the E_2 component of the electric field, in which the laser field is polarized, and the most energetic electrons, coloured depending on their kinetic energy. The electrons move in the vacuum gap from one triangle to the next according the sign of the E_2 component of the electromagnetic field, gaining energy in the process.

The use of triangular structures in the front face of the target changes the local angle of incidence of the laser at the target surface and allows electrons to undergo a temporary interaction with the laser field in vacuum before recolliding with the target. As the laser arrives to the target, it strips off a portion of the electrons from the surface of the structure,

these electrons are accelerated by the laser field in the vacuum gaps of the structures and gain energy and they reenter the target where the laser cannot penetrate, carrying their energy through the target, as shown in figure 4.3. The dimensions of the triangular structures determine the time that the electrons spend being accelerated by the laser field in the vacuum gaps within the structure and their energy of recollision. Since the energy carried by the electrons is modified by the shape of the structures, we expect an optimal laser absorption for targets with geometrical properties that allow for maximum electron energy gain.

A simple model that neglects all fields except the laser one is useful to understand how the recollision energy is related to the triangle shape. The starting point is to consider the relativistic motion of an electron in vacuum under the influence of a linearly polarized electromagnetic wave given by the vector potential $\vec{A} = a_0(m_e c/\omega)\sin(\varphi)\ \hat{x}_2$. The variable $\varphi = \omega t - \vec{k}\cdot\vec{r} + \varphi_0$ represents the electromagnetic wave phase, $\vec{k}$ is the wave vector, $\vec{r}$ the particle position, ω the angular frequency, t the time and φ_0 is the initial phase. The equation of motion of an electron under this field in the vacuum gap is determined by the Lorentz force:

$$\begin{aligned}\frac{d\vec{p}}{dt} &= -q_e\vec{E} - q_e\left(\frac{\vec{p}}{\gamma mc}\times\vec{B}\right) = \\ &= \frac{q_e}{c}\frac{\partial\vec{A}}{\partial t} - q_e\left(\frac{\vec{p}}{\gamma mc}\times\left(\vec{\nabla}\times\vec{A}\right)\right)\end{aligned} \tag{4.1}$$

where q_e is the electron charge. This equation can be solved for the specified vector potential assuming that the electron is initially at rest with $\varphi = 0$. The momentum and displacement of the electron are given by [2]:

$$p_1 = \frac{a_0^2}{2}m_e c\sin^2(\varphi) \qquad p_2 = a_0 m_e c\sin(\varphi) \tag{4.2}$$

$$\Delta x_1 = \frac{a_0^2}{8\pi}\lambda\left(\varphi - \frac{\sin(2\varphi)}{2}\right) \qquad \Delta x_2 = \tfrac{a_0}{\pi}\lambda\sin^2\left(\tfrac{\varphi}{2}\right) \tag{4.3}$$

where the indexes "1" and "2" refer to the longitudinal and transverse field directions and $\lambda = 2\pi c/\omega$ is the laser field wavelength.

The maximum electron energy is reached when $\varphi = \pi/2$, because both components of the electron momentum are maximized, so if the electrons reenter the target at this point they will absorb the maximum possible energy from the field. The kinetic energy carried by the electron as a function of the phase is given by:

$$E_K(\varphi) = m_e c^2 \left(\sqrt{1 + \frac{a_0^4}{4} \sin^4(\varphi) + a_0^2 \sin^2(\varphi)} - 1 \right) \tag{4.4}$$

Reaching the optimal phase at the moment when the electron reenters the target is controlled by its initial position in the structured surface, expressed by its initial height, h_0. We can establish a relation between the initial height, where a single electron is located, and the phase when it arrives to the surface of the next triangle by using the displacements in equation (4.3). This relation is obtained from the following expression for the triangle angle:

$$\tan(\theta) = \frac{h}{w/2} = \frac{x_{1f}}{x_{2f}} = -\frac{h_0}{x_{2o}} \tag{4.5}$$

where h and w are the structure height and width and the indexes "o" and "f" indicate original and final position at the periodic structure surface, respectively. Taking into account the definition of the displacements $\Delta x \equiv |x_f - x_o|$, we can obtain the final equation $h_0 = \frac{1}{2}\Delta x_1 + \frac{h}{w}\Delta x_2$, which, written in our variables of interest, is given by:

$$h_0(\varphi) = \frac{a_0^2}{16\pi}\lambda \left(\varphi - \frac{\sin(2\varphi)}{2} \right) + \frac{a_0}{\pi}\frac{h}{w}\lambda \sin^2\left(\frac{\varphi}{2}\right) \tag{4.6}$$

The maximum amount of energy absorbed by the electrons in the gap is reached when $h_0(\varphi = \pi/2) \approx h$, this means that the electrons initially located at the tip of the structure gain the maximum possible energy. These electrons are the first to interact with the laser pulse. If $h_0(\varphi = \pi/2) > h$ the electrons will not reach the maximum energy because their ideal initial height is not allowed on the structure and when $h_0(\varphi = \pi/2) < h$ a portion of the electrons at the top of the structure

will stay longer in the vacuum gaps and will not enter the target with the optimal energy. It can be also noted that the second term on the right hand side of equation (4.6) becomes less relevant as a_0 increases. However, the findings of equation (4.6) cannot be applied directly to very high intensities where the hole-boring can destroy the pre-formed structures before the end of the interaction. We therefore restrict our analysis to a moderate laser intensity.

Using a laser field with a dimensionless amplitude of $a_0 = 4$, which corresponds to the specification of the STELA laser of the L2A2 facility of the University of Santiago de Compostela, with laser intensities on the order of 10^{19} W/cm^2 and a peak power on the order of tens of TW, the equation (4.6) for the maximum electron energy becomes:

$$h_0(\varphi = \pi/2) = \frac{\lambda}{2} + \frac{2}{\pi}\frac{\lambda}{w}h \tag{4.7}$$

The value of h_0 relative to h in the previous equation is controlled by the height and width of the structures. We can distinguish two cases, one for which $h < 0.5\lambda$ and other for which $h > 0.5\lambda$. In the former the initial height always verifies that $h_0 > h$, regardless of the structure width, therefore in this case not very high absorption percentages will be obtained. In the latter case, when the height is above 0.5λ it is possible to verify $h_0 = h$ and achieve the optimal recollision if the width is tuned properly. However, our model cannot be applied for structure widths much bigger than the wavelength, since in that case other absorption mechanisms will begin to take place, due to the flattening of the surface. Taking the limit $h \gg 0.5\lambda$, we can find an optimal structure width for improving the energy absorption, given by $w = 0.64\lambda$. When the structure width has this value, equation (4.7) becomes:

$$h_0(\varphi = \pi/2) = \lambda/2 + h \tag{4.8}$$

this means that for tall structures $(h \gg \lambda/2)$ we get $h_0 \to h$. We therefore expect that, for a structure width of 0.64λ, above a certain height $(h \sim 0.5\lambda)$ the energy absorption percentage reaches a maximum value and does not change further. This simple model provides a clear picture on how the engineering of the triangular structures can be used

to control the electron trajectories and maximize the energy they deliver to the target.

Figure 4.4 depicts the energy and motion of an electron under equations (4.2) and (4.3) and shows that the structure shape can be manipulated to obtain maximum absorption from the electrons moving from the tip of one triangle across the vacuum gap. Figure 4.4 a) shows that there is a maximum energy, reached periodically for certain positions that would correspond to the phase $\varphi = (2N + 1)\pi/2$, where N is an integer. Figures 4.4 b)-c) show, for two different structures (height and width), the trajectory of an electron moving in the vacuum gap, colored according to its energy. It can be observed that the shape of the structure influences the energy that the electron has at the recollision time. The energy is lower in figure 4.4 b) than in 4.4 c).

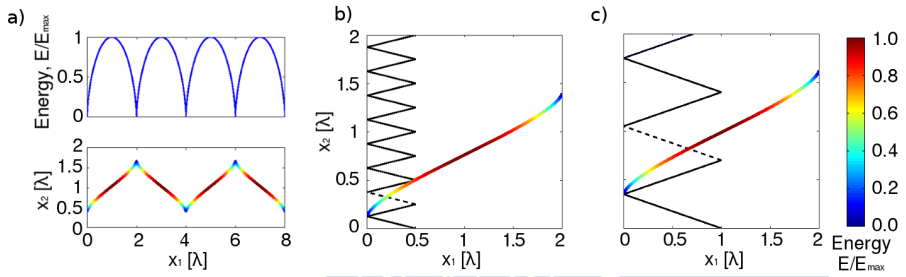

Figure 4.4: a) Energy of one electron versus the longitudinal coordinate x_1 and its trajectory. The trajectory is colored according to its energy. Electron trajectories within the vacuum gaps colored according to their energy for different structure heights and widths: b) $h = 0.5\lambda$ and $w = 0.25\lambda$, and c) $h = \lambda$ and $w = 0.7\lambda$. The dotted line represents the surface where the electron reenters the target. All panels are for a dimensionless vector potential of $a_0 = 4$.

The energy that the electron carries when it reenters the target is closely related to the laser energy absorption percentage. If we assume that the absorption percentage is given by the percentage of the maximum energy that the electron carries at reentry, it is possible to calculate which would be the absorption percentage for a specific nanostructure. The previous equations, assumed that the electron moved from one triangle to the next, and in this way it was possible to make an estimation on the optimal structure for energy absorption, however following the logic of our model, two situations can occur: one in which the electron recollides

at the next triangle and other when it recollides at the very same triangle from where it departs. The relation between the initial height in the triangle surface and the phase at reentry, previously shown in equation (4.7), is modified taking into account the case when the electron arrives to the next triangle ($\Delta x_1 \geq w/2$ when $\Delta x_2 = h$) and by the case when the electron reenters the plasma at the same triangle ($\Delta x_1 < w/2$ when $\Delta x_2 = h$). These new equations would be, respectively:

$$h_0 = \frac{\Delta x_1}{2} + \frac{h}{w}\Delta x_2 \tag{4.9}$$

$$\Delta x_1 = \Delta x_2 \frac{2h}{w} \tag{4.10}$$

The two previous equations allow us to obtain curves for the predicted energy absorption for different structure dimensions. Figure 4.5 shows an example of these curves for different structures. It is possible to observe that the results match the predictions previously described. In figure 4.5 a) it can be seen that there is an optimal width for energy absorption, that approaches $w = 0.64\lambda$ as the height grows beyond 0.5λ. The absorption reaches a saturation regime, as shown in figure 4.5 b), when the structure height is above a certain value, with nearly 100% absorption if the width is near $w = 0.64\lambda$, being at this width when the maximum absorption is reached for the minimum necessary height. It can be also observed in figure 4.5 b), that for widths below the optimal case, the absorption does not reach the maximum possible value, and for widths above it the saturation regime disappears as the height grows.

A couple of clarifications have to be mentioned in relation with figure 4.5. The peaks observed in both panels where there is an abrupt change in the absorption trend represent the transition from the case where the electron recollides with the next triangle to the case where it recollides with its departure triangle. It is also important to note that when the height or width is zero or when the width is much bigger than the height, the structure surface approaches the flat shape and the absorption becomes zero, which is not the case in reality. Therefore in order to compare these curves with the simulation data, a base absorption percentage would have to be added to the final result. Finally, this is

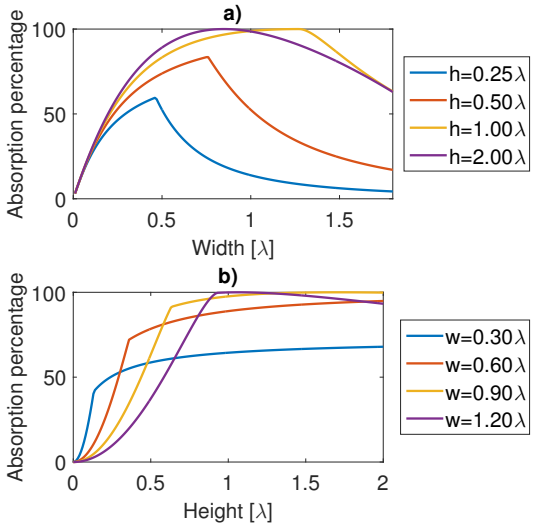

Figure 4.5: Absorption curves obtained from the model equations for different structures versus the a) width for different heights and b) height for different widths.

a simple model, and in reality there will be other energy absorption mechanisms present; there will also be a spread on the energy of each electron due to their different initial positions and, after some laser cycles, the plasma structure would be distorted from its original shape. Therefore it is expected that there will be a slight disagreement between the simulations and the model.

The predictions obtained from the model for the dependence of the energy absorption with the structure height and width can be tested by performing PIC simulations. In the following sections we discuss the results obtained from such simulations, with the aim of designing an optimal target for enhancing the energy absorption and proton acceleration.

4.2.2 Effect of the structure dimensions on the energy absorption and proton energy

The aim of this subsection is to identify, via PIC simulations, a parameter range with maximum transfer of laser energy to the accelerated protons. To address how the shape of the structures affects the absorption

of laser energy as well as the energies of the electrons and protons, we present a numerical study encompassing a wide range of sizes for two types of structures indicated in figure 4.6. We vary their width and height and use a laser pulse at normal incidence.

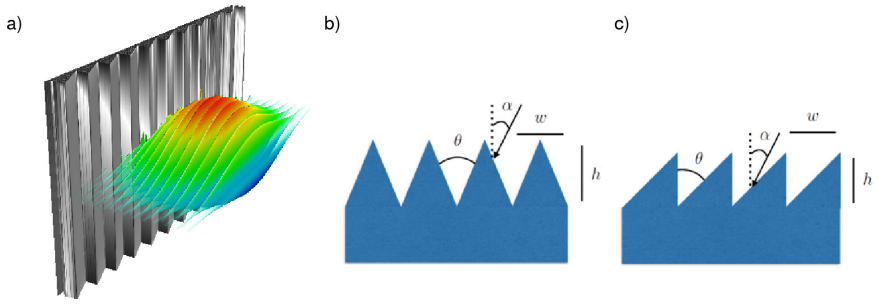

Figure 4.6: Shapes of the triangular structures. a) 3D image of the simulation setup and b)-c) detailed view of the 2D targets. The variable h represents structure height, w the width, θ the angle formed between two neighbouring structures and α the angle of incidence towards the target, defined with respect to the flat surface.

Two different targets with triangular structures were used in this work, as shown in figure 4.6. The asymmetry presented in figure 4.6 c) ("tilted triangles") with respect to figure 4.6 b) ("regular triangles") is interesting from the experimental point of view, where oblique incident laser pulses are usually used.

The targets are made of electrons and protons with a number density of $n = 40n_c$. All the targets have a bulk thickness of 0.5λ, where λ is the wavelength of the laser, and the number of particles per cell is 16 per species. The density has a steep profile as we consider a high contrast laser ($> 10^{10}$ at 5 ps) which corresponds to the STELA laser. The simulation box has a width and length of 47.9λ and 21.1λ, respectively. The spatial resolution is $\delta = 0.02$ in simulation units, that is 0.0032λ, in both axes.

The laser pulse is focused on the target surface. This pulse is launched from the left wall of the simulation box, located at a distance of 11.1λ from the target. The laser has an intensity of 3.45×10^{19} W/cm^2, a FWHM of 25 fs (with a sin^2 temporal profile), a wavelength of $\lambda = 800$ nm and a gaussian spot diameter in the focal plane of 6 μm. The

laser pulse is linearly polarized in the simulation plane, such that it is always P-polarized in relation to the structures.

The reflected energy, as well as the electron properties at the rear surface, are measured right after the interaction finishes, at the time $t = 70.2$ fs. The proton properties are measured at $t = 172.3$ fs, the time at which electrons that generate the accelerating field start leaving the simulation box. The reflected energy is measured by integrating the reflected field energy density. We have also monitored the electron and proton kinetic energy, as well as the energy of the self-consistent fields generated around the target. The energy conservation has been verified throughout all the simulations. The electron temperature at the rear surface is obtained by fitting the electron spectrum to a Maxwell-Jüttner distribution. The simulation setup is designed to scan the parameter space and to compare the relative gain between the flat and structured targets.

Several cases from low to almost complete laser absorption are illustrated in figure 4.7. Figure 4.7 a) shows the incident laser pulse and figures 4.7 b)-e) display the reflected fields. The lowest absorption is obtained for a flat target. The results obtained for different structured targets are displayed in figures 4.7 c)-e). We observe that the reflected spatial distribution of light when structured targets are used carries the imprint of the nanostructures at the target surface, and that there is an enhancement of the absorption of laser energy.

To verify the predictions of the analytical model described earlier, we perform a first set of simulations varying the width of the structure for a fixed structure height of $h = \lambda$. According to our analysis for $h \gg 0.5\lambda$ we should expect maximum energy absorption at a width of $w = 0.64\lambda$. Figure 4.8 a) shows the energy absorption, as a function of the structure width, for regular and tilted triangular nanostructures. In both cases the energy absorption increases with the width of the triangles up to a maximum nanostructure width around 0.7λ. Above this value the energy absorption decreases smoothly as the triangle width increases. For the triangles $0.6\lambda - \lambda$ wide, we obtain that the energy absorption is above 90%. This is consistent with the findings from our model in figure 4.5 a). The electron temperature rises with the width of the triangles for

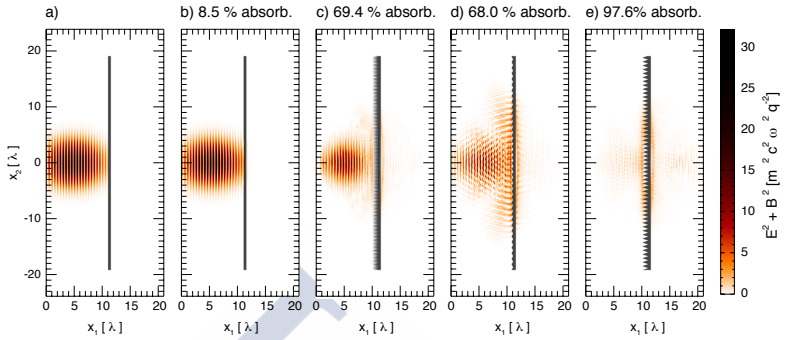

Figure 4.7: a) Incident and b)-e) reflected electromagnetic energy density for different structured targets. The reflected field is shown for a b) flat target and targets with a structure height and width of: c) $h = \lambda$ and $w = 0.25\lambda$, d) $h = 0.25\lambda$ and $w = \lambda$ and e) $h = \lambda$ and $w = 0.7\lambda$.

both types of structures and once the width of the triangles achieves a value close to 0.7λ the slope of the curve changes to a lower value, as shown in figure 4.8 b). The gain in proton cutoff energy is shown in figure 4.8 c). It exhibits a similar trend as the energy absorption.

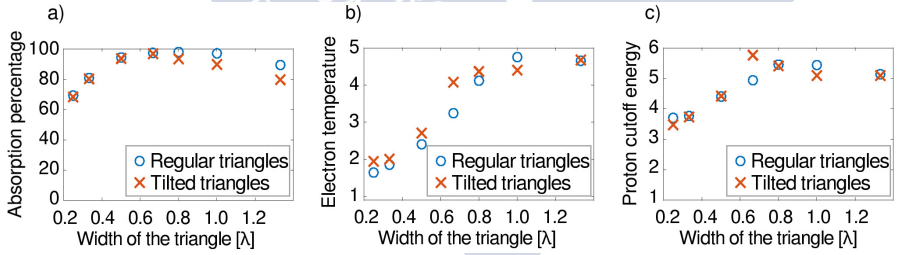

Figure 4.8: a) Laser energy absorption percentage, b) electron temperature and c) proton cutoff energy as a function of the structure width. The height of the structures is $h = \lambda$. The electron temperature and proton energy are normalized to the values obtained for a flat target.

The plots in figure 4.8 show that the the structure width can be optimized to yield a maximum laser absorption and proton energy cutoff. The structure width of the optimal target is consistent with the predictions from the theoretical model.

A second set of simulations is performed with a fixed structure

width of $w = 0.7\lambda$ and varying the structure height. We kept the rest of simulation parameters equal to the ones in the previous case. Here we should expect nearly a complete laser energy absorption above a certain threshold structure height. Figure 4.9 displays the energy absorption, the relative electron temperature and proton cutoff energy versus the height of the structures. The energy absorption percentage is shown in figure 4.9 a), that depicts an increase of the absorption of energy as the height of the triangles becomes bigger, up to a maximum value, close to 100%. This is consistent with the findings from our model in figure 4.5 b). Once this maximum is achieved, it remains unchanged as we increase the height of the triangles. The electron temperature, in figure 4.9 b), shows a big increase when the structures are added, followed by a smooth decay/stabilization for higher structures. Figure 4.9 c) displays the relative proton cutoff energy.

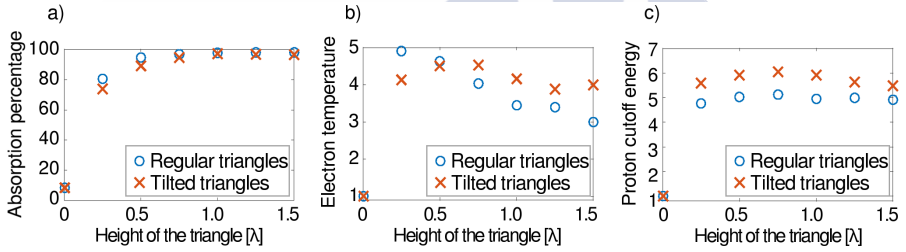

Figure 4.9: a) Laser energy absorption percentage, b) electron temperature and c) proton cutoff energy as a function of a structure height. The width of the structures is $w = 0.7\lambda$. The electron temperature and proton energy are normalized to the values obtained for a flat target.

For $h > 0.5\lambda$, the results in figure 4.9 show that the absorption percentage is above 90% and there is a 5-fold increase in the proton cutoff energy compared with the flat target. The high absorption percentages shown in figure 4.9 a) are due to the choice of a structure width of 0.7λ, close to the optimal value found before. As predicted by the analytical model, above the threshold structure height, the laser energy absorption is nearly 100% and there is no significant difference observed in the spectrum of generated protons.

For the sake of completeness, figure 4.10 compares the absorption percentages for the regular triangles against the curves predicted from

our model, including in these curves the absorption for a flat target case as a constant factor added to the absorption theoretical curve. It can be observed a good agreement between the simulation data and the model curve for some regions of the data, with a substantial discrepancy at low heights and high widths, which suggests that when the electron recollides at the same triangle from where it departs, other absorption mechanisms will be taking place.

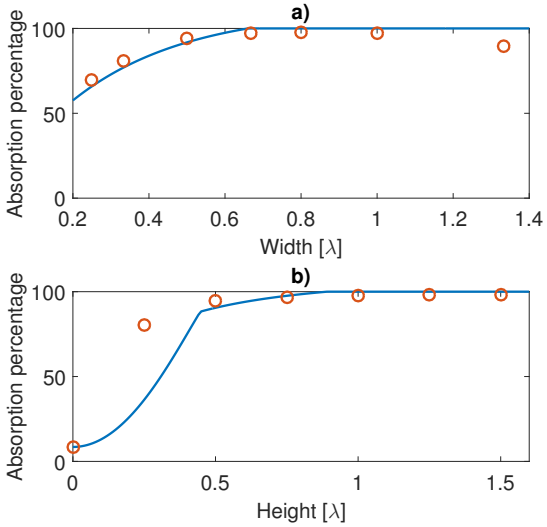

Figure 4.10: Comparison between the absorption percentage obtained from the simulations (circles) and the curve predicted by the model (solid line) for a) different structure widths and a fixed height of $h = \lambda$ and b) different structure heights and a fixed width of $w = 0.7\lambda$.

Figures 4.8 and 4.9 demonstrate that there is a correspondence between the trend followed by the laser absorption and the cutoff energy of the protons. This is not surprising, because in TNSA the absorbed laser energy is carried by the electrons towards the rear side of the target. These electrons escape the target and create a longitudinal field proportional to the square root of the electron temperature and to the electron front number density [76]. This longitudinal field is responsible for the acceleration of protons. We therefore expect higher proton energies for higher achieved electron temperatures at the rear surface. However,

additional height in the structures changes the effective target thickness and hence the electron front number density is also modified. The consequence is that the electrons with a lower temperature (e. g. for $h = 1.5\lambda$ in figure 4.9 b)) can, in principle, generate the accelerating field of the same magnitude as the electrons with a 53% higher temperature in a case with a different effective target thickness (e. g. for $h = 0.5\lambda$ in figure 4.9 b). We therefore obtain similar values for the accelerating field and for the proton cutoff energy in all cases where $h > 0.5\lambda$.

4.2.3 Oblique laser incidence

In the previous subsections it has been discussed how the energy absorption and the particle properties change with the front structure shape of the solid target. All the previous simulations have been performed with a pulse in normal incidence, however experiments of TNSA proton acceleration are typically done in oblique incidence. The main reason for using oblique incidence is to avoid the damage on the optical elements used to transport the beam to the target, with the particles ejected by the target or the back reflection of the laser pulse.

The angle of incidence of the laser pulse is expected to affect the laser energy absorption and the particle energies. We have performed simulations at different angles of incidence using targets with $w = \lambda$ and $h = 1.2\lambda$, for regular and $w = \lambda$ and $h = \lambda$ for tilted triangles. These values are chosen in the range of values that yield to the highest absorption percentages, and in such a way that the triangle angle would be the same for both, in order to be able to compare the results.

Figure 4.11 displays a) the energy absorption, b) the electron temperature and c) the proton cutoff energy at oblique laser incidence. Figure 4.11 a) shows that for the regular triangular structure, the maximum absorption and particle energies occur at normal incidence, while for the tilted structures this maximum is shifted by a value close to 22.5^o. The electron temperature for the tilted structures, in 4.11 b), displays two maxima at the angles $\pm 22.5^o$, while the proton cutoff energy for the same structure, in 4.11 c), shows a plateau around the zero angle slightly maximized for the maximum energy absorption angle.

The peak observed for the electron temperature at $\alpha = -22.5^o$

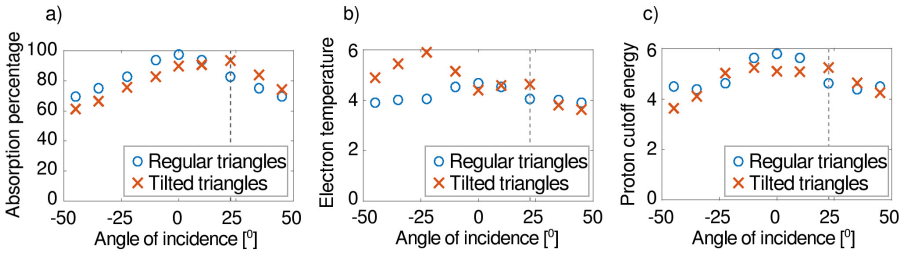

Figure 4.11: a) Laser energy absorption percentage, b) electron temperature and c) proton cutoff energy. The grey dotted line indicates the angle of incidence $\alpha = 22.5^o$, where the maximum energy absorption for the tilted structure occurs. The width and height of the structures are $w = \lambda$ and $h = \lambda$ for the tilted triangular structure and $h = 1.2\lambda$ for the regular triangular structure. The values are normalized to the results obtained for a flat target and a normally incident laser pulse.

represents electrons that get heated efficiently but do not contribute to enhance the energy of TNSA protons. This behavior suggests that a surface plasma wave (SPW) [238, 248, 250–254] is being excited at this angle, such that the electrons escape the target tangentially. This is confirmed by measuring the longitudinal accelerating field in the rear surface of the target, which shows the same trend as the proton cutoff energy in figure 4.11 c).

The analysis of the effect of oblique incident pulses shows that the asymmetric tilted triangles yield to a higher absorption percentage and more energetic protons at oblique incidence compared to normal incidence. The angle of optimal absorption for the tilted triangular structure coincides with the half of the triangle angle ($\theta = \tan^{-1}(w/h) = 45°$), and the same happens for the regular triangles, where the optimal absorption is obtained at normal incidence. This suggests that the absorption is optimal when the laser pulse is directed towards the axis for which the structure is most symmetric.

We have performed an additional simulation combining an oblique incident laser pulse with an optimized height and width of the structure $h = \lambda$ and $w = 0.7\lambda$. The bulk target thickness is 2λ and the angle of incidence of the laser is $\alpha = 17.5^o$, which is half of the triangle angle in this case ($\theta = \tan^{-1}(0.7) = 35°$).

The comparison between the results obtained with the same setup for a target with a flat surface and the structured target show a 15-fold

increase in the energy absorption percentage, from a 6.1% in the flat target to a 90.6% in the structured target. This enhancement of the energy absorption generates protons with energies between 4 and 5 times higher compared with the case in which a flat solid target was used. This is verified in figure 4.12 that shows a) the proton energy spectrum and the momentum space $p_1 - p_2$ of the protons. Both, the cutoff energy and the temperature of the protons increase by a factor between 4 and 5 when one uses a structured target in place of a flat one.

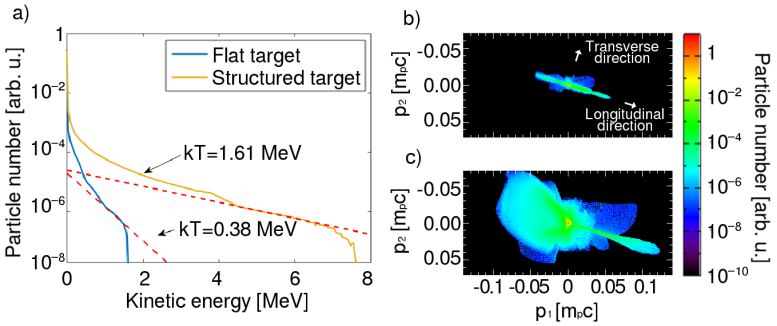

Figure 4.12: a) Proton spectrum and the p1-p2 momentum space for b) a flat and c) a structured target.

The result shown in figure 4.12 demonstrates, in an experimentally feasible setup, that the use of surface nanostructured triangular targets for TNSA acceleration can increase substantially the energy of the accelerated protons.

4.2.4 Robustness of the results for typical deviations from ideality

Most of the numerical studies of TNSA proton acceleration using nanostructured targets that have been published and all the simulations performed before, assume an ideal situation, where the laser peak intensity is fixed, the nanostructures are perfectly regular and there is no pre-plasma. Although that leads to valid results, it is interesting to address the effect of possible deviations from the ideal situation, that are regularly present in real scenarios.

Following the results previously shown, we have performed for

the regular triangle shape, a study about the effect on the laser energy absorption of some of the deviations from the ideal situation that can be expected in a laboratory, with the final purpose of giving a realistic motivation for the suitability of these targets to be implemented experimentally.

In our simulation setup, the target composition and dimensions are the same as the ones used in the parametric study of the previous subsection, with a number of particles per cell of 25 per species. The simulations are ran in slab geometry, with open boundary conditions in the longitudinal limits of the simulation box and periodic boundary conditions in the transverse dimensions. The simulation box has a width and length of 7λ and 25.5λ, respectively. The spatial and temporal resolution are unchanged with respect to the previous simulations.

The laser pulse has the same amplitude, wavelength and polarization as before. It is initialized inside the simulation box, with its front at a distance of 0.6λ to the target, with a total width of 7λ (with a polynomial temporal profile, with a rise and fall curves of length λ), and a plane wave transverse profile.

When considering deviations from the ideal situation, typically assumed in numerical studies, there are several parameters to take into account. Here we have decided to focus in what we think can be the most common sources of deviation: the use of different ion species, a variation on the peak intensity of the laser pulse, the existence of a pre-plasma region and a non-perfect periodicity of the nanostructures.

4.2.4.1 Different ion species

For most of the results shown in this chapter, we have used hydrogenoid targets, whose results in the energy of the accelerated particles must differ from a realistic situation, at least in absolute terms. In the typical TNSA picture the accelerated protons come from a thin layer at the target rear surface, formed due to atmospheric hydrogen, although ions from the bulk can be also accelerated if that layer is removed [73–75]. Typical inexpensive metallic foils, that can be used in these experiments, are formed of a mixture of elements that usually come as derivatives of the fabrication process, where the main element appears in a higher

concentration, therefore it is relevant to address the effect of the ion species on the laser energy absorption.

As it was previously stated, the energy absorption in nanostructured targets is controlled by the electron motion within the structure vacuum gaps, therefore it should not be affected by the ion species. Table 4.1 demonstrates this, showing that for three different kind of targets composed of electrons and different ions and with different plasma densities, the laser energy absorption remains the same, with a slight deviation for hydrogenoid targets, due to the much lower mass of protons compared to heavy ions, however the difference is always below 2%. Furthermore, the table proves that as the density of the plasma becomes higher ($n \gg 1$), the difference in the absorption percentage becomes irrelevant.

Table 4.1: Absorption percentages for plasmas composed of electrons and different ion species at different densities. These results are for a triangular target with height and width of $h = \lambda$ and $w = 0.7\lambda$, respectively.

Ion species $\rightarrow$ Density $\downarrow$	Hydrogen ($Z = 1$)	Aluminum ($Z = 13$)	Copper ($Z = 29$)
$40n_c$	94.8%	96.9%	96.9%
$80n_c$	96.1%	97.0%	97.1%
$120n_c$	95.9%	96.7%	96.8%

4.2.4.2 Variations on the laser intensity

The variation of the peak intensity of the laser pulse is also an important deviation to take into account. In the considered optimal target design of height and width $h = \lambda$ and $w = 0.7\lambda$ we can observe than a $\pm 30\%$ variation in the peak field amplitude represents a maximum $\sim 1 - 2\%$ variation in the absorption, as shown in figure 4.13. This proves that, although a higher intensity will yield to a higher proton energy, the percentage of transferred laser energy will be unchanged in the range of values addressed.

The effect of this deviation from the ideal situation is important to analyze because it is related to both fluctuations between different laser shots and defocusing effects. Experiments of TNSA proton acceleration show slight discrepancies between different shots due to these deviations [122, 255]. Although the typical deviation in a well designed setup does

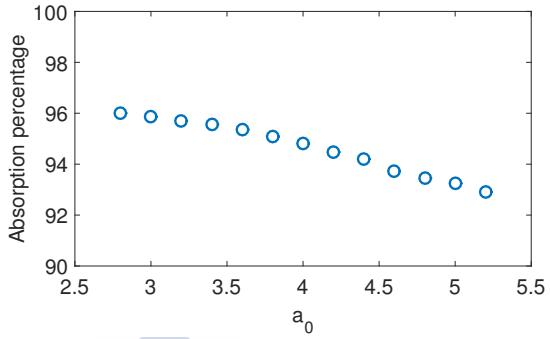

Figure 4.13: Laser energy absorption percentage for different laser intensities, sweeping a $\pm 30\%$ variation around the original peak field amplitude. The height and width of the triangles are $h = \lambda$ and $w = 0.7\lambda$, respectively.

not cause extremely different measurements, it is interesting to analyze the limiting case in which there would be big intensity fluctuations in the laser pulse. With these results it is possible to conclude that the intensity fluctuations between different laser pulses or a non-perfect focusing of the laser pulse, if small, should not affect the energy absorption.

4.2.4.3 Pre-plasma effects

Pre-plasmas are one of the most important experimental issues to take into account in laser-plasma experiments. They are created because of the expansion of the electrons and ions towards vacuum during the ionization of the target, caused by the pre-pulse of the laser pulse or by its front pedestal. This expansion generates a region of density growth, from zero to the plasma bulk density, that the main part of the laser pulse interacts with. The availability of lower density regions for the pulse to interact with, in comparison with the case of a steep density profile, changes the laser-plasma dynamics at the target surface. We have assumed the existence of an exponential pre-plasma profile [195, 256–261] at the target front surface and studied its effect on the laser energy absorption for different lengths. The equation that describes the density profile is given by:

$$n = n_0 \left[e^{\log(2)\frac{x-(x_0-L)}{L}} - 1 \right] \quad (x \in [x_0 - L,\ x_0]) \tag{4.11}$$

where n_0 is the plasma bulk density and x and x_0 are the spatial coordinate and the coordinate origin, respectively. The parameter L determines the length of the pre-plasma, named as scale-length.

TNSA particle acceleration using flat targets is strongly affected by the existence of a pre-plasma [228, 258], however in the case of structured targets there are still only a few studies addressing its effect [124, 239, 242]. These studies have found that in order to obtain the high laser energy absorption achieved with nanostructures and the enhanced proton energy, the contrast of the laser pulse must be very high, to avoid the existence of a long pre-plasma that would destroy the structures before the arrival of the main laser pulse.

Figure 4.14 shows how a short pre-plasma affects the laser energy absorption in different triangular nanostructured targets. For the optimized structure with height and width of $h = \lambda$ and $w = 0.7\lambda$ the effect is very small, finding only a $\sim 6\%$ decrease in the absorption for a pre-plasma with a scale-length of 0.5λ. If the structure dimensions differ from the optimal, and specially as they become smaller, the effect of the pre-plasma can be very important, as seen for a structure of height and width of $h = 0.2\lambda$ and $w = 0.35\lambda$, where a $\sim 20\%$ decrease in absorption is found.

For the optimal target design, pre-plasmas as long as 0.5λ do not affect strongly the energy absorption. Taking as a reference the expansion of pre-plasmas in flat targets [262, 263] and assuming that in these structured targets the expansion will be similar, we can conclude that a laser pulse with an ASE contrast higher than $\sim 10^{10}$, and a pre-pulse with a peak intensity not higher than $\sim 10^{16}$ Wcm^{-2} at a distance shorter than ~ 5 ps would be needed to have a pre-plasma shorter than $\sim 0.2\lambda$, below which its effects are not dramatic as we observe in figure 4.14. Therefore we confirm that in order to preserve the enhanced absorption of these structured targets, specially for a non-optimal design, very high contrast pulses are needed.

In studies using nanospheres, it has been reported that a very short

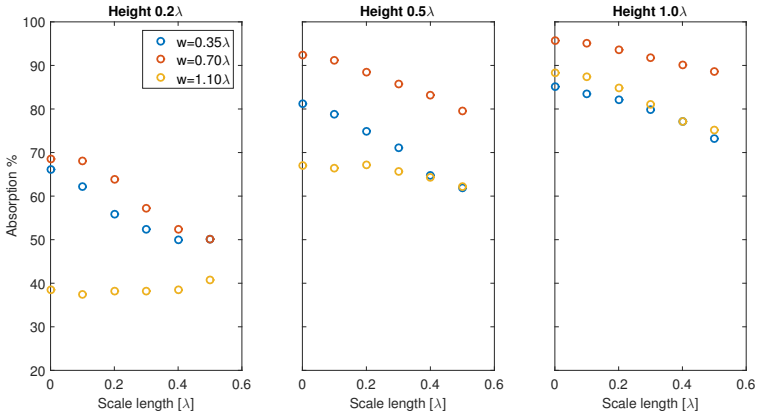

Figure 4.14: Effect of the pre-plasma in the absorption percentage. Targets with smaller features experience a bigger decrease with higher pre-plasmas.

preplasma of length 0.04λ changes the absorption percentage by 5% [123]. In references [239, 240, 242], the effect of pre-plasma on nanostructured targets is also discussed, concluding that a low contrast and hence a long pre-plasma region would destroy the structures before the main pulse arrives. Therefore the conclusions achieved in this section regarding pre-plasma effects could be extended to other kinds of nanostructures.

4.2.4.4 Non-periodical structures

The last issue considered in this study is the possible non-periodicity of the nanostructures. This is a very important situation to analyze, as it will set a requirement for the need of a very precise fabrication technique or not, and therefore of the fabrication costs for these targets.

The fabrication of surface periodic nanostructured targets is a timely topic for several applications that can be achieved by several methods (or a combination of them), such as laser direct writing [264, 265], lithographic methods [266–269] or chemical etching [269, 270], among others. The precision, velocity and costs of fabrication vary substantially depending on the chosen fabrication method and the materials employed. The state of the art of these techniques allows the fabrication of the

targets studied here with high precision, however it is interesting to address what would happen if there were fabrication errors, as it may happen with cheaper and less precise fabrication setups.

To analyze the impact of irregularities in the structure periodicity, we have performed simulations and analytical calculations with our model in several situations in which we randomize the height and width of each triangle in the structure. The randomization is controlled by a maximum variation percentage, that sets the percentage of the ideal height or width that we allow to be varied in the limiting case, for example with a maximum variation percentage of 50% and for a structure height of h, a randomized triangle would have a random height in the interval $[0.5h,\ 1.5h]$. Figure 4.15 illustrates this with an example of two structures whose width and height have been randomized.

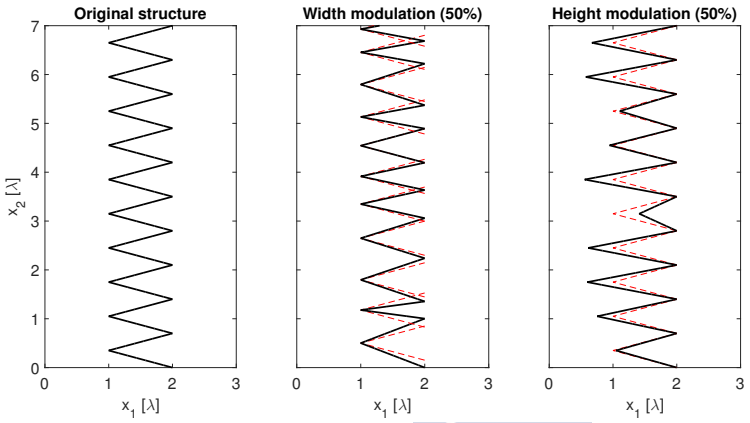

Figure 4.15: Original structure with height and width of $h = \lambda$ and $w = 0.7\lambda$ and examples of two structured targets whose width and height have been randomized with a maximum modulation percentage of 50%. The dotted lines indicate the shape of the triangles with the original dimensions, centered in the same positions as the modulated triangles.

Analytical results are obtained from expanding our previous model, where the equations can be tailored in order to address for these situations. In the case that contiguous triangles have different heights and widths, equation (4.10) would remain the same, however equation (4.9) would be rewritten as:

$$h_0 = \frac{h_A w_B}{h_B w_A} \frac{1}{\frac{h_A w_B}{h_B w_A} + 1} \left[\Delta x_1 + \frac{2h_A}{w_A} \Delta x_2 \right] \tag{4.12}$$

where indexes A and B indicate the departure and arrival triangle, respectively. It is straightforward to verify that if $h_A = h_B = h$ and $w_A = w_B = w$, equation 4.9 is recovered.

Figure 4.16 shows the results obtained with the analytical model taking as reference the optimized structure with dimensions $h = \lambda$ and $w = 0.7\lambda$. For each maximum variation percentage, 200 random structures have been generated and their absorption percentage computed. These individual results can be grouped to generate a probability density, that states the probability for obtaining an specific absorption percentage with a maximum fabrication error given by the maximum variation percentage.

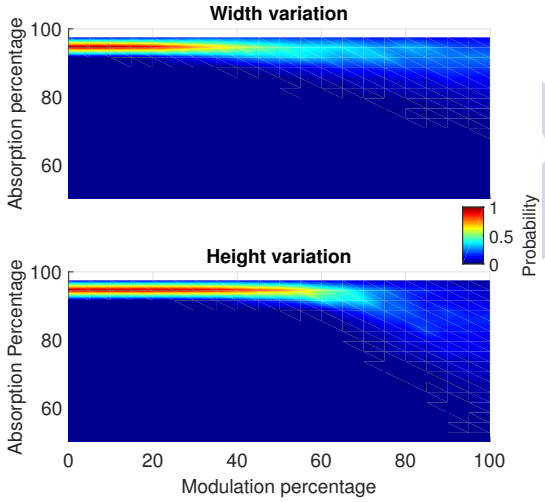

Figure 4.16: Results of the analytical calculations for randomized structures. The panels show the probability of obtaining an specific absorption percentage for a given maximum variation percentage. The results are obtained by performing calculations with the model equations, considering that the structure shape is randomized.

Simulation results are shown in figure 4.17, compared with the analytically predicted average and 3σ intervals, obtained from the probability density in figure 4.16. The agreement between the simulation

data and the model predictions is very good, furthermore the fact that simulation data falls into the 3σ intervals predicted by the model gives further support for this agreement.

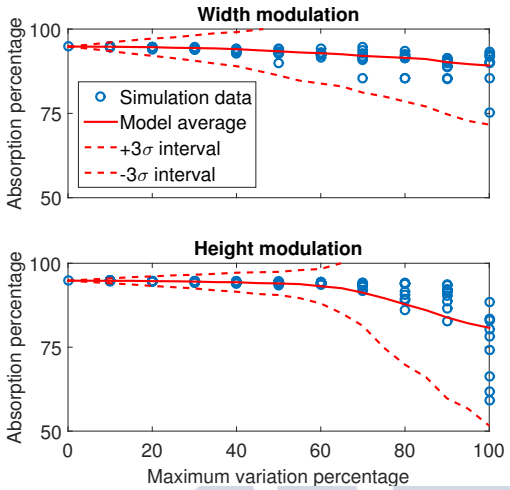

Figure 4.17: Energy absorption percentage obtained with PIC results for different maximum variation percentages for the height and width of the triangles, along with the average and 3σ intervals predicted by the analytical model.

The results in figure 4.17 prove the robustness of these targets for energy absorption in terms of the fabrication techniques, both from PIC simulations and analytical calculations. It can be observed that even with a 100% maximum variation percentage, the average decrease in the energy absorption is $\sim 30\%$ and $\sim 10\%$ for variations of the height and width, respectively. This suggests that it is possible to use cheap fabrication techniques that may not be extremely precise for these targets, thus reducing the potential cost of an experiment.

In summary, triangular nanostructured targets for TNSA are very robust in terms of changes of the laser intensity, ion species, or fabrication errors, however it has been found that the pulse contrast has to be very high, in order to avoid the existence of long pre-plasmas, especially if the target parameters are not the optimal ones. These results are a major motivation for the use of targets with a structured surface in experiments of TNSA instead of those with a flat surace.

4.2.5 Three-dimensional PIC simulations

It has been analyzed how the energy absorption varies when triangular structures are on the target surface and how this variation affects the electron heating and consequently the energies of the accelerated protons. The theoretical analysis, combined with 2D PIC simulations, shows that the structure shape can be optimized to yield high percentages of energy absorption and an enhancement on the accelerated proton energy. It has been also found that these results are robust in terms of deviations from the ideal case.

Our conclusions regarding the target structure for optimal laser absorption are general and can be extended to 3D geometry. The electron interaction with a linearly polarized electromagnetic wave in vacuum is fully described in 2D. The energy of the electrons at the point of re-entry into the target depends on the geometrical properties of the structures such as width and height and it is intrinsically a 2D problem. The optimal configuration for laser absorption is therefore likely to be the same in 2D and 3D geometry. However, even though ion acceleration can be studied qualitatively in 2D, it is well-known that the proton energy cutoff in TNSA is lower in 3D geometry [225, 226], as it has been mentioned at the beginning of this chapter.

4.2.5.1 Comparison between 2D and 3D results

It is very expensive in terms of computational resources to perform a full-scale 3D simulation, allowing to consider enough time for target expansion. However, the 3D simulations can be performed in slab geometry. In this geometry the laser is treated as a wavepacket that is transversely a plane wave and periodic transverse boundary conditions are applied both for the fields and the particles, except for the direction of laser propagation where open boundaries are used.

The simulation box is 25λ long and $3.5\lambda \times 3.5\lambda$ wide. The laser pulse is initialized inside the box with a total duration of $7T$, where $T = c/\lambda$ is the laser period, with its front at a distance of 0.5λ to the top of the structures. We performed simulations for flat targets and for the optimal structured targets presented previously ($h = \lambda$ and $w = 0.7\lambda$).

The goal is to compare the relative increase of the absorption efficiency in 2D and 3D.

The results obtained in 3D simulations, show a 91.5% of laser absorption for a structured target with regular triangles, a 89.5% for the case tilted triangles and 2% for a target with a flat surface. In the case of 2D simulations, a 95.4% of energy absorption was absorbed for the regular triangles, a 92.3% for tilted triangles, and a 2.6% for the flat target. It can be seen that the absorption estimates from 2D and 3D PIC simulations are consistent within a margin of 4%.

The electron spectra obtained from the 2D and 3D PIC simulations at the time $t = 25.5$ fs are displayed in figure 4.18 a). In order to compare the spectrum from the 2D and 3D case (since in the latter the number or particles in the simulation box is higher), the spectra are normalised to the same reference height at the energy 2 MeV. We can observe a slight difference between the tilted and regular structures, due to different electron dynamics at the target surface. The respective proton spectra at the time $t = 51.1$ fs are shown in figure 4.18 b). These spectra are normalized to the same reference height at the energy 1 MeV. As expected, the proton cutoff is lower in 3D compared to the 2D case. Apart from verifying the conclusions obtained in 2D, an additional advantage of 3D simulations is that they can provide an estimate of the total number of accelerated protons. In our case the number of protons being accelerated to an energy above 0.1MeV is approximately 1.35×10^{11}, corresponding to over ~ 21.6 nC of charge accelerated to energies up to 4 MeV.

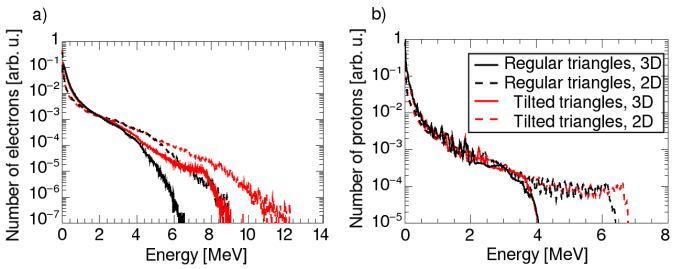

Figure 4.18: The spectrum of a) electrons and b) protons measured for the 2D and 3D setup. The height and width of the triangular structures at the target surface are $h = \lambda$ and $w = 0.7\lambda$.

4.3 DISCUSSION

TNSA proton acceleration is a multidimensional problem, with several parameters involved in the outcome of the acceleration process. There are several factors relevant to the ion acceleration we have not addressed in parts of this chapter or that could be addressed more in detail. A discussion is needed, on how our conclusions can be affected by using a different nanostructure shape or by varying the target thickness and compounds, for example.

The enhanced energy absorption can be obtained also with other structure geometries, such as rectangles [239, 240, 242] or nanospheres [123, 241]. Our model can, in principle, be extended to account for different structure geometries. As the key parameter for obtaining an optimal laser absorption is the time-of-flight of the electrons in the vacuum gap, a change in the shape of the structure directly affects their energy at the point of recollision with the target. Also, certain shapes that are not grating-like, might add different dynamics at the target surface. We therefore expect that other structures would have different absorption percentages, as the literature suggests.

The target thickness is another relevant parameter for proton acceleration. Although the thickness of the target does not affect the energy absorption (for thicknesses well beyond the plasma skin depth), since that is controlled by the nanostructures on the target front, it affects the proton acceleration, since it determines the redistribution of energy from the electrons to the protons. If we consider that there are no pre-plasmas present, our optimal structures could be added to the front surface of a target of an arbitrary thickness, and ensure that the maximum possible energy is transferred from the laser to the electrons. In the case of the existence of a pre-plasma, as the literature suggests, an optimal target thickness would exist for a given structure. In other words, assuming high contrast laser pulses, the target structure shape and the target thickness can be optimised separately to result in the most efficient proton acceleration.

The 2D parametric scan presents simulations of hydrogenoid targets, but as it has been explained, most TNSA targets in experiments are

composed of heavy ions and electrons with a thin proton contamination layer on the rear surface. The presence of different compounds changes the energy of the accelerated protons in comparison with the hydogenoid targets. However, the dynamics of the electrons near the front surface will be similar as in our hydrogen simulations, because their motion depends on the geometry of the nanostructures and the ions can be regarded as inmobile during the interaction between the plasma and the short laser pulse. We have verified that neither a higher ion mass nor a higher plasma density significantly affect the laser absorption, therefore the optimal structure for energy absorption and the absorbed energy remains unchanged.

4.4 CONCLUSIONS

The acceleration of protons in TNSA laser-plasma accelerators using thin targets with a triangular periodic nanostructured front surface has been studied. It has been found that these targets enhance substantially the transfer of energy from the laser pulse to the plasma, thus contributing to an abrupt increase of the accelerated proton energies.

We have developed an analytical model to understand why the absorption is enhanced, based on the motion of electrons across the vacuum gap between two consecutive structures, finding the dependence of the absorption percentage on the shape of the structures. Afterwards, we have performed a numerical study through 2D PIC simulations to reveal how the energy absorption and the accelerated proton kinetic energies vary with the shape of the structures and the angle of incidence of the laser. This study verified the predictions from the model and gave us the conclusion that through the right choice of the dimensions of the structures and the angle of incidence of the laser, energy absorption percentages on the order of 90% can be achieved, yielding to an increase on the proton kinetic energy between 4 and 5 times in comparison to those that can be achieved with flat targets.

The robustness of these results in terms of deviations from an ideal situation was addressed. The effect of several factors that can be found in a realistic situation, such as multiple ion populations, variations of the laser peak intensity or defects in the regularity of the nanostructures, are

found to have an effect on the absorption, which is minimal when the height and width of the structures have the values around the ones found to be optimal. On the other hand, it has been confirmed that in order to obtain high absorption percentages, high contrast laser pulses must be used, specially if the target design is not optimized.

The results shown in this chapter, along with previous results from the literature, represent a major motivation for the use of these targets in experiments and applications. They show how the energy of the accelerated protons is enhanced. It has been also proven the robustness of this acceleration method for deviations that can be found in a laboratory. The best strategy for target fabrication is to combine several different aspects of optimization in order to obtain the highest ion energies (or higher yield of ions at lower energies). Using nanostructures at the front surface presents an opportunity for an additional increase in efficiency of the laser energy absorption by the electrons, which is compatible with other types of target optimization.

USC
UNIVERSIDADE
DE SANTIAGO
DE COMPOSTELA

5 OTHER LASER-PLASMA INTERACTION APPLICATIONS

In this chapter we present results obtained when laser-plasma interactions computed with the PIC mechanism are used as a tool for the computation of other interesting phenomena. Concretely we present the results for HHG in gas targets when metallic bow-tie nanoantenna structures interact with an ultrashort laser pulse [271].

5.1 HHG IN GAS TARGETS

The generation of high harmonics in the interaction between a laser pulse and a gas target has been mentioned several times in this thesis. In this part we will give a very brief outlook about the physical principles that govern this generation and we will focus on the concept of phase matching and its importance for this mechanism, as it will be a relevant concept for the results shown in this chapter.

5.1.1 Physical principles

HHG in gas targets [8,11,272,273] is a nonlinear process that occurs when a laser pulse interacts with a gas target, typically made of a noble gas. In this case the electric field of the laser pulse interacts with neutral atoms, ionizing and moving their electrons in an oscillatory manner around the positively charged nucleus, such that this motion triggers the emission of high harmonic orders, that come in the form of attosecond pulses every half cycle, propagating with the transmitted laser pulse.

In more detail, the HHG process can be understood in terms of a simple three-step semi-classical model [274, 275]:

- The electric field interacts with the atoms, ionizing the electrons in the outer shells and pulling them away from the parent ion.
- The electron wavepacket is pulled into the continuum, until the oscillating electric field changes its sign, when it is accelerated backwards towards the starting point (the position of the parent

ion).

- Finally the electron wavepacket recollides with the parent ion, reaching a lower energy state and liberating the gained kinetic energy during the half oscillation, in the form of high harmonic orders. The recollision occurs at sub-femtosecond time scales, therefore the harmonics are emitted in the form of attosecond pulses.

The motion of the electrons in the direction of the laser field polarization can be calculated analytically and it obeys the equation:

$$x = -a_0 \left(\sin(t) - \sin(t_0) - (t - t_0)\cos(t_0)\right) \tag{5.1}$$

where x notes the separation of the electron from its starting point (the position of the parent ion), t indicates the time and t_0 the time at which the electron starts the motion. This equation is trivially obtained from the integration of the force acting upon the electron: $d^2x/dt^2 = qE_0/m\sin(\omega t) = a_0\sin(t)$. The energy at recollision can be calculated from $E_K = (dx/dt)^2/2$, and it is given by:

$$E_K = \frac{a_0^2}{2}\left(\cos(t) - \cos(t_0)\right)^2 \tag{5.2}$$

To obtain these equations it is assumed that the electrons start the motion once they have been already ionized. At this moment, their position is at $x = 0$ and they are at rest ($dx/dt|_{t_0} = 0$).

The trajectories and the corresponding energy of the electrons at the recollision point are plotted in figure 5.1. It is observed that there is an optimal trajectory for which the energy at recollision is maximum. Outside of it, we obtain two kind of trajectories, the ones where the electron arrives before the optimal case, that we will name short trajectories, and the others where it arrives after, that we will name long trajectories. The harmonic contribution from short trajectories is positively chirped (lower energies are emitted before the higher ones) and negatively chirped for long trajectories.

The main properties of the harmonic spectrum excited by this mechanism are the following [8, 11, 272, 273]: there is a plateau region in

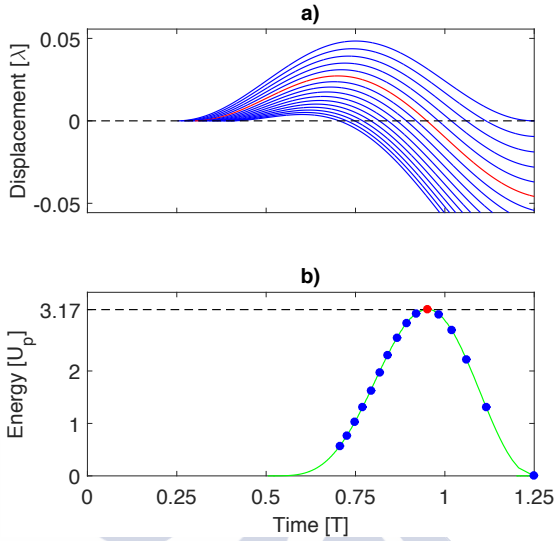

Figure 5.1: Results from the three-step model equations for the a) trajectory of the electrons and b) their energy at recollision with the atom (in units of the ponderomotive energy $U_p = a_0^2/4$). The calculations have assumed an intensity of $I = 5 \cdot 10^{16}$ Wcm^{-2} and a wavelength of $\lambda = 800$ nm. The dashed lines indicate a) the ion position and b) the maximum energy at recollision. The trajectory that leads to the maximum energy is highlighted in red.

the harmonic spectrum, which shows that this is a non-perturbative process; the spectrum has a clear cutoff after the plateau, depending on the ionization potential of the atom and the laser intensity, given by $\omega_c = I_p + 3.17U_p$, where I_p is the ionization potential of the atom and $U_p = a_0^2/4$ is the ponderomotive energy. The spectrum is made of odd harmonic orders (for a monochromatic field), since the emission of the harmonics is separated by half laser cycles with an alternating phase difference of π, coming from the different sign of the laser field in every half cycle; the emission of the high harmonic orders comes in the form of attosecond pulses; and there is an upper limit on the intensity of the laser pulse, from which the Barrier Suppression Ionization (BSI) [179–183] begins to dominate over the tunnel ionization mechanism and the field ionizes completely the atom, thus not allowing for a recollision of the electron wavepacket with the parent ion.

The previous description of HHG in gases is done at the atomic level,

it is referred as the microscopic description of HHG. In real experiments we do not observe the emission from a single atom, but from a big number of them, distributed in a macroscopic sample (gas target), therefore what is measured in an experiment is an integration of all the individual contributions of each atom, hence a macroscopic description for HHG is needed. In this case, phase matching effects represent an important factor to take into account in order to make an accurate macroscopic description.

5.1.2 Phase matching effects

The harmonic spectrum emitted from a macroscopic target is built by the addition of the contributions of each individual atom. However, in the macroscopic scenario there are several factors that can alter the harmonic emission in comparison with the picture from a single atom, and the final harmonic signal is not simply the direct sum of all individual signals from each atom as if they were all packed at the same position and under the same conditions. The atoms in the target are located at different positions, there is a refractive index inside the gas, some atoms are ionized, and the laser pulse has a focusing profile inside the target. These mentioned deviations from the ideal case add different phases and amplitudes for the emission of the harmonics at each atom, such that the final field consists on the sum of each individual emission with different phase and amplitude. The final signal then depends strongly on the different added phases to the field emitted by each individual atom. The effects of all these phases into the final harmonic spectrum is defined as phase matching effects [276–278]. This definition allows us to introduce the phase mismatch $\Delta\vec{k}_n$ as the difference in the propagation between the original laser propagation and the one from the nth harmonic, that is: $\Delta\vec{k}_n \equiv \vec{k}_n - n\vec{k}_1$.

A very simple example of phase matching effects can be done with a geometrical argument: at the macroscopic scale, part of the atoms in the sample will feel the laser field before others, due to their different locations, therefore the emission of the harmonic spectrum will occur at different times for each atom, which translates into the addition of a phase between the different signals. Figure 5.2 illustrates this example.

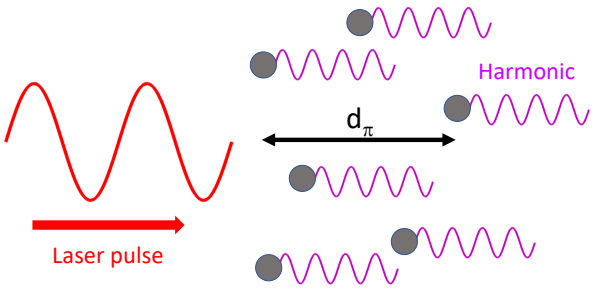

Figure 5.2: Example of a phase matching effect from a geometrical source: a laser impinges onto a sample of atoms and they emit the same harmonic field. The atoms separated by a distance d_π emit with a relative phase of an odd multiple of π , thus their signals interact destructively and they do not contribute to the macroscopic signal.

It is possible to define a coherence length for the n^{th} harmonic as the minimum distance between two atoms that emit out of phase ($d_c = \pi/\Delta k_n$). In general the coherence length for a harmonic order is defined in the same way, but taking into account that there are several sources responsible for the phase mismatch.

The most common sources responsible for phase matching effects are: the geometry of the source, due to the different positions of the atoms; the relative position between the source and the detector, as the optical path followed by the radiation from the atoms to the detector vary with respect to the angle where this detector is placed; the refractive index from bounded and free charges, as it affects the local wave vector of the laser pulse; and the intrinsic phase, which is a phase depending on the excursion time of the electron in the continuum and on the local intensity profile of the electric field, that is the phase mismatch from the different trajectories. The phase mismatch arising from the intrinsic phase is then higher for long trajectories. Long trajectories are more affected by phase matching effects if only one source of phase mismatch is present, since the electrons responsible for them spend more time in the continuum, however in the most general case this is not necessarily true, since the final phase mismatch is obtained from the combination of all the mismatch sources present in the experiment.

The importance of these effects is very high, as it determines mostly

the shape of the harmonic spectrum and its associated attosecond pulses. Phase matching can be tailored in order to enhance some of the properties of HHG, and it has been proven as a successful tool to boost the cutoff energy into the X-ray region [279], to isolate attosecond pulses [280, 281], to tune the polarization of the attosecond pulses and even produce circular polarization [282, 283] or to generate vortex beams with the high harmonic orders [284, 285].

In conclusion, phase matching is a concept arising from the macroscopic description of HHG and it is a relevant factor to take into account when high harmonics are emitted from gas targets. It can be both detrimental or beneficial for different properties of the harmonic spectrum, and therefore a high knowledge and control over it is important in order to achieve the desired results.

5.2 PLASMON OSCILLATIONS

In this section we will introduce shortly the concept of plasmon oscillation, and we will use the interaction of a laser-pulse with a subwavelength slit aperture on a plasma to exemplify it, as it will be relevant for the results presented after.

5.2.1 General description

In general, a plasmon is defined as a quantum of plasma oscillation, that is their quantization, analogously as the definition of phonons to quantify the energy in crystal lattices for solid state physics or photons to do so with electromagnetism. When a P-polarized electromagnetic wave goes from a dielectric material towards the separation surface with another material at an angle of incidence $\theta \neq 0$ and is reflected (i.e. when the material is a dielectric and the angle is above the critical angle, or when the material is a metal, or when the material is an overdense plasma), there is a component of the field during the reflection pointing parallel to the normal direction to the surface. This field component causes the motion of the electrons at the surface, generating a surface wave named surface plasmon oscillation/polariton that propagates tangentially to the surface [286]. The response of the electrons to this wave can be modeled and it is found that the collective response of the

electrons is resonant at a specific frequency named the "resonance frequency". In the case of a plasma the resonance peak occurs for radiation at the plasma frequency ω_p, since the electric permittivity would be zero in that case ($\varepsilon = \varepsilon_0(1 - \omega_p^2/\omega^2)$).

Plasmon resonances occur when the motion of the electrons at the surface have a collective response that triggers a local amplification of the plasmon polariton wave. This phenomenon has been extensively analyzed, as it can be used for an enormous amount of applications, such as in sub-wavelength optics, near-field optics, chemistry at the nanoscale, enhancement of energy absorption or biological applications (see [287, 288] and references therein).

In conclusion, plasmon oscillations are field oscillations at the surface of a material caused by the motion due to an electromagnetic wave of bounded or free electrons over an ion background, that propagate tangentially to the surface, and that can be amplified substantially if the resonance requirements are met.

5.2.2 Case with a sub-wavelength slit

The excitation of these longitudinal oscillations at the surface only occurs when an electromagnetic wave, P-polarized, arrives obliquely to the target. In this situation, part of the field oscillates in the normal direction to the surface during its reflection. The normal field component at the surface is maximized when the laser pulse impinges tangentially to the surface, thus generating a higher charge separation on it. Therefore, if one uses two parallel targets very near to each other ($< \lambda$), such that the laser pulse impinges into the separation gap between them, the charge separation at each of the surfaces will create a sub-wavelength capacitor, that may enhance the field inside the gap. This situation is depicted in figure 5.3.

To produce the plasmon oscillations, it is necessary that the field penetrates into the material at the sub-wavelength gap; hence the thickness of the target should be thin enough to allow the transmission of energy through it. For a plasma this means that the thickness has to be on the order of the skin depth $\delta = c/\omega_p$. Furthermore, the field strength should be well below the relativistic limit ($a_0 \ll 1$), in order to avoid the

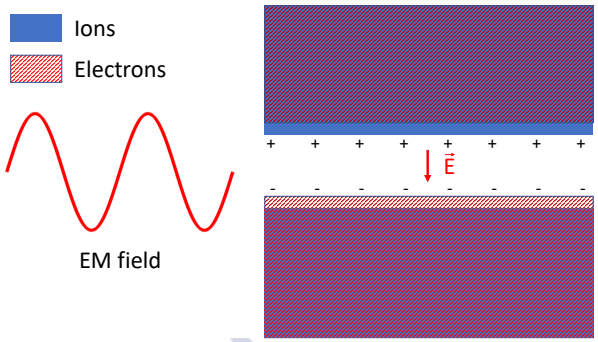

Figure 5.3: Scheme of the described sub-wavelength capacitor. The laser pulse impinges into the gap between the two targets and moves the electrons at the surface, generating two plane-parallel charged surfaces with opposite charge. A field is created inside the gap, and its charge oscillates following the electromagnetic field oscillations.

destruction of the target during the interaction and filling the gap with a high density of electrons.

To evaluate the feasibility of this proposed setup we have performed 2D PIC simulations, in which a laser pulse impinges normally on a very thin target ($\ll \lambda$) with a sub-wavelength aperture at its center. We analyze the field generated inside the gap, as well as the electron motion at the surface. Simulations have been performed with a numerical and temporal resolution of $2 \cdot 10^{-3}$ and 10^{-3} (in simulation units), respectively. The simulation box has the dimensions $6\lambda \times 3\lambda$ (longitudinal $\times$ transversal), with periodic boundary conditions in the transverse dimension and absorbing conditions in the longitudinal dimension. A laser pulse with an intensity of 10^{12} Wcm^{-2} and polarized in the simulation plane is initialized into the simulation box, with a plane transverse profile and a $\sin^2$ longitudinal profile of total width $W = 5\lambda$. We assume that the target is made on gold ions ionized once, that is, gold ions and electrons with a plasma density of $n = 35n_c$ and with a steep density profile. The number of particle per cell is 16. The aperture at the target center has a width of 0.025λ and the thickness of the target is 0.05λ. The simulation runs until the time $t = 6T$, where $T = c/\lambda$ is the laser period.

Figure 5.4 shows a) the electric field temporal evolution at the gap center (normalized to the input peak amplitude a_0), b) a snapshot of the 2D spatial map of the electric field and c) the charge density difference

at the gap borders, both at the time when the electric field is maximized at the gap center.

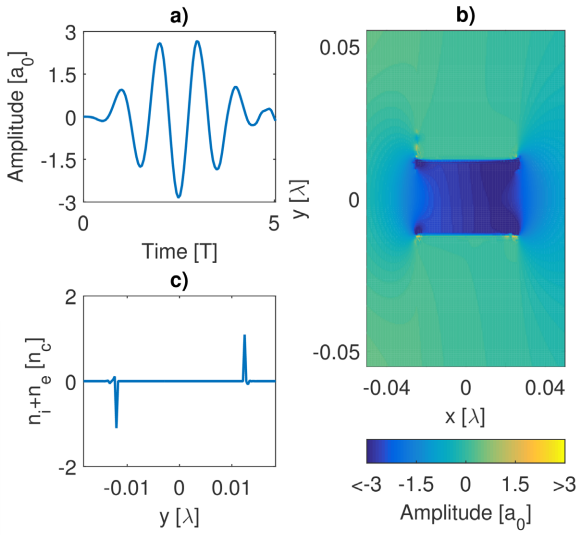

Figure 5.4: Results obtained for the described simulation setup. a) Temporal evolution of the electric field at the gap center (normalized to the input peak amplitude a_0), b) 2D distribution of the electric field at the instant when the maximum field at the gap center is obtained and c) spatial profile of the charge separation at the gap borders when the electric field at the gap center is maximized.

Figure 5.4 a) shows the enhancement the field inside the gap, concretely by a factor of ~ 3. The temporal evolution of the field at the gap reproduces the input field shape. This is expected since the electrons that generate this field are moved by the laser field. Secondly, the field distribution inside the gap, shown in figure 5.4 b), at the moment when it is maximized, is homogeneous, which coincides with the capacitor description. Finally, the motion of the electrons demonstrate that there is a charge separation at the gap borders, seen in figure 5.4 c) at the moment when the field is maximized, and that the electrons oscillate around the ion background.

A quick calculation can be done to further verify the capacitor description. The electric field from a plane parallel capacitor is given by $E = Q/\varepsilon_0$, where Q is the charge accumulated at the borders of the

capacitor and ε_0 the vacuum permittivity. We assume that in our case this charge is given by the charge separation at the borders of the capacitor, caused by the electron motion:

$$Q = qn\Delta d \tag{5.3}$$

where q is the electron unit charge, n the particle density in the separation region ($n = n_{ion} - n_{electron}$) and Δd the width of the separation sheath. Taking these values from the data plotted in figure 5.4 c), we have that $\Delta d \approx 6.4 \cdot 10^{-4}\lambda$ and $n \approx 0.5 n_c$, yielding to a field of $E \approx 2.96 a_0$, which is very close to the measured maximum if figure 5.4 a), of $E = 2.85 a_0$.

5.2.2.1 Effect of different parameters

There are several factors that can affect this excitation. In this subsection we address briefly the effect of the most relevant ones: the polarization of the laser pulse, the gap width, the target thickness and the intensity of the laser pulse.

5.2.2.1.1 Polarization

The functioning of this mechanism demands that the field is able to move the electrons in the normal direction to the gap border surface, therefore it requires the use of a field polarized into the simulation plane. To verify this, figure 5.5 shows the temporal evolution of the electric field inside the gap when the pulse is polarized in the simulation plane and when it is perpendicular to it. The simulation parameters are the same as in figure 5.4. It is clear that in the latter case the pulse is not enhanced, but quite the opposite. Furthermore both signals are phase-shifted by a π phase, that is consistent with the fact that the interaction is different in both cases. The field inside the gap when the polarization is perpendicular to the simulation plane decreases because part of the field gets reflected and part transmitted.

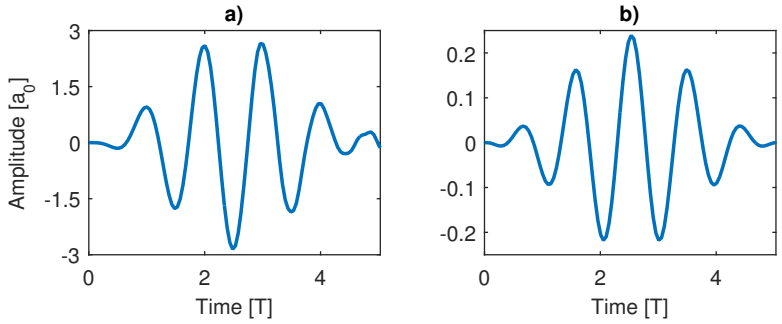

Figure 5.5: Temporal evolution of the field at the gap center for a) a pulse polarized in the simulation plane and b) a pulse polarized perpendicular to the simulation plane.

5.2.2.1.2 Gap width and target thickness

In the ideal case, the field inside an infinite plane-parallel capacitor is independent of the separation between the parallel charged planes, however in this particular case there is not an infinite capacitor and its functioning depends on the local intensity of the electric field in the gap, that at the same time depends on the gap width and on the thickness of the target. A quick parametric scan reveals some features of the dependence of this process on the electric field enhancement. Figure 5.6 shows the maximum electric field at the gap center versus the gap width and the target thickness. It can be observed that as the gap width increases, the enhancement factor decays, since when the gap width goes beyond the wavelength the field goes across the gap almost unperturbed and when the gap width is much lower than the wavelength, the capacitor description is fulfilled. The dependence of the enhancement factor with the target thickness shows that there is an optimal target thickness for the amplification of the field inside the gap. If the target is very thick, the field is not able to penetrate inside the gap, whereas if it is very thin, the surface where the charge is accumulated is reduced, thus the capacitor description is not valid anymore.

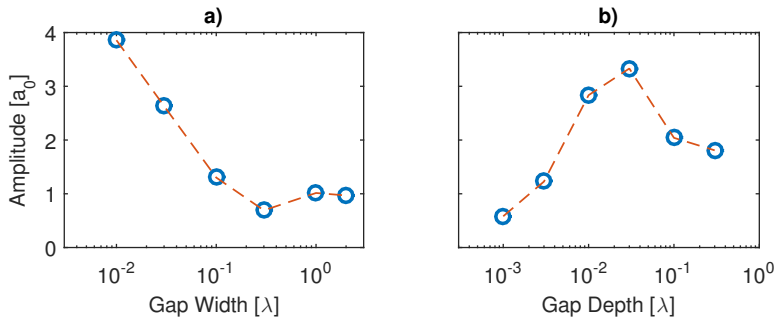

Figure 5.6: Enhancement factor of the electric field at the gap center by varying a) the gap width and b) the thickness of the target.

5.2.2.1.3 Laser pulse intensity

The well functioning of this mechanism depends on the survival of the gap, therefore if the plasmon oscillations are on the order of the gap width and the laser pulse length has several cycles, we will start to see deviations of this mechanism. In light of these facts, we should keep the intensity well below the relativistic threshold and the pulse width of no more than a few cycles.

When the field strength goes beyond the restoring ion force, then the gap will be filled with electrons that will distort the electric field inside it. The intensity at which this happens depends also on the pulse length, as longer interaction times will distort the target more.

The dependence of the maximum electric field at the gap center with the input laser intensity is shown in figure 5.7. It can be seen that the enhancement factor increases with a sudden jump at a certain intensity region, indicating the transition to the regime where the ion restoring force is overcomed by the electric field. It is important to note that the data are normalized to the input a_0 for each intensity, therefore while in relative terms the enhancement is the same for intensities below 10^{14} Wcm^{-2}, in absolute terms it would grow linearly with the input field strength a_0.

The high intensity limit, at which the target is destroyed, is depicted

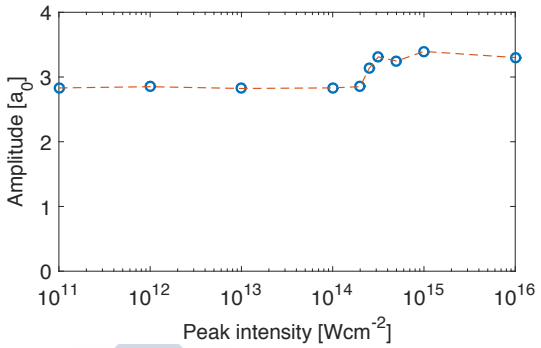

Figure 5.7: Enhancement factor of the electric field at the gap center by varying the intensity of the laser pusle.

in figure 5.8, where a laser pulse of intensity $I = 10^{18}$ Wcm^{-2} has been used. It can be seen how the original structure does not survive the interaction with the laser pulse and therefore the evolution of the field at the gap center is disrupted by its disappearance, changing its shape respect to the one obtained at lower intensities. The field enhancement factor is also affected, being reduced in comparison with the one for non-relativistic intensities. In addition, the field 2D distribution at the time where the maximum is found for lower intensities is very inhomogeneous. It is important to note the big decrease on the maximum field at the gap center in comparison with the values shown in figure 5.7.

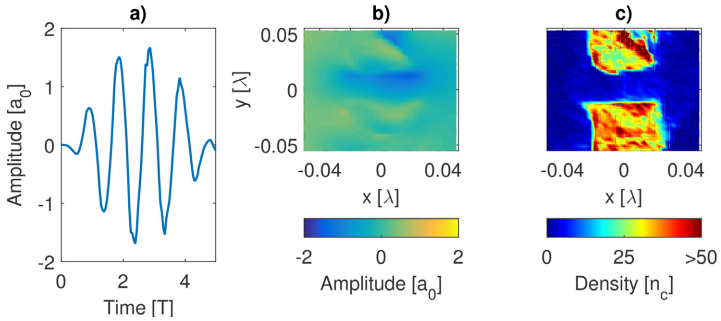

Figure 5.8: Results for a laser intensity of $I = 10^{18}$ Wcm^{-2}: a) temporal evolution of the field at the gap center and 2D distributions of b) the electric field and c) the electron density at the time where the maximum field at the gap center happened for lower intensities.

In summary, this mechanism for field enhancement only works for fields polarized parallel to the gap, at non-relativistic intensities, and for very thin targets with a sub-wavelength gap width.

5.3 PHASE MATCHING EFFECTS IN NANOANTENNAS

Recently it has been shown that a laser oscillator's electric field, when focused into a nanoantenna structure filled with a gas, can be amplified enough to trigger HHG [289–291]. This has been also reported very recently for HHG in nanostructured crystalline targets [292, 293]. Some works addressing the properties of HHG in this scheme have been published: a first theoretical investigation of HHG in bow-tie antennas and nanocones reported the extension of the plateau's cutoff frequency [294]. The generation of isolated attosecond pulses was studied theoretically in coupled-ellipsoid nanostructures [295]. HHG and attosecond pulse generation has also been studied in nano-structured metallic funnel-waveguides [296]. In the experiments [289–291], bow-tie shaped elements were etched in gold films evaporated on sapphire substrates and submitted to oscillator pulses with a length of ≤ 10 fs and a wavelength of 800 nm, with a peak intensity at focus of $\sim 10^{11}$ Wcm^{-2}, at 78 MHz repetition rate. The bow-tie gaps are filled with Ar or Xe, exiting a gas nozzle at 115 to 375 Torr pressures. Under these conditions, the plasmonic oscillation enhances the driving field subtantially [289]. It should be noted, however, that the field enhancement is located at the antenna's gap, and not at the substrate, where the intensity remains below the damage threshold. Gold nanoantennas can tolerate high field amplitudes before being damaged, depending on the particular conditions of resonance, reaching intensities up to 10^{14} Wcm^{-2} for antenna's lengths of $140 - 175$ nm and pulse lengths below < 10 fs [291]. Despite these promising characteristics, the small interaction volume in comparison with that of the conventional HHG experiments at higher intensities, reduces the efficiency of the target volume emission in 6 to 8 orders of magnitude [290, 297]. Also, resonant-enhanced atomic line emission [290, 298] can mask the harmonic signal, making it difficult to distinguish between HHG and atomic fluorescence. Very recently, high-harmonics have been efficiently produced from nanostructures on

sapphire [292] and silicon [293], which makes HHG in nanostructured crystalline targets a promising candidate to implement this setup.

The most common sources of phase mismatch for HHG in gases have a marginal role when the propagation distances are shorter than the wavelength (see methods in reference [297]). Considering this, phase matching effects should be residual in HHG from nanostructures, even with the relative high pressures used in the experiments mentioned above. We demonstrate with this study [271] that phase matching not only has to be taken into account in these setups, but it plays a relevant role even at the nanometric scale.

5.3.1 Simulation setup and numerical methods

The simulation setup considered is the following: a 800 nm laser pulse, with a $\sin^2$ longitudinal profile with a 5-cycle width and a plane transverse profile, is aimed to a bow-tie shaped nanoantenna, whose gap is filled with Ar gas. The driving field's peak intensity, $6.7 \cdot 10^{11}$ Wcm^{-2} (field peak amplitude 2.25 GV/m) is chosen as a safe value below the damage threshold [291]. The field is linearly polarized along the z axis. The antenna dimensions are 50 nm (thickness), 175 nm (half length) and 20 nm (gap), similar to those used in previous experiments [289,291,297]. To simulate this interaction we use three-dimensional PIC simulations, with a simulation box of dimensions $150 \times 300 \times 470$ nm, that encloses completely the antenna, with a spatial resolution of 0.015 in simulation units, periodic boundary conditions in the transverse dimensions and absorbing boundary conditions in the longitudinal dimension. The plasma is composed of electrons and gold ions, with a density of $34.3 n_c$ and 1 particle per cell. The plasma profile has a steep profile. Figure 5.9 shows the scheme of the system, along with the field profile across the gap height (z axis) at the gap center ($x = y = 0$) at the moment of peak intensity ($t_{max} = 8$ fs).

It is important to note that the field intensity distribution inside the gap is inhomogeneous. Previous studies have shown that for strong spatial inhomogeneities, the harmonic spectrum radiated by a single atom is modified [299], extending to frequencies beyond the spectral cut-off. Our integration of the time-dependent Schrödinger equation indicates

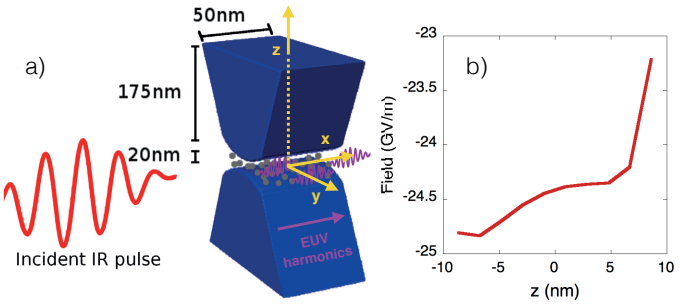

Figure 5.9: a) Simulated interaction scheme: a few-cycle NIR beam is focused into a gold bow-tie nano antenna. Harmonics are generated from argon gas by the enhanced driving field at the antenna's gap. b) Field amplitude profile across the gap, at the antenna's center, induced at the peak of the driving field at the time t_{max}.

that this effect is negligible for the interaction parameters considered here.

HHG and its propagation is computed at the antenna's gap volume using the electromagnetic field propagator [300] for a sufficiently large sample of individual atoms (10^5). The target (gas cell or gas jet) is discretized into a set of elementary radiating volumes centered at $\vec{r}_j$, and propagate the emitted field $\vec{E}_j(\vec{r}_j, t)$ to the far-field detector, located at $\vec{r}_d$:

$$\vec{E}_j(\vec{r}_d, t) = \frac{q_j \vec{s}_d}{c^2 |\vec{r}_d - \vec{r}_j|} \times \left[\vec{s}_d \times \vec{a}_j \left(t - \frac{|\vec{r}_d - \vec{r}_j|}{c} \right) \right] \tag{5.4}$$

where $\vec{a}_j$ is the dipole acceleration, q_j is the charge of the electron, $\vec{s}_d$ is the unitary vector pointing to the detector, and $\vec{r}_d$ and $\vec{r}_j$ are the position vectors of the detector and of the elementary radiator j, respectively. Equation (5.4) assumes that the harmonic radiation propagates with the vacuum phase velocity, which is a reasonable assumption for high-order harmonics. Finally the total field at the detector is computed as the coherent addition of these elementary contributions. Propagation effects in the fundamental field, such as the production of free charges, the refractive index of the neutrals, the group velocity walk-off [301], as well as absorption in the propagation of the harmonics, are included, al-

though they are negligible in gas targets for sub-wavelength propagation distances.

In the case of intense fields, the computation of the dynamics of the elementary radiators is not trivial, as the interaction is non-perturbative. Due to the large number of radiators, using the exact numerical integration of the Time Dependent Schrödinger Equation (TDSE) becomes extremely expensive, specially for mid-infrared driving fields. Therefore, the use of simplified models is required. For these intense fields, the S-matrix approaches combined with the Strong-Field Approximation (SFA) [302–304] are demonstrated to retain most of the features of the HHG [272, 273]. We will use an extension of the standard SFA (SFA+), where the acceleration of the j radiator ($\vec{a}_j$) is found from two contributions, $\vec{a}_{b,j}$ and $\vec{a}_{d,j}$, the first being the standard SFA expression, and the later being a correction due to the instantaneous dressing of the ground state during the electron's recollision. The method used here computes the dipole acceleration directly from the superposition of the contributions of each Volkov wave. Each contribution can be integrated separately as an ordinary 1D equation, leading to a very efficient algorithm without resorting to the saddle-point approximation [305, 306]. This method combining high harmonic generation and propagation has shown excellent agreement with HHG experiments with conventional set-ups, where phase matching plays a relevant role [279, 307, 308]. For the pressures ($<$ 375 Torr) and nanometric optical paths considered here, the influence of the neutral and free carriers on the driving field is negligible [297], consequently the harmonic intensity signal follows a power-two scaling with the number of radiators, typical of a coherent build-up process. To obtain a faithful comparison of the phase matching conditions at different interaction volumes, the results of our calculations have been normalized to the same number of radiators.

We note that, despite quantum SFA models are derived for homogenous fields, it has been pointed out before that the field inhomogeneity in our case is irrelevant at the single-atom level, and therefore SFA can be used in our simulations.

5.3.2 Results

In figure 5.10 a) we plot in violet the total (volume-integrated) propagated harmonic emission from the gas enclosed in the gap, for the antenna structure depicted in figure 5.9 a), as collected by a far-field detector located in the x-axis. For comparison, the effective single-atom emission is shown in blue. We define the latter as the coherent emission of the same number of atoms in the volume, all located at the coordinate origin (gap's center), therefore propagation effects are excluded. Note that the drop in harmonic efficiency by a factor 4 reflects the fact that the average intensity in the interaction volume is lower than the intensity at the gap's center –where the effective single-atom emission is computed–, so it cannot be considered as a direct proof of phase mismatch degradation. In contrast, panels 5.10 b)-d) provide for a more precise diagnostic of the role of phase matching.

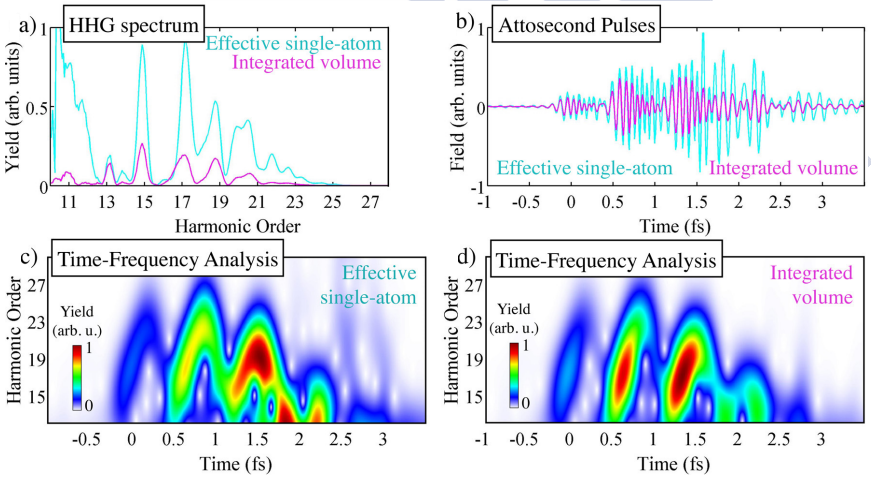

Figure 5.10: a) Violet: Harmonic spectrum from the volume-integrated propagated signal emitted by the argon gas enclosed in the antenna's gap (linear scale), for the antena's design depicted in figure 5.9 a). Blue: emission by the same number of atoms positioned at the coordinate origin (referred in the text as effective single-atom emission). b) EUV field emitted by the antenna, after filtering out the harmonic orders below 10, c) Time-frequency analysis of the emission of the effective single-atom and d) the same for the volume-integrated propagated signal.

Figures 5.10 c)-d) plot the time-frequency analysis of the harmonic emission for the effective single-atom and the integrated volume, re-

spectively. The wedge-shaped intensity structures have a well-known origin [309], corresponding to the pair of electron trajectories that rescatter with the parent ion with the same kinetic energy every half cycle. The first harmonic emission corresponds to the short trajectories (positive slope) and the second to the long ones (negative slope). The comparison between the panels c) and d) of figure 5.10 shows that the contribution of the long trajectories is strongly suppressed in the integrated-volume emission. The elimination of trajectory contributions is a well known consequence of phase matching in HHG, and has a practical interest for attophysics, as the associated attosecond bursts become narrower when this happens. This is shown in figure 5.10 b), where it is plotted the temporal structure of the higher part of the harmonic spectrum (harmonic orders > 10). It becomes apparent how the contrast and width of the attosecond pulses is narrower in the integrated volume case. Also, as both trajectory contributions exhibit opposite chirp, the suppression of one type leads to attosecond pulses with simpler chirp, easier to be compensated near the Fourier limit [310].

To gain insight into the nature of this suppression, we plot in the left column of figure 5.11 the local field intensity distributions inside the antenna's gap, for the main simulation planes ($x = 0;\ y = 0;\ z = 0$). The intensity distributions are plotted at the time instant when the enhanced field has its maximum (t_{max}). As expected, the antenna structure imposes intensity variations at the nanometer scale, the intensity gradients being more pronounced in the $\hat{x}$ and $\hat{y}$ directions. On the right column of figure 5.11 it is shown the time dependent field amplitudes at three points along the y, x and z directions, respectively, indicated with white crosses in the left column. The inspection of these plots shows no appreciable phase shifts of the driving field within the gap's volume, demonstrating that the nanostructure geometry does not have an effect in the field's phase, but it does in the intensity.

Therefore, our analysis rules out three of the main factors contributing to the phase mismatch of harmonic propagation: on one side, neutrals and plasma contributions are negligible in this sub-wavelength scale of the propagation, on the other side, the nanoantenna geometry does not have a relevant effect in phase shifting the field inside the gap volume.

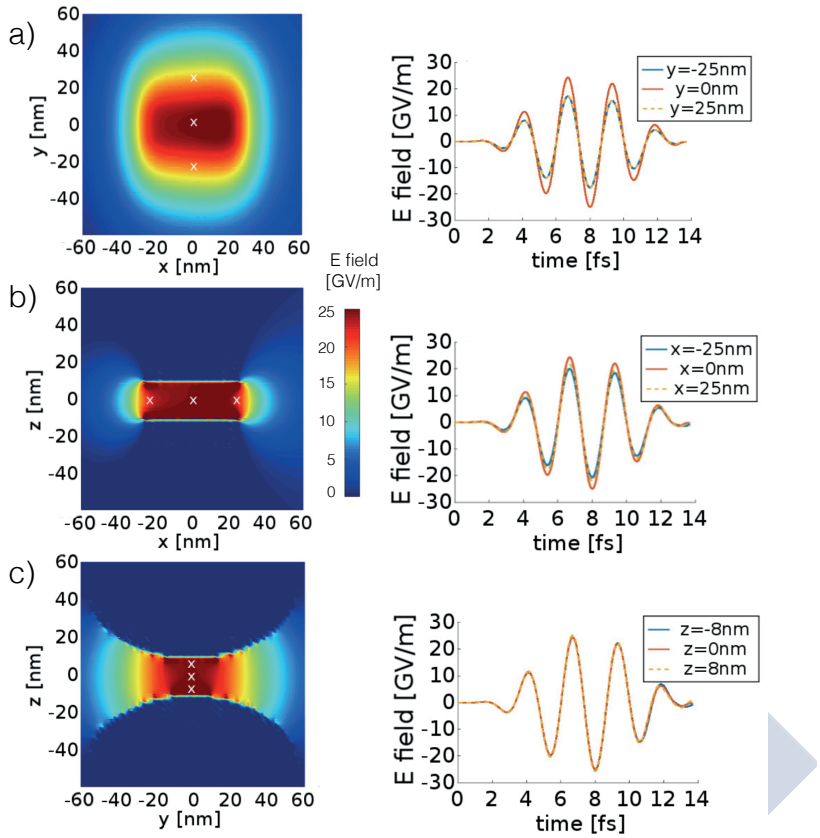

Figure 5.11: Left column: Absolute value of the field amplitude at the planes a) $z = 0$, b) $y = 0$ and c) $x = 0$ at the time t_{max}. Right column: Time-dependent amplitudes at three points in each of the planes (white crosses in the left-column plots).

This leaves the intrinsic phase as the main source of phase mismatch. Since this phase term is proportional to the local intensity, the spatial inhomogeneity shown in figure 5.11 will be translated to phase shifts of the harmonics emitted at different regions of the interaction volume. Note that this remarkably small scale of phase mismatch is induced by the non-perturbative nature of the HHG and, therefore, will not be found in ordinary perturbative harmonic generation.

To demonstrate the spatial shift of the harmonic phase, we show in figure 5.12 a)-c) the spatial maps of the intensity (color background) and

phase (arrows) for the 17th harmonic of the spectrum shown in figure 5.10 a), along the main planes of the interaction volume. The arrow distributions define a coherence length in the medium as the distance between the nearest points with opposite arrow directions, i.e. the distance between two atoms whose harmonic emission interferes destructively. Note that HHG is susceptible to phase shifts in the propagation direction as well as in the transverse dimensions [307]. In the case depicted in figure 5.12, the interaction volume is too small to include a complete half rotation of the arrows, therefore the coherence lengths are larger than the target's size in any dimension. However, despite there is not a complete destructive interference, it is also evident that there is a spatial phase shift in the harmonic emitted and, therefore, the total yield should be affected by the partial cancellation. It can also be observed that these phase shifts are more pronounced in regions with higher intensity gradients of the driving field. This demonstrates the connection between the harmonic phase shift and intensity variations of the driving field, a particular feature of the intrinsic phase in HHG. As mentioned above, the intrinsic phase is proportional to the electron's excursion time. Long trajectories have a stronger dependence with the intensity than short ones and are more susceptible to intrinsic-phase mismatch. This explains the selective suppression of the long trajectory contributions, revealed by the time-frequency analysis shown in figure 5.10 c)-d).

5.3.2.1 Modification of the antenna geometry

The modification of the antenna structure affects the plasmon oscillations as well as the geometry of the enhanced field. We have explored the effect in HHG of increasing the antenna's thickness and the gap width from the original antenna structure in figure 5.9.

Figure 5.13 depicts the results obtained for a 100 nm thick bow-tie antenna. Our computations show that for this case, the field enhancement in the gap is less than in the 50 nm thick case in the main text. In order to compare properly both situations, we have increased the driving field's intensity in the 100 nm case by a factor 1.5, such that the maximum peak field inside the gap remains the same in both cases. Under these conditions, figure 5.13 a)-b) show that a thicker nano-antenna is less

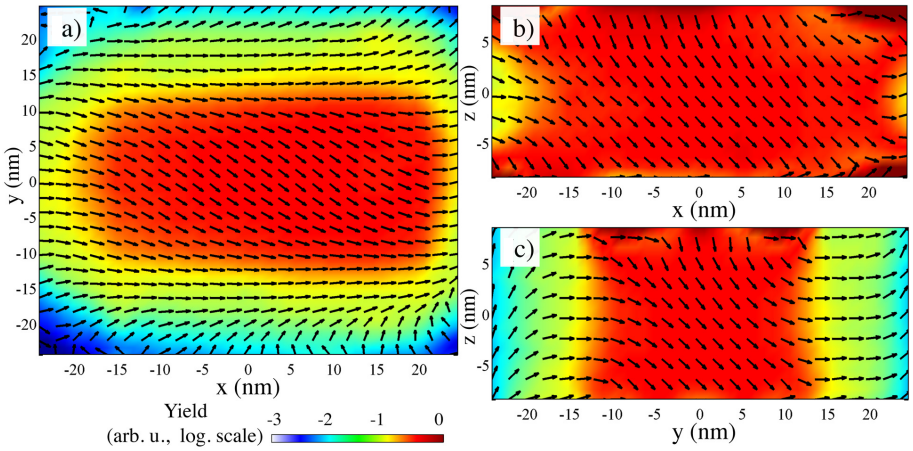

Figure 5.12: Intensity (color) and phase (arrows) maps of the spatial contributions to the 17th harmonic far field plotted along the planes shown in figure 5.11 a)-c).

efficient for the harmonic generation and it does not present a clear advantage in the temporal characteristics of the attosecond pulses. The arrow map plotted in figure 5.13 c) shows that the interaction region is larger than the coherence length.

Increasing of the gap width from 20 nm to 40 nm conveys an enhancement of the efficiency, as shown in figure 5.14 a), demonstrating that structures with wider gaps are optimal for harmonic generation. In order to compare properly both situations, we have increased the driving field peak intensity in the 40 nm case by a factor of 1.77, such that the peak of the amplified field inside the gap remains the same in both situations. Interestingly, the generated attosecond pulses have a higher contrast, which suggest that the suppression of the long trajectory contributions is more effective for wider gaps. The arrow map in figure 5.14 c) shows that since the phase shift along the gap is small, the increase of the gap distance does not include regions with oposite phases in the interaction volume. Therefore wider gaps seem to be more favorable for the efficient harmonic generation, provided that the weaker plasmon resonant enhancement is compensated by the increase of the driving field intensity.

Our findings demonstrate that phase matching becomes a limit for

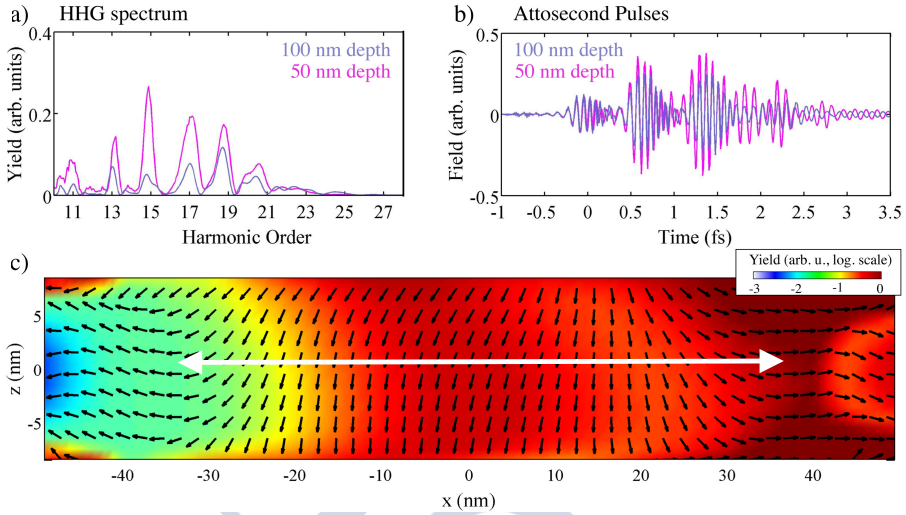

Figure 5.13: Results for the spectrum emitted by a bow-tie antenna structure with the same geometry as the one considered in figure 5.9, but with its thickness increased by a factor two (100 nm). The driving field parameters are also those used in the main text, except for the driver's intensity, that has been increased by a factor of 1.5, to match the peak field amplitude at the center of the gap in both cases. a) Spectrum of the gap's volume harmonic emission in comparison with the 50 nm thickness case. b) Attosecond pulses after selecting the higher frequencies of the harmonic spectra (harmonic orders > 10), in comparison with the 50 nm thickness case. c) Map of the 17th harmonic intensity (color background) and phases (arrows) for the 100 nm thick antenna. The white double arrow indicates the coherence length.

thicker antennas, due to the intensity variation along the propagation dimension. On the other hand, the softer phase variations along the z axis allow to enhance the harmonic emission by increasing the antenna's gap and, therefore the interaction volume. The increase of the radiating volume can help to raise the contrast between the harmonic emission and the incoherent background [290].

In conclusion, we demonstrate that phase matching plays a relevant role in HHG in nanostructures. Despite the nanoscale propagation distances preclude any significant influence of the common sources of phase mismatch, high harmonics have still a substantial phase shift due to the non-perturbative intrinsic phase, this is an universal effect and will be found in any setup like the one described here. Phase-matching at the nanoscale can then be used to modify the spatio-temporal properties of

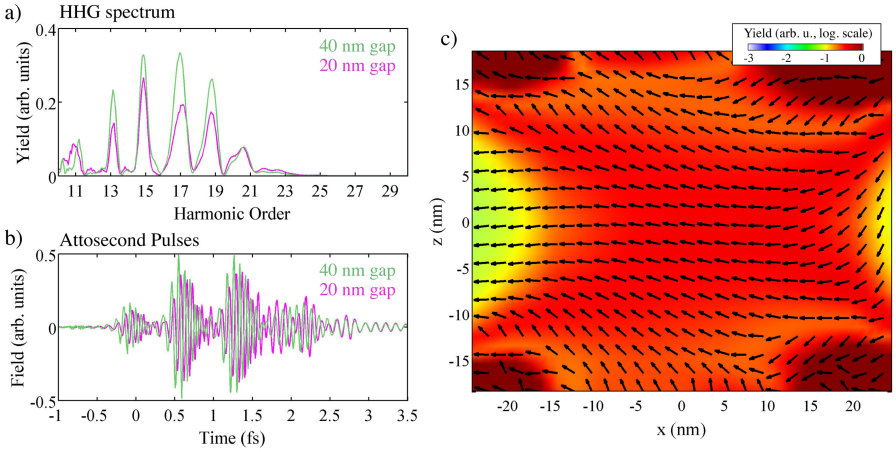

Figure 5.14: Results for the HHG emitted by a bow-tie antenna structure with the same geometry as the considered in figure 5.9 but with the gap size increased by a factor two (40 nm). The driving field parameters are also those used in the main text, except for the driver's intensity, that has been increased by a factor 1.77, to match the peak field amplitude in the gap in both cases. a) Spectrum of the gap's volume harmonic emission in comparison with the 20 nm gap case. b) Attosecond pulses after selecting the higher frequencies of the harmonic spectra (harmonic orders > 10), in comparison with the 20 nm gap case. c) Map of the 17th harmonic intensity (color background) and phases (arrows) for the antenna with 40 nm gap.

the harmonics, through selection of the quantum path trajectories, and hence several applications that make use of phase-matching in macroscopic scenarios may be also applicable here. It has been also shown that phase matching can be engineered modifying the antenna's geometry, which is understandable from the fact that the field distribution over time inside the gap volume is affected by the target shape.

Recent studies of HHG in crystalline materials [311] demonstrate the existence of an intensity-dependent phase, analogous to the intrinsic phase in HHG from atoms. This result together with the finding that nanostructured crystalline targets enhance HHG [292, 293], suggest that our conclusions may be also applicable to HHG from nanostructured crystalline materials.

5.4 CONCLUSIONS

We have introduced the concept of HHG in gas targets and explained briefly its nature and its main properties, along with the concept of phase-

matching, which is very important for several applications.

We have proposed a method to enhance locally at sub-wavelength distances the intensity of a laser pulse, making use of plasmon oscillations at the surface of an overdense plasma, plus the diffraction from a sub-wavelength aperture on a nanometric thick target. This setup creates a sub-wavelength capacitor that oscillates with the laser field and enhances the field locally.

The combination of the previous two concepts has been used to study HHG in nanostructured solid targets, where the gas that generates the harmonics is enclosed inside a nanogap where the capacitor is formed. This study has shown, on the contrary of what was typically assumed, that the generation of high harmonics in these setups is affected by phase-matching effects, and that the source of phase-mismatch is the intrinsic phase, arising from the field spatial distribution in the gap volume. These findings represent and advancement on the understanding of HHG in gas targets at sub-wavelength distances, and could be even applicable to HHG in crystalline targets, as suggested from very recent publications.

USC
UNIVERSIDADE
DE SANTIAGO
DE COMPOSTELA

CONCLUSIONS

This thesis has been mainly devoted to the study, via particle in cell (PIC) simulations, of the interaction between intense and ultrashort laser pulses with solid targets, in the form of ionized overdense plasmas. The focus of this work has been to make use of two of the most known outcomes of this interaction, high harmonic generation (HHG) in the reflected field and proton acceleration via target normal sheath acceleration (TNSA), to be able to propose new experimental setups where some of their properties can be enhanced and used for applications. The obtained results will find applicability into attoscience, atomic physics, medical physics or materials physics, among many other examples.

We have analyzed the phenomenon of high harmonic generation in solid targets, introducing its main properties and its dependence with different relevant physical factors. We have proposed two setups to achieve the isolation of a single attosecond pulse: the first is a new version of the already known polarization gating mechanism, where the polarization gate is generated via a nonlinear mechanism known as cross polarized wave generation (XPWG), in combination with a quarter-wavelength plate; the second is a completely new method proposed by us, consisting on the coherent combination of two laser pulses with a small frequency shift between them, forming a beating pattern that reduces effectively the width of the resulting pulse and thus the number of attosecond pulses in the train. The two methods are able to achieve the isolation of a single attosecond pulse, using many-cycle laser pulses with table-top intensities. We have also studied in depth how to control the polarization of the generated attosecond pulses by tuning the polarization state and angle of incidence of the laser pulse, making use of the relativistic electronic spring (RES) model, which describes accurately the HHG process in the regime where the relativistic similarity parameter $S = n/a_0$ is in the range $[0.05,\ 5]$. We have found that there is a region in the space of parameters for which near circularly polarized attosecond pulses are generated, which is independent on the S parameter in the range of values

addressed. We have also found that, as the S parameter decreases and the RES mechanism becomes more dominant, a new parameter region for the generation of circular attosecond pulses appears, allowing their production even when the laser pulse is linearly polarized, under certain conditions.

Proton acceleration via the TNSA mechanism has been studied, for the particular case in which the target front surface is structured with periodic grating-like nanostructures on top of it. We have found that triangular nanostructures allow the absorption of almost the whole laser pulse energy, and that this enhanced absorption translates into an increase of the proton energy by a factor of ~ 5 in comparison with when a flat target is used. An analytical model was introduced to explain the reason behind the enhanced absorption, based on the motion of the electrons in the vacuum gaps of the structure under the influence of the laser electric field. The model predicted an optimal structure design to maximize energy absorption, which was confirmed by performing a parametric scan with PIC simulations. Finally, the robustness of the enhanced energy absorption from these targets under typical deviations that can be found in a laboratory was addressed, on one side it was found that the very high absorption percentages are maintained for a range of laser intensities, by changing the ion species or by adding irregularities to the structures, and on the other side it was observed that the addition of a pre-plasma is strongly detrimental to the enhanced absorption.

We have studied the interaction between a laser pulse of low intensity ($a_0 \ll 1$) and a target with a nanometric aperture, finding that if the aperture width and the target thickness are below the laser wavelength, the plasmon oscillations of the charge density at the aperture edges generate a parallel plate nanocapacitor that enhances locally the intensity of the electric field. The findings from this setup have been used to study HHG from gas media when a gas is enclosed in the nanogap of a bow-tie nanostructure. Prior to this, the phenomenon of HHG in gas targets was introduced and its main properties explained, with an emphasis on the phase-matching effects. Our findings demonstrated that the local enhancement of the electric field in the gap of the nanoantenna affects HHG, such that phase-matching effects were found to play a relevant

role in these setups, in opposition of what was typically assumed, since the most common sources of phase-mismatch are not relevant in these setups. The intrinsic phase of the emitted harmonics is responsible for the phase-matching effects, indicating that this is an universal effect and will be found in any setup involving nanoantenna structures.

USC
UNIVERSIDADE
DE SANTIAGO
DE COMPOSTELA

BIBLIOGRAPHY

[1] A. Macchi. *A Superintense Laser-Plasma Interaction Theory Primer*. Springer, 2012.

[2] P. Gibbon. *Short Pulse Laser Interactions with Matter*. Imperial College Press, 2005.

[3] D. A. Jaroszynski, R. Bingham, and R. A. Cairns. *Laser-Plasma Interactions*. Tailor & Francis, 2009.

[4] U. Teubner and P. Gibbon. High-order harmonics from laser-irradiated plasma surfaces. *Rev. Mod. Phys.*, 81(2):445–479, 2009.

[5] C. Thaury and F. Quéré. High-order harmonic and attosecond pulse generation on plasma mirrors: basic mechanisms. *J. Phys. B*, 43(21):213001, 2010.

[6] H. Daido, M. Nishiuchi, and A.S. Pirozhkov. Review of laser-driven ion sources and their applications. *Rep. Prog. Phys.*, 75(5):056401, 2012.

[7] A. Macchi, M. Borghesi, and M. Passoni. Ion acceleration by superintense laser-plasma interaction. *Rev. Mod. Phys.*, 85(2):751–793, 2013.

[8] Ferenc Krausz and Misha Ivanov. Attosecond physics. *Rev. Mod. Phys.*, 81:163–234, 2009.

[9] P.M. Paul, E.S. Toma, P. Breger, G. Mullot, F. Augé, Ph. Balcou, H.G. Muller, and P. Agostini. Observation of a train of attosecond pulses from high harmonic generation. *Science*, 292(5522):1689–1692, 2001.

[10] M. Hentschel, R. Kienberger, Ch. Spielmann, G.A. Reider, N. Milosevic, T. Brabec, P. Corkum, U. Heinzmann, M. Drescher,

and F. Krausz. Attosecond metrology. *Nature*, 414(6863):509–513, 2001.

[11] P. Agostini and L.F. DiMauro. The physics of attosecond light pulses. *Rep. Prog. Phys.*, 67(6):813, 2004.

[12] I.P. Christov, M.M. Murnane, and H.C. Kapteyn. High-harmonic generation of attosecond pulses in the "single-cycle" regime. *Phys. Rev. Lett.*, 78:1251–1254, 1997.

[13] J. Mauritsson, P. Johnsson, E. Gustafsson, A. L'Huillier, K. J. Schafer, and M. B. Gaarde. Attosecond pulse trains generated using two color laser fields. *Phys. Rev. Lett.*, 97:013001, 2006.

[14] P. Antoine, A. L'Huillier, and M. Lewenstein. Attosecond pulse trains using high order harmonics. *Phys. Rev. Lett.*, 77:1234–1237, 1996.

[15] S.E. Harris, J.J. Macklin, and T.W. Hänsch. Atomic scale temporal structure inherent to high-order harmonic generation. *Opt. Comm.*, 100(5):487–490, 1993.

[16] R. Bartels, S. Backus, E. Zeek, L. Misoguti, G. Vdovin, I. P. Christov, M. M. Murnane, and H. C. Kapteyn. Shaped-pulse optimization of coherent emission of high-harmonic soft x-rays. *Nat. Lett.*, 406(6792):164–166, 2000.

[17] J. Zhou, J. Peatross, M. M. Murnane, H. C. Kapteyn, and I. P. Christov. Enhanced high-harmonic generation using 25 fs laser pulses. *Phys. Rev. Lett.*, 76:752–755, 1996.

[18] G. Sansone, L. Poletto, and M. Nisoli. High-energy attosecond light sources. *Nat. Photon.*, 5:655–663, 2011.

[19] N. H. Burnett, H. A. Baldis, M. C. Richardson, and G. D. Enright. Harmonic generation in CO_2 laser target interaction. *Appl. Phys. Lett.*, 31(3):172–174, 1977.

[20] R. L. Carman, D. W. Forslund, and J. M. Kindel. Visible harmonic emission as a way of measuring profile steepening. *Phys. Rev. Lett.*, 46:29–32, 1981.

[21] R. L. Carman, C. K. Rhodes, and R. F. Benjamin. Observation of harmonics in the visible and ultraviolet created in CO_2-laser-produced plasmas. *Phys. Rev. A*, 24:2649–2663, 1981.

[22] B. Bezzerides, R. D. Jones, and D. W. Forslund. Plasma mechanism for ultraviolet harmonic radiation due to intense co_2 light. *Phys. Rev. Lett.*, 49:202–205, 1982.

[23] C. Grebogi, V. K. Tripathi, and H. Chen. Harmonic generation of radiation in a steep density profile. *Phys. Fluids*, 26(7):1904–1908, 1983.

[24] D. von der Linde, T. Engers, G. Jenke, P. Agostini, G. Grillon, E. Nibbering, A. Mysyrowicz, and A. Antonetti. Generation of high-order harmonics from solid surfaces by intense femtosecond laser pulses. *Phys. Rev. A*, 52:R25–R27, 1995.

[25] S. Kohlweyer, G.D. Tsakiris, C.-G. Wahlström, C. Tillman, and I. Mercer. Harmonic generation from solid-vacuum interface irradiated at high laser intensities. *Opt. Comm.*, 117(5):431–438, 1995.

[26] P. Gibbon. Harmonic generation by femtosecond laser-solid interaction: A coherent "water-window" light source? *Phys. Rev. Lett.*, 76:50–53, 1996.

[27] R. Lichters, J. Meyer ter Vehn, and A. Pukhov. Short pulse laser harmonics from oscillating plasma surfaces driven at relativistic intensity. *Phys. Plasmas*, 3(9):3425–3437, 1996.

[28] F. Quéré, C. Thaury, P. Monot, S. Dobosz, Ph. Martin, J.-P. Geindre, and P. Audebert. Coherent wake emission of high-order harmonics from overdense plasmas. *Phys. Rev. Lett.*, 96:125004, 2006.

[29] A. A. Gonoskov, A. V. Korzhimanov, A. V. Kim, M. Marklund, and A. M. Sergeev. Ultrarelativistic nanoplasmonics as a route towards extreme-intensity attosecond pulses. *Phys. Rev. E*, 84:046403, 2011.

[30] F. Brunel. Not-so-resonant, resonant absorption. *Phys. Rev. Lett.*, 59:52–55, 1987.

[31] G. Bonnaud, P. Gibbon, J. Kindel, and E. Williams. Laser interaction with a sharp-edged overdense plasma. *Laser Part. Beams*, 9(2):339–354, 1991.

[32] Z.-M. Sheng, K. Mima, J. Zhang, and H. Sanuki. Emission of electromagnetic pulses from laser wakefields through linear mode conversion. *Phys. Rev. Lett.*, 94:095003, 2005.

[33] C. Thaury, F. Quéré, J.-P. Geindre, A. Levy, P. Ceccotti, T.and Monot, M. Bougeard, F. Reau, P. d'Oliveira, P. Audebert, R. Marjoribanks, and Ph. Martin. Plasma mirrors for ultrahigh-intensity optics. *Nat. Phys.*, 3(6):424–429, 2007.

[34] F. Quéré, C. Thaury, H. George, J.P. Geindre, E. Lefebvre, G. Bonnaud, S. Hüller, P. Monot, and Ph. Martin. Basic mechanisms of laser high-order harmonic generation from plasma mirrors. *J. Mod. Opt.*, 55(16):2711–2721, 2008.

[35] A. Tarasevitch, K. Lobov, C. Wünsche, and D. von der Linde. Transition to the relativistic regime in high order harmonic generation. *Phys. Rev. Lett.*, 98:103902, 2007.

[36] B. Dromey, S. G. Rykovanov, D. Adams, R. Hörlein, Y. Nomura, D. C. Carroll, P. S. Foster, S. Kar, K. Markey, P. McKenna, D. Neely, M. Geissler, G. D. Tsakiris, and M. Zepf. Tunable enhancement of high harmonic emission from laser solid interactions. *Phys. Rev. Lett.*, 102:225002, 2009.

[37] D. von der Linde and K. Rzàzewski. High-order optical harmonic generation from solid surfaces. *Appl. Phys. B*, 63(5):499–506, 1996.

[38] S. Gordienko, A. Pukhov, O. Shorokhov, and T. Baeva. Relativistic doppler effect: Universal spectra and zeptosecond pulses. *Phys. Rev. Lett.*, 93:115002, 2004.

[39] T. Baeva, S. Gordienko, and A. Pukhov. Theory of high-order harmonic generation in relativistic laser interaction with overdense plasma. *Phys. Rev. E*, 74:046404, 2006.

[40] L. Plaja, L. Roso, K. Rzażewski, and Maciej Lewenstein. Generation of attosecond pulse trains during the reflection of a very intense laser on a solid surface. *J. Opt. Soc. Am. B*, 15(7):1904–1911, 1998.

[41] A. Pukhov, T. Baeva, D. an der Brügge, and S. Münster. Relativistic high harmonics and (sub-)attosecond pulses: relativistic spikes and relativistic mirror. *Eur. Phys. J. D*, 55(2):407, 2009.

[42] Alexander S. Pirozhkov, Sergei V. Bulanov, Timur Zh. Esirkepov, Michiaki Mori, Akito Sagisaka, and Hiroyuki Daido. Attosecond pulse generation in the relativistic regime of the laser-foil interaction: The sliding mirror model. *Phys. Plasmas*, 13(1):013107, 2006.

[43] H. Vincenti, S. Monchocé, S. Kahaly, G. Bonnaud, Ph. Martin, and F. Quéré. Optical properties of relativistic plasma mirrors. *Nat. Comm.*, 5:3403, 2014.

[44] A. Gonoskov. Theory of relativistic radiation reflection from plasmas. *Phys. Plasmas*, 25:013108, 2018.

[45] A. Tarasevitch and D. von der Linde. High order harmonic generation from solid targets: Towards intense attosecond pulses. *Eur. Phys. J. Spec. Top.*, 175(1):35–41, 2009.

[46] P.B. Corkum, N.H. Burnett, and M.Y. Ivanov. Subfemtosecond pulses. *Opt. Lett.*, 19(22):1870–1872, 1994.

[47] S.G. Rykovanov, M. Geissler, J. Meyer ter Vehn, and G.D. Tsakiris. Intense single attosecond pulses from surface harmonics using the polarization gating technique. *New J. Phys.*, 10(2):025025, 2008.

[48] G. Zhang, M. Chen, F. Liu, X. Yuan, S. Weng, J. Zheng, Y. Ma, F. Shao, Z. Sheng, and J. Zhang. Directional enhancement of selected high-order-harmonics from intense laser irradiated blazed grating targets. *Opt. Express*, 25(20):23567–23578, 2017.

[49] X.-Z. Li, H.-B. Zhuo, D.-B. Zou, S.-J. Zhang, H.-Y. Zhou, N. Zhao, Y. Lang, and D.-Y. Yu. High-order-harmonic generation from a relativistic circularly polarized laser interacting with over-dense plasma grating. *Chin. Phys. Lett.*, 34(9):094201, 2017.

[50] L. Fedeli, A. Formenti, L. Cialfi, A. Sgattoni, G. Cantono, and M. Passoni. Structured targets for advanced laser-driven sources. *Plasma Phys. Control. Fusion*, 60(1):014013, 2018.

[51] A.P. Tarasevitch, R. Kohn, and D. von der Linde. Towards intense attosecond pulses: using two beams for high order harmonic generation from solid targets. *J. Phys. B*, 42(13):134006, 2009.

[52] M.R. Edwards and J.M. Mikhailova. Waveform-controlled relativistic high-order-harmonic generation. *Phys. Rev. Lett.*, 117:125001, 2016.

[53] G.D. Tsakiris, K. Eidmann, J. Meyer ter Vehn, and F. Krausz. Route to intense single attosecond pulses. *New J. Phys.*, 8(1):19, 2006.

[54] Yu.M. Mikhailova, V.T. Platonenko, and S.G. Rykovanov. Generation of an attosecond x-ray pulse in a thin film irradiated by an ultrashort ultrarelativistic laser pulse. *J. Exp. Th. Phys. Lett.*, 81(11):571–574, 2005.

[55] N.M. Naumova, J.A. Nees, I.V. Sokolov, B. Hou, and G.A. Mourou. Relativistic generation of isolated attosecond pulses in a λ^3 focal volume. *Phys. Rev. Lett.*, 92:063902, 2004.

[56] E. Balogh, C. Zhang, T. Ruchon, J.-F. Hergott, F. Quéré, P. Corkum, C.H. Nam, and K.T. Kim. Dynamic wavefront rotation in the attosecond lighthouse. *Optica*, 4(1):48–53, 2017.

[57] J.A. Wheeler, A. Borot, S. Monchoce, H. Vincenti, A. Ricci, A. Malvache, R. Lopez-Martens, and F. Quéré. Attosecond lighthouses from plasma mirrors. *Nat. Photon.*, 6:829–833, 2012.

[58] H. Vincenti and F. Quéré. Attosecond lighthouses: How to use spatiotemporally coupled light fields to generate isolated attosecond pulses. *Phys. Rev. Lett.*, 108:113904, 2012.

[59] Z.-Y. Chen and A. Pukhov. Bright high-order harmonic generation with controllable polarization from a relativistic plasma mirror. *Nat. Comm.*, 7:12515, 2016.

[60] G. Ma, W. Yu, M.Y. Yu, B. Shen, and L. Veisz. Intense circularly polarized attosecond pulse generation from relativistic laser plasmas using few-cycle laser pulses. *Opt. Express*, 24(9):10057–10065, 2016.

[61] F. Krausz and M.I. Stockman. Attosecond metrology: from electron capture to future signal processing. *Nat. Photon.*, 8:205–213, 2014.

[62] P. Tzallas, E. Skantzakis, L.A.A. Nikolopoulos, G.D. Tsakiris, and D. Charalambidis. Extreme-ultraviolet pump-probe studies of one-femtosecond-scale electron dynamics. *Nat. Phys.*, 7:781–784, 2011.

[63] H. Niikura, D.M. Villeneuve, and P. B. Corkum. Mapping attosecond electron wave packet motion. *Phys. Rev. Lett.*, 94:083003, 2005.

[64] S. Baker, J.S. Robinson, C.A. Haworth, H. Teng, R.A. Smith, C.C. Chirilă, M. Lein, J.W.G. Tisch, and J.P. Marangos. Probing proton dynamics in molecules on an attosecond time scale. *Science*, 312(5772):424–427, 2006.

[65] O. Smirnova, Y. Mairesse, S. Patchkovskii, N. Dudovich, D. Villeneuve, P. Corkum, and M.Yu. Ivanov. High harmonic interferometry of multi-electron dynamics in molecules. *Nature*, 460:972–977, 2009.

[66] H. Niikura, F. Legare, R. Hasbani, A.D. Bandrauk, M.Yu. Ivanov, D.M. Villeneuve, and P.B. Corkum. Sub-laser-cycle electron pulses for probing molecular dynamics. *Nature*, 417:917–922, 2002.

[67] T. Remetter, P. Johnsson, J. Mauritsson, K. Varju, Y. Ni, F. Lepine, E. Gustafsson, M. Kling, J. Khan, R. Lopez-Martens, K. J. Schafer, M. J. J. Vrakking, and A. L/'Huillier. Attosecond electron wave packet interferometry. *Nat. Phys.*, 2:323–326, 2006.

[68] H. Merdji, P. Salières, Le Déroff L., J.F. Hegott, B. Carré, D. Joyeux, D. Descamps, J. Norin, C. Lyngå, A. L'Huillier, C.G. Wahlström, M. Bellini, and S. Huller. Coherence properties of high-order harmonics: Application to high-density laser–plasma diagnostic. *Laser Part. Beams*, 18(3):495–502, 2000.

[69] S. Dobosz, G. Doumy, H. Stabile, P. D'Oliveira, P. Monot, F. Réau, S. Hüller, and Ph. Martin. Probing hot and dense laser-induced plasmas with ultrafast xuv pulses. *Phys. Rev. Lett.*, 95:025001, 2005.

[70] T. Tajima and J.M. Dawson. Laser electron accelerator. *Phys. Rev. Lett.*, 43(4):267–270, 1979.

[71] S.C. Wilks, A.B. Langdon, T.E. Cowan, M. Roth, M. Singh, S. Hatchett, M.H. Key, D. Pennington, A. MacKinnon, and R.A. Snavely. Energetic proton generation in ultra-intense laser–solid interactions. *Phys. Plasmas*, 8(2):542–549, 2001.

[72] L. Romagnani, J. Fuchs, M. Borghesi, P. Antici, P. Audebert, F. Ceccherini, T. Cowan, T. Grismayer, S. Kar, A. Macchi, P. Mora, G. Pretzler, A. Schiavi, T. Toncian, and O. Willi. Dynamics of

electric fields driving the laser acceleration of multi-mev protons. *Phys. Rev. Lett.*, 95:195001, 2005.

[73] M. Hegelich, S. Karsch, G. Pretzler, D. Habs, K. Witte, W. Guenther, M. Allen, A. Blazevic, J. Fuchs, J. C. Gauthier, M. Geissel, P. Audebert, T. Cowan, and M. Roth. Mev ion jets from short-pulse-laser interaction with thin foils. *Phys. Rev. Lett.*, 89:085002, 2002.

[74] B. M. Hegelich, B. Albright, P. Audebert, A. Blazevic, E. Brambrink, J. Cobble, T. Cowan, J. Fuchs, J. C. Gauthier, C. Gautier, M. Geissel, D. Habs, R. Johnson, S. Karsch, A. Kemp, S. Letzring, M. Roth, U. Schramm, J. Schreiber, K. J. Witte, and J. C. Fernández. Spectral properties of laser-accelerated mid-z mev/u ion beams. *Phys. Plasmas*, 12(5):056314, 2005.

[75] M. Allen, P.K. Patel, A. Mackinnon, D. Price, S. Wilks, and E. Morse. Direct experimental evidence of back-surface ion acceleration from laser-irradiated gold foils. *Phys. Rev. Lett.*, 93:265004, 2004.

[76] P. Mora. Plasma expansion into a vacuum. *Phys. Rev. Lett.*, 90:185002, 2003.

[77] M. Passoni, V.T. Tikhonchuk, M. Lontano, and V.Yu. Bychenkov. Charge separation effects in solid targets and ion acceleration with a two-temperature electron distribution. *Phys. Rev. E*, 69:026411, 2004.

[78] B.J. Albright, L. Yin, B.M. Hegelich, K.J. Bowers, T.J.T. Kwan, and J.C. Fernández. Theory of laser acceleration of light-ion beams from interaction of ultrahigh-intensity lasers with layered targets. *Phys. Rev. Lett.*, 97:115002, 2006.

[79] M. Nishiuchi, A. Fukumi, H. Daido, Z. Li, A. Sagisaka, K. Ogura, S. Orimo, M. Kado, Y. Hayashi, M. Mori, S.V. Bulanov, T. Esirkepov, K. Nemoto, Y. Oishi, T. Nayuki, T. Fujii, A. Noda,

Y. Iwashita, T. Shirai, and S. Nakamura. The laser proton acceleration in the strong charge separation regime. *Phys. Lett. A*, 357(4):339–344, 2006.

[80] M. Passoni and M. Lontano. One-dimensional model of the electrostatic ion acceleration in the ultraintense laser–solid interaction. *Laser Part. Beams*, 22(2):163–169, 2004.

[81] M. Passoni and M. Lontano. Theory of light-ion acceleration driven by a strong charge separation. *Phys. Rev. Lett.*, 101:115001, 2008.

[82] M. Lontano and M. Passoni. Electrostatic field distribution at the sharp interface between high density matter and vacuum. *Phys. Plasmas*, 13(4):042102, 2006.

[83] J. Schreiber, F. Bell, F. Grüner, U. Schramm, M. Geissler, M. Schnürer, S. Ter-Avetisyan, B. M. Hegelich, J. Cobble, E. Brambrink, J. Fuchs, P. Audebert, and D. Habs. Analytical model for ion acceleration by high-intensity laser pulses. *Phys. Rev. Lett.*, 97:045005, 2006.

[84] E. L. Clark, K. Krushelnick, J. R. Davies, M. Zepf, M. Tatarakis, F. N. Beg, A. Machacek, P. A. Norreys, M. I. K. Santala, I. Watts, and A. E. Dangor. Measurements of energetic proton transport through magnetized plasma from intense laser interactions with solids. *Phys. Rev. Lett.*, 84:670–673, 2000.

[85] A. Maksimchuk, S. Gu, K. Flippo, D. Umstadter, and V. Yu. Bychenkov. Forward ion acceleration in thin films driven by a high-intensity laser. *Phys. Rev. Lett.*, 84:4108–4111, 2000.

[86] A. Henig, S. Steinke, M. Schnürer, T. Sokollik, R. Hörlein, D. Kiefer, D. Jung, J. Schreiber, B. M. Hegelich, X. Q. Yan, J. Meyer-ter Vehn, T. Tajima, P. V. Nickles, W. Sandner, and D. Habs. Radiation-pressure acceleration of ion beams driven by circularly polarized laser pulses. *Phys. Rev. Lett.*, 103:245003, 2009.

[87] T. Schlegel, N. Naumova, V. T. Tikhonchuk, C. Labaune, I. V. Sokolov, and G. Mourou. Relativistic laser piston model: Ponderomotive ion acceleration in dense plasmas using ultraintense laser pulses. *Phys. Plasmas*, 16(8):083103, 2009.

[88] K. Nemoto, A. Maksimchuk, S. Banerjee, K. Flippo, G. Mourou, D. Umstadter, and V. Yu. Bychenkov. Laser-triggered ion acceleration and table top isotope production. *Applied Physics Letters*, 78(5):595–597, 2001.

[89] A. Henig, D. Kiefer, M. Geissler, S. G. Rykovanov, R. Ramis, R. Hörlein, J. Osterhoff, Zs. Major, L. Veisz, S. Karsch, F. Krausz, D. Habs, and J. Schreiber. Laser-driven shock acceleration of ion beams from spherical mass-limited targets. *Phys. Rev. Lett.*, 102:095002, 2009.

[90] S. Kar, M. Borghesi, S. V. Bulanov, M. H. Key, T. V. Liseykina, A. Macchi, A. J. Mackinnon, P. K. Patel, L. Romagnani, A. Schiavi, and O. Willi. Plasma jets driven by ultraintense-laser interaction with thin foils. *Phys. Rev. Lett.*, 100:225004, 2008.

[91] A.P.L. Robinson, P. Gibbon, M. Zepf, S. Kar, R.G. Evans, and C. Bellei. Relativistically correct hole-boring and ion acceleration by circularly polarized laser pulses. *Plasma Phys. Control. Fusion*, 51(2):024004, 2009.

[92] T. Schlegel, N. Naumova, V. T. Tikhonchuk, C. Labaune, I. V. Sokolov, and G. Mourou. Relativistic laser piston model: Ponderomotive ion acceleration in dense plasmas using ultraintense laser pulses. *Phys. Plasmas*, 16(8):083103, 2009.

[93] A. Macchi, F. Cattani, T.V. Liseykina, and F. Cornolti. Laser acceleration of ion bunches at the front surface of overdense plasmas. *Phys. Rev. Lett.*, 94:165003, 2005.

[94] T.V. Liseikina and A. Macchi. Features of ion acceleration by circularly polarized laser pulses. *App. Phys. Lett.*, 91(17):171502, 2007.

[95] S.S. Bulanov, A. Brantov, V.Yu. Bychenkov, V. Chvykov, G. Kalinchenko, T. Matsuoka, P. Rousseau, S. Reed, V. Yanovsky, K. Krushelnick, D.W. Litzenberg, and A. Maksimchuk. Accelerating protons to therapeutic energies with ultraintense, ultraclean, and ultrashort laser pulses. *Med. Phys.*, 35(5):1770–1776, 2008.

[96] T. Esirkepov, M. Yamagiwa, and T. Tajima. Laser ion-acceleration scaling laws seen in multiparametric particle-in-cell simulations. *Phys. Rev. Lett.*, 96:105001, 2006.

[97] K. Zeil nd S.D. Kraft, S. Bock, M. Bussmann, T.E. Cowan, T. Kluge, J. Metzkes, T. Richter, R. Sauerbrey, and U. Schramm. The scaling of proton energies in ultrashort pulse laser plasma acceleration. *New J. Phys.*, 12(4):045015, 2010.

[98] T. Esirkepov, M. Borghesi, S. V. Bulanov, G. Mourou, and T. Tajima. Highly efficient relativistic-ion generation in the laser-piston regime. *Phys. Rev. Lett.*, 92:175003, 2004.

[99] X. Zhang, B. Shen, X. Li, Z. Jin, and F. Wang. Multistaged acceleration of ions by circularly polarized laser pulse: Monoenergetic ion beam generation. *Phys. Plasmas*, 14(7):073101, 2007.

[100] O. Klimo, J. Psikal, J. Limpouch, and V.T. Tikhonchuk. Monoenergetic ion beams from ultrathin foils irradiated by ultrahigh-contrast circularly polarized laser pulses. *Phys. Rev. ST Accel. Beams*, 11:031301, 2008.

[101] A.P.L. Robinson, M. Zepf, S. Kar, R.G. Evans, and C. Bellei. Radiation pressure acceleration of thin foils with circularly polarized laser pulses. *New J. Phys.*, 10(1):013021, 2008.

[102] L.O. Silva, M. Marti, J.R. Davies, R.A. Fonseca, C. Ren, F.S. Tsung, and W.B. Mori. Proton shock acceleration in laser-plasma interactions. *Phys. Rev. Lett.*, 92:015002, 2004.

[103] D. Haberberger, S. Tochitsky, F. Fiuza, C. Gong, R.A. Fonseca, L.O. Silva, W.B. Mori, and C. Joshi. Collisionless shocks in

laser-produced plasma generate monoenergetic high-energy proton beams. *Nat. Phys.*, 8:95–99, 2012.

[104] M. Zepf, E. L. Clark, F. N. Beg, R. J. Clarke, A. E. Dangor, A. Gopal, K. Krushelnick, P. A. Norreys, M. Tatarakis, U. Wagner, and M. S. Wei. Proton acceleration from high-intensity laser interactions with thin foil targets. *Phys. Rev. Lett.*, 90:064801, 2003.

[105] E. d'Humières, E. Lefebvre, L. Gremillet, and V. Malka. Proton acceleration mechanisms in high-intensity laser interaction with thin foils. *Phys. Plasmas*, 12(6):062704, 2005.

[106] M. Chen, Z.-M. Sheng, Q.-L. Dong, M.-Q. He, Y.-T. Li, M.A. Bari, and J. Zhang. Collisionless electrostatic shock generation and ion acceleration by ultraintense laser pulses in overdense plasmas. *Phys. Plasmas*, 14(5):053102, 2007.

[107] S.P. Hatchett, C.G. Brown, T.E. Cowan, E.A. Henry, J.S. Johnson, M.H. Key, J.A. Koch, A.B. Langdon, B.F. Lasinski, R.W. Lee, A.J. Mackinnon, D.M. Pennington, M.D. Perry, T.W. Phillips, M. Roth, T.C. Sangster, M.S. Singh, R.A. Snavely, M.A. Stoyer, S.C. Wilks, and K.Yasuike. Electron, photon, and ion beams from the relativistic interaction of petawatt laser pulses with solid targets. *Phys. Plasmas*, 7(5):2076–2082, 2000.

[108] R. A. Snavely, M. H. Key, S. P. Hatchett, T. E. Cowan, M. Roth, T. W. Phillips, M. A. Stoyer, E. A. Henry, T. C. Sangster, M. S. Singh, S. C. Wilks, A. MacKinnon, A. Offenberger, D. M. Pennington, K. Yasuike, A. B. Langdon, B. F. Lasinski, J. Johnson, M. D. Perry, and E. M. Campbell. Intense high-energy proton beams from petawatt-laser irradiation of solids. *Phys. Rev. Lett.*, 85:2945–2948, 2000.

[109] A.J. Mackinnon, M. Borghesi, S. Hatchett, M.H. Key, P.K. Patel, H. Campbell, A. Schiavi, R. Snavely, S.C. Wilks, and O. Willi. Effect of plasma scale length on multi-mev proton production by intense laser pulses. *Phys. Rev. Lett.*, 86:1769–1772, 2001.

[110] J. Fuchs, Y. Sentoku, S. Karsch, J. Cobble, P. Audebert, A. Kemp, A. Nikroo, P. Antici, E. Brambrink, A. Blazevic, E. M. Campbell, J. C. Fernández, J.-C. Gauthier, M. Geissel, M. Hegelich, H. Pépin, H. Popescu, N. Renard-LeGalloudec, M. Roth, J. Schreiber, R. Stephens, and T. E. Cowan. Comparison of laser ion acceleration from the front and rear surfaces of thin foils. *Phys. Rev. Lett.*, 94:045004, 2005.

[111] Y. Sentoku, T. E. Cowan, A. Kemp, and H. Ruhl. High energy proton acceleration in interaction of short laser pulse with dense plasma target. *Physics of Plasmas*, 10(5):2009–2015, 2003.

[112] M. Borghesi, A.J. Mackinnon, D.H. Campbell, D.G. Hicks, S. Kar, P.K. Patel, D. Price, L. Romagnani, A. Schiavi, and O. Willi. Multi-mev proton source investigations in ultraintense laser-foil interactions. *Phys. Rev. Lett.*, 92:055003, 2004.

[113] M. Nishiuchi, H. Daido, A. Yogo, S. Orimo, K. Ogura, J. Ma, A. Sagisaka, M. Mori, A. S. Pirozhkov, H. Kiriyama, S. V. Bulanov, T. Zh. Esirkepov, I. W. Choi, C. M. Kim, T. M. Jeong, T. J. Yu, J. H. Sung, S. K. Lee, N. Hafz, K. H. Pae, Y.-C. Noh, D.-K. Ko, J. Lee, Y. Oishi, K. Nemoto, H. Nagatomo, K. Nagai, and H. Azuma. Efficient production of a collimated mev proton beam from a polyimide target driven by an intense femtosecond laser pulse. *Phys. Plasmas*, 15(5):053104, 2008.

[114] M. Borghesi, A.J. Mackinnon, D.H. Campbell, D.G. Hicks, S. Kar, P.K. Patel, D. Price, L. Romagnani, A. Schiavi, and O. Willi. Multi-mev proton source investigations in ultraintense laser-foil interactions. *Phys. Rev. Lett.*, 92:055003, 2004.

[115] A.J. Mackinnon, Y. Sentoku, P.K. Patel, D.W. Price, S. Hatchett, M.H. Key, C. Andersen, R. Snavely, and R.R. Freeman. Enhancement of proton acceleration by hot-electron recirculation in thin foils irradiated by ultraintense laser pulses. *Phys. Rev. Lett.*, 88:215006, 2002.

[116] T.E. Cowan, J. Fuchs, H. Ruhl, A. Kemp, P. Audebert, M. Roth, R. Stephens, I. Barton, A. Blazevic, E. Brambrink, J. Cobble, J. Fernández, J.-C. Gauthier, M. Geissel, M. Hegelich, J. Kaae, S. Karsch, G.P. Le Sage, S. Letzring, M. Manclossi, S. Meyroneinc, A. Newkirk, H. Pépin, and N. Renard-LeGalloudec. Ultralow emittance, multi-mev proton beams from a laser virtual-cathode plasma accelerator. *Phys. Rev. Lett.*, 92:204801, 2004.

[117] H. Schwoerer, S. Pfotenhauer, O. Jackel, K.-U. Amthor, B. Liesfeld, W. Ziegler, R. Sauerbrey, K.W.D. Ledingham, and T. Esirkepov. Laser-plasma acceleration of quasi-monoenergetic protons from microstructured targets. *Nature*, 439(7075):445–448, 2006.

[118] I. Prencipe, A. Sgattoni, D. Dellasega, L. Fedeli, L. Cialfi, Il.W. Choi, I.J. Kim, K.A. Janulewicz, K.F. Kakolee, H.W. Lee, J.H. Sung, S.K. Lee, C.H. Nam, and M. Passoni. Development of foam-based layered targets for laser-driven ion beam production. *Plasma Phys. Control. Fusion*, 58(3):034019, 2016.

[119] M. Passoni, A. Sgattoni, I. Prencipe, L. Fedeli, D. Dellasega, L. Cialfi, Il Woo Choi, I Jong Kim, K. A. Janulewicz, Hwang Woon Lee, Jae Hee Sung, Seong Ku Lee, and Chang Hee Nam. Toward high-energy laser-driven ion beams: Nanostructured double-layer targets. *Phys. Rev. Accel. Beams*, 19:061301, 2016.

[120] E. Fourkal, I. Velchev, and C.-M. Ma. Coulomb explosion effect and the maximum energy of protons accelerated by high-power lasers. *Phys. Rev. E*, 71:036412, 2005.

[121] K Zeil, J Metzkes, T Kluge, M Bussmann, T E Cowan, S D Kraft, R Sauerbrey, B Schmidt, M Zier, and U Schramm. Robust energy enhancement of ultrashort pulse laser accelerated protons from reduced mass targets. *Plasma Phys. Control. Fusion*, 56(8):084004, 2014.

[122] S. Kahaly, S.K. Yadav, W.M. Wang, S. Sengupta, Z.M. Sheng, A. Das, P.K. Kaw, and G.R. Kumar. Near-complete absorption of

intense, ultrashort laser light by sub-λ gratings. *Phys. Rev. Lett.*, 101:145001, 2008.

[123] O. Klimo, J. Psikal, J. Limpouch, J. Proska, F. Novotny, T. Ceccotti, V. Floquet, and S. Kawata. Short pulse laser interaction with micro-structured targets: simulations of laser absorption and ion acceleration. *New J. Phys.*, 13(5):053028, 2011.

[124] L.L. Ji, J. Snyder, A. Pukhov, R.R. Freeman, and K.U. Akli. Towards manipulating relativistic laser pulses with micro-tube plasma lenses. *Sci. Rep.*, 6:23256, 2016.

[125] M. Borghesi, D. H. Campbell, A. Schiavi, M. G. Haines, O. Willi, A. J. MacKinnon, P. Patel, L. A. Gizzi, M. Galimberti, R. J. Clarke, F. Pegoraro, H. Ruhl, and S. Bulanov. Electric field detection in laser-plasma interaction experiments via the proton imaging technique. *Phys. Plasmas*, 9(5):2214–2220, 2002.

[126] T. Sokollik, M. Schnürer, S. Ter-Avetisyan, P. V. Nickles, E. Risse, M. Kalashnikov, W. Sandner, G. Priebe, M. Amin, T. Toncian, O. Willi, and A. A. Andreev. Transient electric fields in laser plasmas observed by proton streak deflectometry. *App. Phys. Lett.*, 92(9):091503, 2008.

[127] C. A. Cecchetti, M. Borghesi, J. Fuchs, G. Schurtz, S. Kar, A. Macchi, L. Romagnani, P. A. Wilson, P. Antici, R. Jung, J. Osterholtz, C. A. Pipahl, O. Willi, A. Schiavi, M. Notley, and D. Neely. Magnetic field measurements in laser-produced plasmas via proton deflectometry. *Phys. Plasmas*, 16(4):043102, 2009.

[128] K. Quinn, P. A. Wilson, B. Ramakrishna, L. Romagnani, G. Sarri, C. A. Cecchetti, L. Lancia, J. Fuchs, A. Pipahl, T. Toncian, O. Willi, R. J. Clarke, D. Neely, M. Notley, P. Gallegos, D. C. Carroll, M. N. Quinn, X. H. Yuan, P. McKenna, and M. Borghesi. Modified proton radiography arrangement for the detection of ultrafast field fronts. *Rev. Sci. Instr.*, 80(11):113506, 2009.

[129] L. Lancia, M. Grech, S. Weber, J.-R. Marquès, L. Romagnani, M. Nakatsutsumi, P. Antici, A. Bellue, N. Bourgeois, J.-L. Feugeas, T. Grismayer, T. Lin, Ph. Nicolaï, B. Nkonga, P. Audebert, R. Kodama, V. T. Tikhonchuk, and J. Fuchs. Anomalous self-generated electrostatic fields in nanosecond laser-plasma interaction. *Phys. Plasmas*, 18(3):030705, 2011.

[130] S. Kar, M. Borghesi, C.A. Cecchetti, L. Romagnani, F. Ceccherini, T.V. Liseykina, A. Macchi, R. Jung, J. Osterholz, O. Willi, L.A. Gizzi, A. Schiavi, M. Galimberti, and R. Heathcote. Dynamics of charge-displacement channeling in intense laser–plasma interactions. *New J. Phys.*, 9(11):402, 2007.

[131] L. Romagnani, S. V. Bulanov, M. Borghesi, P. Audebert, J. C. Gauthier, K. Löwenbrück, A. J. Mackinnon, P. Patel, G. Pretzler, T. Toncian, and O. Willi. Observation of collisionless shocks in laser-plasma experiments. *Phys. Rev. Lett.*, 101:025004, 2008.

[132] K. Quinn, P. A. Wilson, C. A. Cecchetti, B. Ramakrishna, L. Romagnani, G. Sarri, L. Lancia, J. Fuchs, A. Pipahl, T. Toncian, O. Willi, R. J. Clarke, D. Neely, M. Notley, P. Gallegos, D. C. Carroll, M. N. Quinn, X. H. Yuan, P. McKenna, T. V. Liseykina, A. Macchi, and M. Borghesi. Laser-driven ultrafast field propagation on solid surfaces. *Phys. Rev. Lett.*, 102:194801, 2009.

[133] L. Willingale, A. G. R. Thomas, P. M. Nilson, M. C. Kaluza, S. Bandyopadhyay, A. E. Dangor, R. G. Evans, P. Fernandes, M. G. Haines, C. Kamperidis, R. J. Kingham, S. Minardi, M. Notley, C. P. Ridgers, W. Rozmus, M. Sherlock, M. Tatarakis, M. S. Wei, Z. Najmudin, and K. Krushelnick. Fast advection of magnetic fields by hot electrons. *Phys. Rev. Lett.*, 105:095001, 2010.

[134] J. A. Cobble, R. P. Johnson, T. E. Cowan, N. Renard-Le Galloudec, and M. Allen. High resolution laser-driven proton radiography. *J. App. Phys.*, 92(4):1775–1779, 2002.

[135] A. Ravasio, L. Romagnani, S. Le Pape, A. Benuzzi-Mounaix, C. Cecchetti, D. Batani, T. Boehly, M. Borghesi, R. Dezulian,

L. Gremillet, E. Henry, D. Hicks, B. Loupias, A. MacKinnon, N. Ozaki, H. S. Park, P. Patel, A. Schiavi, T. Vinci, R. Clarke, M. Notley, S. Bandyopadhyay, and M. Koenig. Proton radiography of a shock-compressed target. *Phys. Rev. E*, 82:016407, 2010.

[136] G. Sarri, C. A. Cecchetti, R. Jung, P. Hobbs, S. James, J. Lockyear, R. M. Stevenson, D. Doria, D. J. Hoarty, O. Willi, and M. Borghesi. Spatially resolved measurements of laser filamentation in long scale length underdense plasmas with and without beam smoothing. *Phys. Rev. Lett.*, 106:095001, 2011.

[137] G. Sarri, M. E. Dieckmann, C. R. D. Brown, C. A. Cecchetti, D. J. Hoarty, S. F. James, R. Jung, I. Kourakis, H. Schamel, O. Willi, and M. Borghesi. Observation and characterization of laser-driven phase space electron holes. *Phys. Plasmas*, 17(1):010701, 2010.

[138] M. Borghesi, S. Bulanov, D. H. Campbell, R. J. Clarke, T. Zh. Esirkepov, M. Galimberti, L. A. Gizzi, A. J. MacKinnon, N. M. Naumova, F. Pegoraro, H. Ruhl, A. Schiavi, and O. Willi. Macroscopic evidence of soliton formation in multiterawatt laser-plasma interaction. *Phys. Rev. Lett.*, 88:135002, 2002.

[139] M. Borghesi, A. Schiavi, D.H. Campbell, M.G. Haines, O. Willi, A.J. MacKinnon, L.A. Gizzi, M. Galimberti, R.J. Clarke, and H. Ruhl. Proton imaging: a diagnostic for inertial confinement fusion/fast ignitor studies. *Plasma Phys. Control. Fusion*, 43(12A):A267, 2001.

[140] A. J. Mackinnon, P. K. Patel, M. Borghesi, R. C. Clarke, R. R. Freeman, H. Habara, S. P. Hatchett, D. Hey, D. G. Hicks, S. Kar, M. H. Key, J. A. King, K. Lancaster, D. Neely, A. Nikkro, P. A. Norreys, M. M. Notley, T. W. Phillips, L. Romagnani, R. A. Snavely, R. B. Stephens, and R. P. J. Town. Proton radiography of a laser-driven implosion. *Phys. Rev. Lett.*, 97:045001, 2006.

[141] G. Sarri, C.A. Cecchetti, L. Romagnani, C.M. Brown, D.J. Hoarty, S. James, J. Morton, M.E. Dieckmann, R. Jung, O. Willi, S.V.

Bulanov, F. Pegoraro, and M. Borghesi. The application of laser-driven proton beams to the radiography of intense laser–hohlraum interactions. *New J. Phys.*, 12(4):045006, 2010.

[142] S.V. Bulanov and V.S. Khoroshkov. Feasibility of using laser ion accelerators in proton therapy. *Plasma Phys. Rep.*, 28(5):453–456, 2002.

[143] A. Yogo, K. Sato, M. Nishikino, M. Mori, T. Teshima, H. Numasaki, M. Murakami, Y. Demizu, S. Akagi, S. Nagayama, K. Ogura, A. Sagisaka, S. Orimo, M. Nishiuchi, A. S. Pirozhkov, M. Ikegami, M. Tampo, H. Sakaki, M. Suzuki, I. Daito, Y. Oishi, H. Sugiyama, H. Kiriyama, H. Okada, S. Kanazawa, S. Kondo, T. Shimomura, Y. Nakai, M. Tanoue, H. Sasao, D. Wakai, P. R. Bolton, and H. Daido. Application of laser-accelerated protons to the demonstration of dna double-strand breaks in human cancer cells. *App. Phys. Lett.*, 94(18):181502, 2009.

[144] A. Yogo, T. Maeda, T. Hori, H. Sakaki, K. Ogura, M. Nishiuchi, A. Sagisaka, H. Kiriyama, H. Okada, S. Kanazawa, T. Shimomura, Y. Nakai, M. Tanoue, F. Sasao, P. R. Bolton, M. Murakami, T. Nomura, S. Kawanishi, and K. Kondo. Measurement of relative biological effectiveness of protons in human cancer cells using a laser-driven quasimonoenergetic proton beamline. *App. Phys. Lett.*, 98(5):053701, 2011.

[145] S.V. Bulanov, T.Zh. Esirkepov, V.S. Khoroshkov, A.V. Kuznetsov, and F. Pegoraro. Oncological hadrontherapy with laser ion accelerators. *Phys. Lett. A*, 299(2):240–247, 2002.

[146] E. Fourkal, J.S. Li, W. Xiong, A. Nahum, and C.-M. Ma. Intensity modulated radiation therapy using laser-accelerated protons: a monte carlo dosimetric study. *Phys. Med. Biol.*, 48(24):3977, 2003.

[147] W Luo, J Li, E Fourkal, J Fan, X Xu, Z Chen, L Jin, R Price, and C-M Ma. Dosimetric advantages of impt over imrt for laser-accelerated proton beams. *Phys. Med. Biol.*, 53(24):7151, 2008.

[148] S. Schell and J.J. Wilkens. Advanced treatment planning methods for efficient radiation therapy with laser accelerated proton and ion beams. *Med. Phys.*, 37(10):5330–5340, 2010.

[149] E. Fourkal, I. Velchev, J. Fan, W. Luo, and C.-M. Ma. Energy optimization procedure for treatment planning with laser-accelerated protons. *Med. Phys.*, 34(2):577–584, 2007.

[150] V. Malka, S. Fritzler, E. Lefebvre, E. d'Humières, R. Ferrand, G. Grillon, C. Albaret, S. Meyroneinc, J.-P. Chambaret, A. Antonetti, and D. Hulin. Practicability of protontherapy using compact laser systems. *Med. Phys.*, 31(6):1587–1592, 2004.

[151] S. Fritzler, V. Malka, G. Grillon, J. P. Rousseau, F. Burgy, E. Lefebvre, E. d'Humières, P. McKenna, and K. W. D. Ledingham. Proton beams generated with high-intensity lasers: Applications to medical isotope production. *App. Phys. Lett.*, 83(15):3039–3041, 2003.

[152] E. Lefebvre, E. d'Humières, S. Fritzler, and V. Malka. Numerical simulation of isotope production for positron emission tomography with laser-accelerated ions. *J. App. Phys.*, 100(11):113308, 2006.

[153] M. Fujimoto, K. Matsukado, H. Takahashi, Y. Kawada, and S. Ohsuka. Repetitive production of positron emitters using deuterons accelerated by multiterawatt laser pulses. *Rev. Sci. Instr.*, 80(11):113301, 2009.

[154] S. Atzeni and J. Meyer ter Vehn. *The Physics of Inertial Fusion: Beam Plasma Interaction, Hydrodynamics, Hot Dense Matter*. Oxford University Press, 2009.

[155] V.Yu. Bychenkov, W. Rozmus, A. Maksimchuk, D. Umstadter, and C. E. Capjack. Fast ignitor concept with light ions. *Plasma Phys. Rep.*, 27(12):1017–1020, 2001.

[156] M. Temporal, J.J. Honrubia, and S. Atzeni. Numerical study of fast ignition of ablatively imploded deuterium–tritium fusion

capsules by ultra-intense proton beams. *Phys. Plasmas*, 9(7):3098–3107, 2002.

[157] M.H. Key. Status of and prospects for the fast ignition inertial fusion concept. *Phys. Plasmas*, 14(5):055502, 2007.

[158] S. Atzeni, M. Temporal, and J.J. Honrubia. A first analysis of fast ignition of precompressed icf fuel by laser-accelerated protons. *Nucl. Fusion*, 42(3):L1, 2002.

[159] M. Roth, T. E. Cowan, M. H. Key, S. P. Hatchett, C. Brown, W. Fountain, J. Johnson, D. M. Pennington, R. A. Snavely, S. C. Wilks, K. Yasuike, H. Ruhl, F. Pegoraro, S. V. Bulanov, E. M. Campbell, M. D. Perry, and H. Powell. Fast ignition by intense laser-accelerated proton beams. *Phys. Rev. Lett.*, 86:436–439, 2001.

[160] N. Naumova, T. Schlegel, V. T. Tikhonchuk, C. Labaune, I. V. Sokolov, and G. Mourou. Hole boring in a dt pellet and fast-ion ignition with ultraintense laser pulses. *Phys. Rev. Lett.*, 102:025002, 2009.

[161] V.T. Tikhonchuk, T. Schlegel, C. Regan, M. Temporal, J.-L. Feugeas, Ph. Nicolaï, and X. Ribeyre. Fast ion ignition with ultra-intense laser pulses. *Nucl. Fusion*, 50(4):045003, 2010.

[162] M. Roth, I. Alber, V. Bagnoud, C.R.D. Brown, R. Clarke, H. Daido, J. Fernandez, K. Flippo, S. Gaillard, C. Gauthier, M. Geissel, S. Glenzer, G. Gregori, M. Günther, K. Harres, R. Heathcote, A. Kritcher, N. Kugland, S. LePape, B. Li, M. Makita, J. Mithen, C. Niemann, F. Nürnberg, D. Offermann, A. Otten, A. Pelka, D. Riley, G. Schaumann, M. Schollmeier, J. Schütrumpf, M. Tampo, A. Tauschwitz, and A. Tauschwitz. Proton acceleration experiments and warm dense matter research using high power lasers. *Plasma Phys. and Control. Fusion*, 51(12):124039, 2009.

[163] A. Mancic, J. Robiche, P. Antici, P. Audebert, C. Blancard, P. Combis, F. Dorchies, G. Faussurier, S. Fourmaux, M. Harmand, R. Kodama, L. Lancia, S. Mazevet, M. Nakatsutsumi, O. Peyrusse, V. Recoules, P. Renaudin, R. Shepherd, and J. Fuchs. Isochoric heating of solids by laser-accelerated protons: Experimental characterization and self-consistent hydrodynamic modeling. *High En. Dens. Phys.*, 6(1):21–28, 2010.

[164] P. K. Patel, A. J. Mackinnon, M. H. Key, T. E. Cowan, M. E. Foord, M. Allen, D. F. Price, H. Ruhl, P. T. Springer, and R. Stephens. Isochoric heating of solid-density matter with an ultrafast proton beam. *Phys. Rev. Lett.*, 91:125004, 2003.

[165] G. M. Dyer, A. C. Bernstein, B. I. Cho, J. Osterholz, W. Grigsby, A. Dalton, R. Shepherd, Y. Ping, H. Chen, K. Widmann, and T. Ditmire. Equation-of-state measurement of dense plasmas heated with fast protons. *Phys. Rev. Lett.*, 101:015002, 2008.

[166] A. Pelka, G. Gregori, D. O. Gericke, J. Vorberger, S. H. Glenzer, M. M. Günther, K. Harres, R. Heathcote, A. L. Kritcher, N. L. Kugland, B. Li, M. Makita, J. Mithen, D. Neely, C. Niemann, A. Otten, D. Riley, G. Schaumann, M. Schollmeier, An. Tauschwitz, and M. Roth. Ultrafast melting of carbon induced by intense proton beams. *Phys. Rev. Lett.*, 105:265701, 2010.

[167] C. Toupin, E. Lefebvre, and G. Bonnaud. Neutron emission from a deuterated solid target irradiated by an ultraintense laser pulse. *Phys. Plasmas*, 8(3):1011–1021, 2001.

[168] P. McKenna, K. W. D. Ledingham, S. Shimizu, J. M. Yang, L. Robson, T. McCanny, J. Galy, J. Magill, R. J. Clarke, D. Neely, P. A. Norreys, R. P. Singhal, K. Krushelnick, and M. S. Wei. Broad energy spectrum of laser-accelerated protons for spallation-related physics. *Phys. Rev. Lett.*, 94:084801, 2005.

[169] J. M. Yang, P. McKenna, K. W. D. Ledingham, T. McCanny, L. Robson, S. Shimizu, R. P. Singhal, M. S. Wei, K. Krushelnick,

R. J. Clarke, D. Neely, and P. A. Norreys. Neutron production by fast protons from ultraintense laser-plasma interactions. *J. App. Phys.*, 96(11):6912–6918, 2004.

[170] P. McKenna, K. W. D. Ledingham, J. M. Yang, L. Robson, T. McCanny, S. Shimizu, R. J. Clarke, D. Neely, K. Spohr, R. Chapman, R. P. Singhal, K. Krushelnick, M. S. Wei, and P. A. Norreys. Characterization of proton and heavier ion acceleration in ultrahigh-intensity laser interactions with heated target foils. *Phys. Rev. E*, 70:036405, 2004.

[171] P. McKenna, K. W. D. Ledingham, T. McCanny, R. P. Singhal, I. Spencer, M. I. K. Santala, F. N. Beg, K. Krushelnick, M. Tatarakis, M. S. Wei, E. L. Clark, R. J. Clarke, K. L. Lancaster, P. A. Norreys, K. Spohr, R. Chapman, and M. Zepf. Demonstration of fusion-evaporation and direct-interaction nuclear reactions using high-intensity laser-plasma-accelerated ion beams. *Phys. Rev. Lett.*, 91:075006, 2003.

[172] A. Macchi. A femtosecond neutron source. *App. Phys. B*, 82(3):337–340, 2006.

[173] K.W.D Ledingham and W. Galster. Laser-driven particle and photon beams and some applications. *New J. Phys.*, 12(4):045005, 2010.

[174] V. Yu. Bychenkov, Y. Sentoku, S. V. Bulanov, K. Mima, G. Mourou, and S. V. Tolokonnikov. Pion production under the action of intense ultrashort laser pulse on a solid target. *J. Exp. Th. Phys. Lett.*, 74(12):586–589, 2001.

[175] S.V. Bulanov, T. Esirkepov, P. Migliozzi, F. Pegoraro, T. Tajima, and F. Terranova. Neutrino oscillation studies with laser-driven beam dump facilities. *Nucl. Instr. Meth. Phys. Res. A*, 540(1):25–41, 2005.

[176] A.V. Pakhomov. Neutrino generation by high-intensity lasers. *J. Phys. G*, 28(6):1469, 2002.

[177] R. W. Hockney and J. W. Eastwood. *Computer simulation using particles*. Tailor & Francis, 1988.

[178] C. K. Birdsall and A. B. Langdon. *Plasma physics via computer simulation*. IOP Publishing, 1991.

[179] N. B. Delone and V. P. Krainov. Tunneling and barrier-suppression ionization of atoms and ions in a laser radiation field. *Phys. Usp.*, 41(5):469, 1998.

[180] M. B. Smirnov and V. P. Krainov. Ionization of cluster atoms in a strong laser field. *Phys. Rev. A*, 69:043201, 2004.

[181] V. P. Krainov. Ionization rates and energy and angular distributions at the barrier-suppression ionization of complex atoms and atomic ions. *J. Opt. Soc. Am. B*, 14(2):425–431, 1997.

[182] V. P. Krainov. Theory of barrier-suppression ionization of atoms. *J. Nonlinear Optic. Phys. Mat.*, 4:775, 1994.

[183] S. Augst, D. D. Meyerhofer, D. Strickland, and S. L. Chin. Laser ionization of noble gases by coulomb-barrier suppression. *J. Opt. Soc. Am. B*, 8(4):858–867, 1991.

[184] R. FitzPatrick. *Plasma Physics: An Introduction*. CRC Press, 2014.

[185] J. Villasenor and O. Buneman. Rigorous charge conservation for local electromagnetic field solvers. *Comp. Phys. Comm.*, 69(2):306–316, 1992.

[186] K. Yee. Numerical solution of initial boundary value problems involving maxwell's equations in isotropic media. *IEEE Trans. Ant. Prop.*, 14(3):302–307, 1966.

[187] J. P. Boris. Relativistic plasma simulation-optimization of a hybrid code. *Proc. 4th Conf. Num. Sim. Plasmas*, pages 3–67, 1970.

[188] R. A. Fonseca, L. O. Silva, F. S. Tsung, V. K. Decyk, W. Lu, C. Ren, W. B. Mori, S. Deng, S. Lee, T. Katsouleas, and J. C. Adam. *OSIRIS: A Three-Dimensional, Fully Relativistic Particle in Cell Code for Modeling Plasma Based Accelerators*, pages 342–351. Springer Berlin Heidelberg, Berlin, Heidelberg, 2002.

[189] R A Fonseca, J Vieira, F Fiuza, A Davidson, F S Tsung, W B Mori, and L O Silva. Exploiting multi-scale parallelism for large scale numerical modelling of laser wakefield accelerators. *Plasma Phys. Control. Fusion*, 55(12):124011, 2013.

[190] R A Fonseca, S F Martins, L O Silva, J W Tonge, F S Tsung, and W B Mori. One-to-one direct modeling of experiments and astrophysical scenarios: pushing the envelope on kinetic plasma simulations. *Plasma Phys. Control. Fusion*, 50(12):124034, 2008.

[191] S. Bastrakov, R. Donchenko, A. Gonoskov, E. Efimenko, A. Malyshev, Meyerov. I., and I. Surmin. Particle-in-cell plasma simulation on heterogeneous cluster systems. *J. Comput. Sci.*, 3(6):474–479, 2012.

[192] I.A. Surmin, S.I. Bastrakov, E.S. Efimenko, A.A. Gonoskov, A.V. Korzhimanov, and I.B. Meyerov. Particle-in-cell laser-plasma simulation on xeon phi coprocessors. *Comp. Phys. Comm.*, 202:204–210, may 2016.

[193] J. E. Allen and M. Perego. On the ion front of a plasma expanding into a vacuum. *Phys. Plasmas*, 21(3):3–6, 2014.

[194] S. Le Pape, Y. Y. Tsui, A. Macphee, D.l Hey, P. Patel, A. Mackinnon, M. Key, M. Wei, T. Ma, F. N. Beg, R. Stephens, K. Akli, T. Link, L. Van-Woerkom, and R. R. Freeman. Characterization of the preformed plasma for high-intensity laser-plasma interaction. *Opt. lett.*, 34:2997–2999, 2009.

[195] K. Adumi, K. A. Tanaka, T. Matsuoka, T. Kurahashi, T. Yabuuchi, Y. Kitagawa, R. Kodama, K. Sawai, K. Suzuki, K. Okabe, T. Sera,

T. Norimatsu, and Y. Izawa. Characterization of preplasma produced by an ultrahigh intensity laser system. *Phys. Plasmas*, 11:3721–3725, 2004.

[196] A. Bourdier. Oblique incidence of a strong electromagnetic wave on a cold inhomogeneous electron plasma. relativistic effects. *Phys. Fluids*, 26(7):1804, 1983.

[197] A. L. Cavalieri, N. Müller, Th. Uphues, V. S. Yakovlev, A. Baltuška, B. Horvath, B. Schmidt, L. Blümel, R. Holzwarth, S. Hendel, M. Drescher, U. Kleineberg, P. M. Echenique, R. Kienberger, F. Krausz, and U. Heinzmann. Attosecond spectroscopy in condensed matter. *Nature*, 449:1029, 2007.

[198] M. Uiberacker, Th. Uphues, M. Schultze, A. J. Verhoef, V. Yakovlev, M. F. Kling, J. Rauschenberger, N. M. Kabachnik, H. Schröder, M. Lezius, K. L. Kompa, H.-G. Muller, M. J. J. Vrakking, S. Hendel, U. Kleineberg, U. Heinzmann, M. Drescher, and F. Krausz. Attosecond real-time observation of electron tunnelling in atoms. *Nature*, 446:627, 2007.

[199] G. Sansone, E. Benedetti, F. Calegari, C. Vozzi, L. Avaldi, R. Flammini, L. Poletto, P. Villoresi, C. Altucci, R. Velotta, S. Stagira, S. De Silvestri, and M. Nisoli. Isolated single-cycle attosecond pulses. *Science*, 314(5798):443–446, 2006.

[200] F. Cambronero-López, M. Blanco, C. Ruiz, M. T. Flores-Arias, and C. Bao-Varela. Polarization gating using cross-polarized wave generation with multicycle lasers to produce isolated attosecond pulses in overdense media. *J. Opt. Soc. Am. B*, 34(4):843–849, 2017.

[201] M. Blanco and M.T. Flores-Arias. Frequency gating to isolate single attosecond pulses with overdense plasmas using particle-in-cell simulations. *Opt. Express*, 25(12):13372–13381, 2017.

[202] I J Sola, E. Mével, L Elouga, E Constant, V Strelkov, L Poletto, P Villoresi, E Benedetti, J.-P. Caumes, S Stagira, C Vozzi, G Sansone, and M Nisoli. Controlling attosecond electron dynamics by phase-stabilized polarization gating. *Nature Physics*, 2(5):319–322, 2006.

[203] J. J. Carrera, X. M. Tong, and S. I. Chu. Creation and control of a single coherent attosecond xuv pulse by few-cycle intense laser pulses. *Physical Review A - Atomic, Molecular, and Optical Physics*, 74(2):1–7, 2006.

[204] G. Sansone, E. Benedetti, J. P. Caumes, S. Stagira, C. Vozzi, M. Nisoli, L. Poletto, P. Villoresi, V. Strelkov, I. Sola, L. B. Elouga, A. Za??r, E. M??vel, and E. Constant. Shaping of attosecond pulses by phase-stabilized polarization gating. *Physical Review A - Atomic, Molecular, and Optical Physics*, 80(6):1–8, 2009.

[205] N. Minkovski, S. M. Saltiel, G. I. Petrov, O. Albert, and J. Etchepare. Polarization rotation induced by cascaded third-order processes. *Opt. Lett.*, 27(22):2025–2027, 2002.

[206] F. Cambronero-López, C. Bao-Varela, and C. Ruiz. Spatiotemporal polarization pattern obtained by interference in a single cross-polarized wave-generation crystal. *J. Opt. Soc. Am. B*, 33(8):1740–1748, 2016.

[207] L. Canova, S. Kourtev, N. Minkovski, A. Jullien, R. Lopez-Martens, O. Albert, and S. M. Saltiel. Efficient generation of cross-polarized femtosecond pulses in cubic crystals with holographic cut orientation. *Applied Physics Letters*, 92(23):231102, 2008.

[208] T. Pfeifer, L. Gallmann, M. J. Abel, P. M. Nagel, D. M. Neumark, and S. R. Leone. Heterodyne mixing of laser fields for temporal gating of high-order harmonic generation. *Phys. Rev. Lett.*, 97:163901, 2006.

[209] H. Merdji, T. Auguste, W. Boutu, J.-P. Caumes, B. Carré, T. Pfeifer, A. Jullien, D. M. Neumark, and S. R. Leone. Isolated attosecond pulses using a detuned second-harmonic field. *Opt. Lett.*, 32(21):3134–3136, 2007.

[210] E. J. Takahashi, P. Lan, O. D. Mücke, Y. Nabekawa, and K. Midorikawa. Infrared two-color multicycle laser field synthesis for generating an intense attosecond pulse. *Phys. Rev. Lett.*, 104:233901, 2010.

[211] E. J. Takahashi, P. Lan, O. D. Mücke, Y. Nabekawa, and K. Midorikawa. Attosecond nonlinear optics using gigawatt-scale isolated attosecond pulses. *Nat. Comm.*, 4:2691, 2013.

[212] S. Haessler anf T. Balčiūnas, G. Fan, L. E. Chipperfield, and A. Baltuška. Enhanced multi-colour gating for the generation of high-power isolated attosecond pulses. *Sci. Rep.*, 5:10084, 2015.

[213] M. R. Edwards, V. T. Platonenko, and J. M. Mikhailova. Enhanced attosecond bursts of relativistic high-order harmonics driven by two-color fields. *Opt. Lett.*, 39(24):6823–6826, 2014.

[214] S. Mirzanejad and M. Salehi. Two-color high-order-harmonic generation: Relativistic mirror effects and attosecond pulses. *Phys. Rev. A*, 87:063815, 2013.

[215] S.-Y. Xu, M. Neupane, C. Liu, D. Zhang, A. Richardella, L. Andrew Wray, N. Alidoust, M. Leandersson, T. Balasubramanian, J. Sánchez-Barriga, O. Rader, G. Landolt, B. Slomski, J. Hugo Dil, J. Osterwalder, T.-R. Chang, H.-T. Jeng, H. Lin, A. Bansil, N. Samarth, and M. Zahid Hasan. Hedgehog spin texture and Berry's phase tuning in a magnetic topological insulator. *Nat. Phys.*, 8:616–622, 2012.

[216] I. Gierz, M. Lindroos, H. Höchst, C. R. Ast, and K. Kern. Graphene sublattice symmetry and isospin determined by circular dichroism in angle-resolved photoemission spectroscopy. *Nano Lett.*, 12(8):3900–3904, 2012.

[217] Y. Liu, G. Bian, T. Miller, and T.-C. Chiang. Visualizing electronic chirality and berry phases in graphene systems using photoemission with circularly polarized light. *Phys. Rev. Lett.*, 107:166803, 2011.

[218] G. Schütz, M. Knülle, and H. Ebert. Magnetic circular x-ray dichroism and its relation to local moments. *Phys. Scripta*, 49:302–306, 1993.

[219] T. Fan, P. Grychtol, R. Knut, C. Hernández-García, D. D. Hickstein, D. Zusin, C. Gentry, F. J. Dollar, C. A. Mancuso, C. W. Hogle, O. Kfir, D. Legut, K. Carva, J. L. Ellis, K. M. Dorney, C. Chen, O. G. Shpyrko, E. E. Fullerton, O. Cohen, P. M. Oppeneer, D. B. Milošević, A. Becker, A. A. Jaroń-Becker, T. Popmintchev, M. M. Murnane, and H. C. Kapteyn. Bright circularly polarized soft x-ray high harmonics for x-ray magnetic circular dichroism. *Proc. Natl. Acad. Sci.*, 112(46):14206–14211, 2015.

[220] D. B. Milošević and W. Becker. Attosecond pulse trains with unusual nonlinear polarization. *Phys. Rev. A*, 62:011403, 2000.

[221] D. D. Hickstein, F. J. Dollar, P. Grychtol, J. L. Ellis, R. Knut, C. Hernández-García, D. Zusin, C. Gentry, J. M. Shaw, T. Fan, K. M. Dorney, A. Becker, A. Jaroń-Becker, H. C. Kapteyn, M. M. Murnane, and C. G. Durfee. Non-collinear generation of angularly isolated circularly polarized high harmonics. *Nat. Photon.*, 9:743–750, 2015.

[222] C. Hernández-García, C. G. Durfee, D. D. Hickstein, T. Popmintchev, A. Meier, M. M. Murnane, H. C. Kapteyn, I. J. Sola, A. Jaron-Becker, and A. Becker. Schemes for generation of isolated attosecond pulses of pure circular polarization. *Phys. Rev. A*, 93:043855, 2016.

[223] M. Blanco, M. T. Flores-Arias, and A. Gonoskov. Controlling the ellipticity of attosecond pulses generated in the non-mirror regime of laser-plasma interaction. *arXiv:1706.04785*, 2018 (under revision).

[224] M. Blanco, M. T. Flores-Arias, C. Ruiz, and M. Vranic. Table-top laser-based proton acceleration in nanostructured targets. *New J. Phys.*, 19(3):033004, 2017.

[225] E. d'Humières, A. Brantov, V. Yu. Bychenkov, and V. T. Tikhonchuk. Optimization of laser-target interaction for proton acceleration. *Phys. Plasmas*, 20(2):023103, 2013.

[226] A. Sgattoni, P. Londrillo, A. Macchi, and M. Passoni. Laser ion acceleration using a solid target coupled with a low-density layer. *Phys. Rev. E*, 85:036405, 2012.

[227] M. Passoni, C. Perego, A. Sgattoni, and D. Batani. Advances in target normal sheath acceleration theory. *Physics of Plasmas*, 20(6):060701, 2013.

[228] L.A. Gizzi, C. Altana, F. Brandi, P. Cirrone, G. Cristoforetti, A. Fazzi, P. Ferrara, L. Fulgentini, D. Giove, P. Koester, L. Labate, G. Lanzalone, P. Londrillo, D. Mascali, A. Muoio, D. Palla, F. Schillaci, S. Sinigardi, S. Tudisco, and G. Turchetti. Role of laser contrast and foil thickness in target normal sheath acceleration. *Nucl. Instr. Meth. Phys. Res. Sec. A*, 829:144–148, 2016.

[229] Lu Jianxin, Lan Xiaofei, Xi Xiaofeng, Zhang Haifeng, Zhang Ji, Wang Leijian, Tang Xiuzhang, and Wang Naiyan. Effect of foil target thickness in proton acceleration driven by an ultra-short laser. *Plasma Sci. Tech.*, 17(6):458, 2015.

[230] J. S. Green, A. P. L. Robinson, N. Booth, D. C. Carroll, R. J. Dance, R. J. Gray, D. A. MacLellan, P. McKenna, C. D. Murphy, D. Rusby, and L. Wilson. High efficiency proton beam generation through target thickness control in femtosecond laser-plasma interactions. *Appl. Phys. Lett.*, 104(21):214101, 2014.

[231] C. McGuffey, A. Raymond, T. Batson, R. Hua, G. M. Petrov, J. Kim, C. M. Krauland, A. Maksimchuk, A. G. R. Thomas,

V. Yanovsky, K. Krushelnick, and F. N. Beg. Acceleration of high charge-state target ions in high-intensity laser interactions with sub-micron targets. *New J. Phys.*, 18(11):113032, 2016.

[232] M. Kaluza, J. Schreiber, M. I. K. Santala, G. D. Tsakiris, K. Eidmann, J. Meyer-ter Vehn, and K. J. Witte. Influence of the laser prepulse on proton acceleration in thin-foil experiments. *Phys. Rev. Lett.*, 93:045003, 2004.

[233] P. L. Poole, L. Obst, G. E. Cochran, J. Metzkes, H.-P. Schlenvoigt, I. Prencipe, T. Kluge, T. Cowan, U. Schramm, D. W. Schumacher, and K. Zeil. Laser-driven ion acceleration via target normal sheath acceleration in the relativistic transparency regime. *New J. Phys.*, 20(1):013019, 2018.

[234] D. K. Kuri, N. Das, and K. Patel. Role of target thickness in proton acceleration from near-critical mass-limited plasmas. *Appl. Phys. B*, 123(7), 2017.

[235] A. Sgattoni, T. Ceccotti, V. Floquet, A. Bigongiari, M. Raynaud, C. Riconda, F. Baffigi, L. Labate, L. A. Gizzi, L. Vassura, J. Fuchs, O. Klimo, M. Kveton, F. Novotny, M. Possolt, J. Prokupek, J. Proska, J. Psikal, L. Stolcova, A. Velyhan, M. Bougeard, P. Martin, I. Prencipe, A. Zani, D. Dellasega, A. Macchi, and M. Passoni. Laser plasma proton acceleration experiments using foam-covered and grating targets. *Proc. SPIE*, 8779:87790L–87790L–7, 2013.

[236] S. Zheng-Ming, W. Su-Ming, Y. Lu-Le, W. Wei-Min, C. Yun-Qian, C. Min, and Z. Jie. Absorption of ultrashort intense lasers in laser–solid interactions. *Chin. Phys. B*, 24(1):015201, 2015.

[237] A. Bigongiari, M. Raynaud, C. Riconda, A. Héron, and A. Macchi. Efficient laser-overdense plasma coupling via surface plasma waves and steady magnetic field generation. *Phys. Plasmas*, 18(10):102701, 2011.

[238] M. Raynaud, J. Kupersztych, C. Riconda, J. C. Adam, and A. Héron. Strongly enhanced laser absorption and electron acceleration via resonant excitation of surface plasma waves. *Phys. Plasmas*, 14(9):092702, 2007.

[239] A. Andreev and K. Platonov. Interaction of ultra high intensity laser pulse with structured target and fast particle generation in a stable mode. *Contrib. Plasma Phys.*, 53(2):173–178, 2013.

[240] A. Andreev, K. Platonov, J. Braenzel, A. Lubcke, S. Das, H. Messaoudi, R. Grunwald, C. Gray, E. McGlynn, and M. Schnurer. Relativistic laser nano-plasmonics for effective fast particle production. *Plasma Phys. Control. Fusion*, 58(1):014038, 2016.

[241] D. Margarone, I. J. Kim, J. Psikal, J. Kaufman, T. Mocek, I. W. Choi, L. Stolcova, J. Proska, A. Choukourov, I. Melnichuk, O. Klimo, J. Limpouch, J. H. Sung, S. K. Lee, G. Korn, and T. M. Jeong. Laser-driven high-energy proton beam with homogeneous spatial profile from a nanosphere target. *Phys. Rev. STAB*, 18:071304, 2015.

[242] A. Andreev, N. Kumar, K. Platonov, and A. Pukhov. Efficient generation of fast ions from surface modulated nanostructure targets irradiated by high intensity short-pulse lasers. *Phys. Plasmas*, 18(10):103103, 2011.

[243] D. Margarone, O. Klimo, I. J. Kim, J. Prokůpek, J. Limpouch, T. M. Jeong, T. Mocek, J. Pšikal, H. T. Kim, J. Proška, K. H Nam, L. Štolcová, I. W. Choi, S. K. Lee, J. H. Sung, T. J. Yu, and G. Korn. Laser-driven proton acceleration enhancement by nanostructured foils. *Phys. Rev. Lett.*, 109:234801, 2012.

[244] A. Zigler, S. Eisenman, M. Botton, E. Nahum, E. Schleifer, A. Baspaly, I. Pomerantz, F. Abicht, J. Branzel, G. Priebe, S. Steinke, A. Andreev, M. Schnuerer, W. Sandner, D. Gordon, P. Sprangle, and K. W. D. Ledingham. Enhanced proton acceleration by an ultrashort laser interaction with structured dynamic plasma targets. *Phys. Rev. Lett.*, 110:215004, 2013.

[245] A. Brantov and V. Bychenkov. Laser-triggered proton acceleration from micro-structured thin targets. *Contrib. Plasma Phys.*, 53(10):731–735, 2013.

[246] M. Dalui, W.-M. Wang, T. M. Trivikram, S. Sarkar, S. Tata, J. Jha, P. Ayyub, Z. M. Sheng, and M. Krishnamurthy. Preferential enhancement of laser-driven carbon ion acceleration from optimized nanostructured surfaces. *Sci. Rep.*, 5:11930 EP, 2015.

[247] A. Zigler, T. Palchan, N. Bruner, E. Schleifer, S. Eisenmann, M. Botton, Z. Henis, S. A. Pikuz, A. Y. Faenov, D. Gordon, and P. Sprangle. 5.5-7.5 mev proton generation by a moderate-intensity ultrashort-pulse laser interaction with H_2O nanowire targets. *Phys. Rev. Lett.*, 106:134801, 2011.

[248] A. Bigongiari, M. Raynaud, C. Riconda, and A. Héron. Improved ion acceleration via laser surface plasma waves excitation. *Phys. Plasmas*, 20(5):052701, 2013.

[249] T. Ceccotti, V. Floquet, A. Sgattoni, A. Bigongiari, O. Klimo, M. Raynaud, C. Riconda, A. Heron, F. Baffigi, L. Labate, L. A. Gizzi, L. Vassura, J. Fuchs, M. Passoni, M. Květon, F. Novotny, M. Possolt, J. Prokůpek, J. Proška, J. Pšikal, L. Štolcová, A. Velyhan, M. Bougeard, P. D'Oliveira, O. Tcherbakoff, F. Réau, P. Martin, and A. Macchi. Evidence of resonant surface-wave excitation in the relativistic regime through measurements of proton acceleration from grating targets. *Phys. Rev. Lett.*, 111:185001, 2013.

[250] A. Sgattoni, L. Fedeli, G. Cantono, T. Ceccotti, and A. Macchi. High field plasmonics and laser-plasma acceleration in solid targets. *Plasma Phys. Control. Fusion*, 58(1):014004, 2016.

[251] L. Fedeli, A. Sgattoni, G. Cantono, D. Garzella, F. Réau, I. Prencipe, M. Passoni, M. Raynaud, M. Květoň, J. Proska, A. Macchi, and T. Ceccotti. Electron acceleration by relativistic surface plasmons in laser-grating interaction. *Phys. Rev. Lett.*, 116:015001, 2016.

[252] J. Kupersztych, M. Raynaud, and C. Riconda. Electron acceleration by surface plasma waves in the interaction between femtosecond laser pulses and sharp-edged overdense plasmas. *Phys. Plasmas*, 11(4):1669–1673, 2004.

[253] C. Riconda, M. Raynaud, T. Vialis, and M. Grech. Simple scalings for various regimes of electron acceleration in surface plasma waves. *Phys. Plasmas*, 22(7):073103, 2015.

[254] A. Bigongiari, M. Raynaud, and C. Riconda. Steady magnetic-field generation via surface-plasma-wave excitation. *Phys. Rev. E*, 84:015402, 2011.

[255] S. Busold, D. Schumacher, C. Brabetz, D. Jahn, F. Kroll, O. Deppert, U. Schramm, T.E. Cowan, A. Blažević, V. Bagnoud, and M. Roth. Towards highest peak intensities for ultra-short mev-range ion bunches. *Sci. Rep.*, 5:12459, 2015.

[256] J. Peebles, M.S. Wei, A.V. Arefiev, C. McGuffey, R.B. Stephens, W. Theobald, D. Haberberger, L.C. Jarrott, A. Link, H. Chen, H.S. McLean, A. Sorokovikova, S. Krasheninnikov, and F.N. Beg. Investigation of laser pulse length and pre-plasma scale length impact on hot electron generation on omega-ep. *New J. Phys.*, 19(2):023008, 2017.

[257] T.Zh. Esirkepov, J.K. Koga, A. Sunahara, T. Morita, M. Nishikino, K. Kageyama, H. Nagatomo, K. Nishihara, A. Sagisaka, H. Kotaki, T. Nakamura, Y. Fukuda, H. Okada, A.S. Pirozhkov, A. Yogo, M. Nishiuchi, H. Kiriyama, K. Kondo, M. Kando, and S.V. Bulanov. Prepulse and amplified spontaneous emission effects on the interaction of a petawatt class laser with thin solid targets. *Nucl. Instr. Meth. Phys. Res. Sect. A*, 745:150–163, 2014.

[258] Paul McKenna, Filip Lindau, Olle Lundh, David Neely, Anders Persson, and Claes-Göran Wahlström. High-intensity laser-driven proton acceleration: influence of pulse contrast. *Phil. Trans. R. Soc. Lond. A*, 364(1840):711–723, 2006.

[259] C. Courtois, A. Compant La Fontaine, O. Landoas, G. Lidove, V. Méot, P. Morel, R. Nuter, E. Lefebvre, A. Boscheron, J. Grenier, M. M. Aléonard, M. Gerbaux, F. Gobet, F. Hannachi, G. Malka, J. N. Scheurer, and M. Tarisien. Effect of plasma density scale length on the properties of bremsstrahlung x-ray sources created by picosecond laser pulses. *Phys. Plasmas*, 16(1):013105, 2009.

[260] J. A. Cobble, R. P. Johnson, N. A. Kurnit, D. S. Montgomery, and J. C. Fernández. Cyclic plasma shearing interferometry for temporal characterization of a laser-produced plasma. *Rev. Sci. Instr.*, 73(11):3813–3817, 2002.

[261] N.E. Andreev, M.E. Povarnitsyn, L.P. Pugachev, and P.R. Levashov. Laser electron acceleration in the prepulse produced plasma corona. *J. Phys.: Conf. Series*, 653(1):012006, 2015.

[262] S. Kahaly, S. Monchocé, H. Vincenti, T. Dzelzainis, B. Dromey, M. Zepf, Ph. Martin, and F. Quéré. Direct observation of density-gradient effects in harmonic generation from plasma mirrors. *Phys. Rev. Lett.*, 110:175001, 2013.

[263] F. Wagner, S. Bedacht, A. Ortner, M. Roth, A. Tauschwitz, B. Zielbauer, and V. Bagnoud. Pre-plasma formation in experiments using petawatt lasers. *Opt. Express*, 22(24):29505–29514, 2014.

[264] V. Stankevič, G. Račiukaitis, F. Bragheri, X. Wang, E. G. Gamaly, R. Osellame, and S. Juodkazis. Laser printed nano-gratings: orientation and period peculiarities. *Sci. Rep.*, 7:39989, 2017.

[265] K. Miyazaki and G. Miyaji. Nanograting formation through surface plasmon fields induced by femtosecond laser pulses. *J. Appl. Phys.*, 114(15):153108, 2013.

[266] W. Wan, W. Qiao, W. Huang, M. Zhu, Z. Fang, D. Pu, Y. Ye, Y. Liu, and L. Chen. Efficient fabrication method of nano-grating for 3d holographic display with full parallax views. *Opt. Express*, 24(6):6203–6212, 2016.

[267] L. Yuan and P. R. Herman. Layered nano-gratings by electron beam writing to form 3-level diffractive optical elements for 3d phase-offset holographic lithography. *Nanoscale*, 7:19905–19913, 2015.

[268] H. Cao, Z. Yu, J. Wang, J. O. Tegenfeldt, R. H. Austin, E. Chen, W. Wu, and S. Y. Chou. Fabrication of 10 nm enclosed nanofluidic channels. *Appl. Phys. Lett.*, 81(1):174–176, 2002.

[269] S. K. Lynch, C. Liu, N. Y. Morgan, X. Xiao, A. A. Gomella, D. Mazilu, E. E. Bennett, L. Assoufid, F. de Carlo, and H. Wen. Fabrication of 200 nm period centimeter area hard x-ray absorption gratings by multilayer deposition. *J. Micromech. Microeng.*, 22(10):105007, 2012.

[270] M.-S. Jo, K.-W. Choi, M.-H. Seo, and J.-B. Yoon. Realization of large-scale sub-10 nm nanogratings using a repetitive wet-chemical oxidation and etching technique. *Micro Nano Syst. Lett.*, 5(1):19, 2017.

[271] M. Blanco, C. Hernández-García, A. Chacón, M. Lewenstein, M. T. Flores-Arias, and L. Plaja. Phase matching effects in high harmonic generation at the nanometer scale. *Opt. Express*, 25(13):14974–14985, 2017.

[272] M. Lewenstein, Ph. Balcou, M. Yu. Ivanov, Anne L'Huillier, and P. B. Corkum. Theory of high-harmonic generation by low-frequency laser fields. *Phys. Rev. A*, 49:2117–2132, 1994.

[273] W. Becker, A. Lohr, M. Kleber, and M. Lewenstein. A unified theory of high-harmonic generation: Application to polarization properties of the harmonics. *Phys. Rev. A*, 56:645–656, 1997.

[274] P. B. Corkum. Plasma perspective on strong field multiphoton ionization. *Phys. Rev. Lett.*, 71:1994–1997, 1993.

[275] K. J. Schafer, Baorui Yang, L. F. DiMauro, and K. C. Kulander. Above threshold ionization beyond the high harmonic cutoff. *Phys. Rev. Lett.*, 70:1599–1602, 1993.

[276] M. B. Gaarde, J. L. Tate, and K. J. Schafer. Macroscopic aspects of attosecond pulse generation. *Journal of Physics B: Atomic, Molecular and Optical Physics*, 41(13):132001, 2008.

[277] P. Salières, A. L'Huillier, and M. Lewenstein. Coherence control of high-order harmonics. *Phys. Rev. Lett.*, 74:3776–3779, 1995.

[278] Philippe Balcou, Pascal Sali'eres, Anne L'Huillier, and Maciej Lewenstein. Generalized phase-matching conditions for high harmonics: The role of field-gradient forces. *Phys. Rev. A*, 55:3204–3210, 1997.

[279] T. Popmintchev, M.-C. Chen, D. Popmintchev, P. Arpin, S. Brown, S. Ališauskas, G. Andriukaitis, T. Balčiunas, O. D. Mücke, A. Pugzlys, A. Baltuška, B. Shim, S. E. Schrauth, A. Gaeta, C. Hernández-García, L. Plaja, A. Becker, A. Jaron-Becker, M. M. Murnane, and H. C. Kapteyn. Bright coherent ultrahigh harmonics in the kev x-ray regime from mid-infrared femtosecond lasers. *Science*, 336(6086):1287–1291, 2012.

[280] M.-C. Chen, C. Mancuso, C. Hernández-García, F. Dollar, B. Galloway, D. Popmintchev, P.-C. Huang, B. Walker, L. Plaja, A. A. Jaron-Becker, A. Becker, M. M. Murnane, H. C. Kapteyn, and T. Popmintchev. Generation of bright isolated attosecond soft x-ray pulses driven by multicycle midinfrared lasers. *Proc. Nat. Ac. Sci.*, 111(23):E2361–E2367, 2014.

[281] C. Hernández-García, T. Popmintchev, M. M. Murnane, H. C. Kapteyn, L. Plaja, A. Becker, and A. Jaron-Becker. Isolated broadband attosecond pulse generation with near- and mid-infrared driver pulses via time-gated phase matching. *Opt. Express*, 25(10):11855–11866, 2017.

[282] E. Skantzakis, S. Chatziathanasiou, P. A. Carpeggiani, G. Sansone, A. Nayak, D. Gray, P. Tzallas, D. Charalambidis, E. Hertz, and O. Faucher. Polarization shaping of high-order harmonics in laser-aligned molecules. *Sci. Rep.*, 6:39295, 2016.

[283] C. Hernández-García, C. G. Durfee, D. D. Hickstein, T. Popmintchev, A. Meier, M. M. Murnane, H. C. Kapteyn, I. J. Sola, A. Jaron-Becker, and A. Becker. Schemes for generation of isolated attosecond pulses of pure circular polarization. *Phys. Rev. A*, 93:043855, 2016.

[284] C. Hernández-García, A. Picón, J. San Román, and L. Plaja. Attosecond extreme ultraviolet vortices from high-order harmonic generation. *Phys. Rev. Lett.*, 111:083602, 2013.

[285] C. Hernández-García, J. San Román, L. Plaja, and A. Picón. Quantum-path signatures in attosecond helical beams driven by optical vortices. *New J. Phys.*, 17(9):093029, 2015.

[286] J. M. Pitarke, V. M. Silkin, E. V. Chulkov, and P. M. Echenique. Theory of surface plasmons and surface-plasmon polaritons. *Rep. Prog. Phys.*, 70(1):1, 2007.

[287] J. Zhang, L. Zhang, and W. Xu. Surface plasmon polaritons: physics and applications. *J. Phys. D: Appl. Phys.*, 45(11):113001, 2012.

[288] X. Luo and L. Yan. Surface plasmon polaritons and its applications. *IEEE Photonics Journal*, 4(2):590–595, 2012.

[289] S. Kim, J. Jin, Y.-J. Kim, I.-Y. Park, Y. Kim, and S.-W. Kim. High-harmonic generation by resonant plasmon field enhancement. *Nature*, 453(7196):757–760, 2008.

[290] M. Sivis, M. Duwe, B. Abel, and C. Ropers. Nanostructure-enhanced atomic line emission. *Nature*, 485(7397):E1–E3, 2012.

[291] N. Pfullmann, C. Waltermann, M. Noack, S. Rausch, T. Nagy, C. Reinhardt, M. Kovačev, V. Knittel, R. Bratschitsch, D. Akemeier, A. Hütten, A. Leitenstorfer, and U. Morgner. Bow-tie nano-antenna assisted generation of extreme ultraviolet radiation. *New J. Phys.*, 15(9):093027, 2013.

[292] S. Han, H. Kim, Y. W. Kim, Y.-J. Kim, S. Kim, I.-Y. Park, and S.-W. Kim. High-harmonic generation by field enhanced femtosecond pulses in metal-sapphire nanostructure. *Nat. Commun.*, 7:13105, 2016.

[293] G. Vampa, B. G. Ghamsari, S. Siadat Mousavi, T. J. Hammond, A. Olivieri, E. Lisicka-Skrek, A. Yu. Naumov, D. M. Villeneuve, A. Staudte, P. Berini, and P. B. Corkum. Plasmon-enhanced high-harmonic generation from silicon. *Nat. Phys.*, 13:659–662, 2017.

[294] A. Husakou, S.-J. Im, and J. Herrmann. Theory of plasmon-enhanced high-order harmonic generation in the vicinity of metal nanostructures in noble gases. *Phys. Rev. A*, 83:043839, 2011.

[295] S. L. Stebbings, F. Süßmann, Y.-Y. Yang, A. Scrinzi, M. Durach, A. Rusina, M. I. Stockman, and M. F. Kling. Generation of isolated attosecond extreme ultraviolet pulses employing nanoplasmonic field enhancement: optimization of coupled ellipsoids. *New J. Phys.*, 13(7):073010, 2011.

[296] J. Choi, S. Kim, I.-Y. Park, D.-H. Lee, S. Han, and S.-W. Kim. Generation of isolated attosecond pulses using a plasmonic funnel-waveguide. *New J. Phys.*, 14(10):103038, 2012.

[297] M. Sivis, M. Duwe, B. Abel, and C. Ropers. Extreme-ultraviolet light generation in plasmonic nanostructures. *Nat. Phys.*, 9(5):304–309, 2013.

[298] S. Kim, J. Jin, Y.-J. Kim, I.-Y. Park, Y. Kim, and S.-W. Kim. Kim et al. reply. *Nature*, 485(7397):E1–E3, 2012.

[299] M. F. Ciappina, J. Biegert, R. Quidant, and M. Lewenstein. High-order-harmonic generation from inhomogeneous fields. *Phys. Rev. A*, 85:033828, 2012.

[300] C. Hernández-García, J. A. Pérez-Hernández, J. Ramos, E. C. Jarque, L. Roso, and L. Plaja. High-order harmonic propagation

in gases within the discrete dipole approximation. *Phys. Rev. A*, 82:033432, 2010.

[301] C. Hernández-García, T. Popmintchev, M. M. Murnane, H. C. Kapteyn, L. Plaja, A. Becker, and A. Jaron-Becker. Group velocity matching in high-order harmonic generation driven by mid-infrared lasers. *New J. Phys.*, 18(7):073031, 2016.

[302] L. V. Keldysh. Ionization in the field of a strong electromagnetic wave. *Zh. Eksp. Teor. Fiz.*, 47:1945, 1965.

[303] F. H. M. Faisal. Multiple absorption of laser photons by atoms. *J. Phys. B-At. Mol. Opt.*, 6(4):L89, 1973.

[304] H. R. Reiss. Effect of an intense electromagnetic field on a weakly bound system. *Phys. Rev. A*, 22:1786–1813, 1980.

[305] J. A. Pérez-Hernández, L. Roso, and L. Plaja. Harmonic generation beyond the strong-field approximation: the physics behind the short-wave-infrared scaling laws. *Opt. Express*, 17(12):9891–9903, 2009.

[306] J. A. Pérez-Hernández, C. Hernández-García, J. Ramos, E. C. Jarque, L. Plaja, and L. Roso. *New Methods For Computing High-Order Harmonic Generation and Propagation*, pages 145–162. Springer, 2011.

[307] C. Hernández-García, I. J. Sola, and L. Plaja. Signature of the transversal coherence length in high-order harmonic generation. *Phys. Rev. A*, 88:043848, 2013.

[308] C. Hernández-García, W. Holgado, L. Plaja, B. Alonso, F. Silva, M. Miranda, H. Crespo, and I. J. Sola. Carrier-envelope-phase insensitivity in high-order harmonic generation driven by few-cycle laser pulses. *Opt. Express*, 23(16):21497–21508, 2015.

[309] P. Antoine, B. Piraux, and A. Maquet. Time profile of harmonics generated by a single atom in a strong electromagnetic field. *Phys. Rev. A*, 51:R1750–R1753, 1995.

[310] G. Sansone, E. Benedetti, F. Calegari, C. Vozzi, L. Avaldi, R. Flammini, L. Poletto, P. Villoresi, C. Altucci, R. Velotta, S. Stagira, S. De Silvestri, and M. Nisoli. Isolated single-cycle attosecond pulses. *Science*, 314(5798):443–446, 2006.

[311] E. N. Osika, A. Chacón, L. Ortmann, N. Suárez, J. A. Pérez-Hernández, B. Szafran, M. F. Ciappina, F. Sols, A. S. Landsman, and M. Lewenstein. Wannier-bloch approach to localization in high-harmonics generation in solids. *Phys. Rev. X*, 7:021017, 2017.

USC
UNIVERSIDADE
DE SANTIAGO
DE COMPOSTELA

PUBLICATIONS

2015

- M. Blanco, D. Nieto and M.T. Flores-Arias, *Fabrication of a microlens array in BK7 through laser ablation and thermal treatment techniques*, J. Phys.: Conf. Ser. **605**, 012023 (2015)

2017

- M. Blanco, M.T. Flores-Arias, C. Ruiz and M. Vranic, *Table-top laser-based proton acceleration in nanostructured targets*, New J. Phys. **19**, 033004 (2017)
- F. Cambronero-López, M. Blanco, C. Ruiz, M.T. Flores-Arias and C. Bao-Varela, *Polarization gating using cross-polarized wave generation with multicycle lasers to produce isolated attosecond pulses in overdense media*, J. Opt. Soc. Am. B **34**(4), 843–849 (2017)
- M. Blanco and M.T. Flores-Arias, *Frequency gating to isolate single attosecond pulses with overdense plasmas using particle-in-cell simulations*, Opt. Express **25**(12), 13372–13381 (2017)
- M. Blanco, C. Hernández-García, A. Chacón, M. Lewenstein, M.T. Flores-Arias and L. Plaja, *Phase matching effects in high harmonic generation at the nanometer scale*, Opt. Express **25**(13), 14974–14985 (2017)

2018

- M. Blanco, M.T. Flores-Arias and A. Gonoskov, *Controlling the ellipticity of attosecond pulses generated in the non-mirror regime of laser-plasma interaction*, arXiv:1706.04785 (under peer review)
- M. Blanco, M.T. Flores-Arias and M. Vranic, *Suitability and robustness of triangular nanostructured targets for proton acceleration* (under preparation)

USC
UNIVERSIDADE
DE SANTIAGO
DE COMPOSTELA

CONTRIBUTIONS TO CONFERENCES

2014

- M. Blanco, D. Nieto and M. T. Flores-Arias, *Fabrication of microlens arrays on borosilicate glass using a combination of a stepped laser direct-write and a thermal reflow technique* (Poster) **II International Conference on Applications of Optics and Photonics - AOP2014**, 26-30 May 2014, Aveiro (Portugal)

- M. Blanco, D. Nieto and M. T. Flores-Arias, *Fabrication of a microlens array in BK7 through laser ablation and thermal treatment techniques* (Poster) **International Commission for Optics 23 - ICO23**, 26-29 August 2014, Santiago de Compostela (Spain) (Prize to best student poster contribution)

2015

- M. Blanco, *Creación dun código PIC para a simulación de interacións láser-plasma* (Poster) **III Encontro Mocidade Investigadora**, 25-26 March 2015, Santiago de Compostela (Spain)

- M. Blanco, C.Ruiz and M.T. Flores-Arias, *Analytical model for low intensity high harmonic generation* (Poster) **Ultrafast Science and Technology Spain 2015 - USTS2015**, 24-26 November 2015, Madrid (Spain)

- M. Blanco, C.Ruiz and M.T. Flores-Arias, *Polarization gating to generate high energy ultrashort pulses in overdense plasmas, theory and simulation* (Oral) **XI Reunión Nacional de Óptica - RNOXI**, 1-4 September 2015, Salamanca (Spain)

- M. Blanco, C. Ruiz and M.T. Flores-Arias, *Polarization gating to generate high energy ultrashort pulses in overdense plasmas, theory and simulation* (Oral) **I Workshop do Programa de Doutoramento interuniversitario en Láser, Fotónica e Visión**, 25 September 2015, Santiago de Compostela (Spain)

2016

- M. Blanco, C.Ruiz, M.T. Flores-Arias and M. Vranic, *Ion acceleration in microstructured targets* (Poster) **43rd EPS Conference on Plasma Physics - EPS2016**, 3-9 July 2016, Leuven (Belgium)

- M. Blanco, F. Cambronero-López, C. Bao-Varela, M.T. Flores-Arias and C. Ruiz, *High harmonic generation of elliptically polarized pulses* (Poster) **7th International Comitee on Ultrahigh Intensity Lasers - ICUIL2016**, 11-16 September 2016, Montebello (Canada)

- F. Cambronero-López, M. Blanco, M.T. Flores-Arias, C. Bao-Varela and C. Ruiz, *Generation of interference patterns in BaF_2 crystal* (Poster) **7th International Comitee on Ultrahigh Intensity Lasers - ICUIL2016**, 11-16 September 2016, Montebello (Canada)

- F. Cambronero-López, M. Blanco, C.Bao-Varela, J. Arines, R. Romero, F. Silva, H. Crespo and M.T.Flores-Arias, *D-scan real-time detection of fast spectral phase distortions imparted by dielectric mirrors in femtosecond laser pulses* (Poster) **7th International Comitee on Ultrahigh Intensity Lasers - ICUIL2016**, 11-16 September 2016, Montebello (Canada)

- P. Aguiar, J. Arines, C. Bao-Varela, M. Blanco, F. Cambronero-López, A. Iglesias, J. Silva-Rodriguez and M.T. Flores-Arias, *Radioisotope production by laser for PET imaging* (Oral) **8th Petawatt Conference**, 10-11 September 2016, Montebello (Canada)

- M. Blanco, F. Cambronero-López, M.T. Flores-Arias and C. Ruiz, *Isolation of attosecond pulses by polarization gating using Cross Polarized Wave generation* (Oral) **II Workshop do Programa de Doutoramento interuniversitario en Láser, Fotónica e Visión**, 7 October 2016, Santiago de Compostela (Spain)

2017

- M. Aymerich, F. Cambronero-López, Á.L. Aragón, T. Delgado, M. Blanco, A.I. Gómez-Varela, A. Gargallo, S. Williamson, A. Amorín, Á- Sánchez-García, C-.Bao-Varela and M.T. Flores-Arias, *The USC-EPS Young Minds Section Activities in Optics* (Poster) **6th YM Leadership Meeting**, 12-13 May 2017, Naples (Italy)

- M.T. Flores-Arias, A. Iglesias, M. Blanco, C. Bao-Varela, P. Aguiar, J. Silva-Rodríguez, J. Arines and F. Cambronero-López, *PET imaging by high power table-top lasers* (Oral) **III International Conference on Applications of Optics and Photonics - AOP2017**, 8-12 May 2017, Faro (Portugal)

- M. Blanco, C. Hernández- García, A. Chacón, M. Lewenstein, M. Flores- Arias, and L. Plaja, *High Harmonic Generation by Resonant Nano-Antennas: Phase Matching at the Nanometer Scale* (Oral) **Conference on Lasers and Electro-Optics - CLEO Europe 2017**, 25-29 June 2017, Munich (Germany)

- M. Blanco, M.T. Flores-Arias and A. Gonoskov, *Circularly polarized HHG with matched laser-plasma conditions* (Poster) **44th Conference on Plasma Physics - EPS2017**, 26-30 June 2017, Belfast (United Kingdom)

- M. Blanco and M.T. Flores-Arias, *Single attosecond pulse isolation in overdense plasmas via frequency gating* (Poster) **Ultrafast Science and Technology Spain 2017 - USTS2017**, 22-24 November 2017, Salamanca (Spain)

- M. Blanco, C. Hernández-García, A. Chacón, M. Lewenstein, M.T. Flores-Arias, and L. Plaja, *Phase matching effects in high harmonic generation in nanoantennas* (Oral) **Ultrafast Science and Technology Spain 2017 - USTS2017**, 22-24 November 2017, Salamanca (Spain) (Prize for best student oral contribution)

- M.T. Flores-Arias, C. Bao-Varela, M. Blanco, A. Iglesias, J. Silva-Rodríguez, F. Cambronero-López, J. Arines and P. Aguiar, *Biomed-*

ical applications of high power table top lasers (Oral) **Ultrafast Science and Technology Spain 2017 - USTS2017**, 22-24 November 2017, Salamanca (Spain)

- M. Blanco, M.T. Flores-Arias and A. Gonoskov, *Controlling the polarization of attosecond pulses generated with matched laser-plasma conditions* (Oral) **III Workshop Programa Interuniversitario de Doutoramento en Láser, Fotónica e Visión**, Santiago de Compostela (Spain)

- A. Gonoskov, T. Blackburn, M. Blanco, M.T. Flores-Arias, B. Wettervik and M. Marklund, *Prospects of X-Ray Generation in the Non-Mirror Regime of Laser Plasma Interaction* (Oral) **26th ANNUAL INTERNATIONAL LASER PHYSICS WORKSHOP - LPHYS2017**, 17-21 July 2017, Kazan (Russia)

- A. Gonoskov, T. Blackburn, M. Blanco, M.T. Flores-Arias, B. Wettervik and M. Marklund, *X-Ray generation by the laser-plasma interaction in the regime of relativistic electronic spring* (Oral) **59th Annual Meeting of the APS Division of Plasma Physics**, 23-27 October 2017, Milwaukee (United States of America)

- M. Blanco, C. Hernández-García, A. Chacón, M. Lewenstein, M.T. Flores-Arias, and L. Plaja, *High harmonic generation in nanostructures: Phase matching effects* (Poster) **10 Reunión Nacional de Optoelectrónica - OPTOEL2017**, 12-14 July 2017, Santiago de Compostela (Spain)